ABSTRACT

Title of dissertation: SEMICONDUCTOR WAVEGUIDES FOR NONLINEAR OPTICAL SIGNAL PROCESSING

Paveen Apiratikul, Doctor of Philosophy, 2009

Dissertation directed by: Professor Thomas E. Murphy
Department of Electrical and Computer Engineering

This thesis investigates nonlinear effects in semiconductor waveguides for optical signal processing. Two semiconductor waveguides are studied : nanoporous silicon waveguide and GaAs/AlGaAs waveguide. First, nonlinear optical properties of nanoporous silicon waveguides including two-photon absorption, self-phase modulation and free-carrier effects are characterized and compared with similar measurements conducted on conventional silicon-on-insulator waveguides. Then, we experimentally demonstrate 10-Gb/s wavelength conversion using cross-amplitude modulation, cross-phase modulation and four-wave-mixing in GaAs/AlGaAs waveguides. Finally, we propose an ultrafast optical sampling system based on non-degenerate two-photon absorption in a GaAs photodiode. Using this technique, we successfully demonstrate a background-suppressed measurement of quasi 4-Tb/s eye diagrams.

SEMICONDUCTOR WAVEGUIDES FOR NONLINEAR OPTICAL SIGNAL PROCESSING

by

Paveen Apiratikul

Dissertation submitted to the Faculty of the Graduate School of the
University of Maryland, College Park in partial fulfillment
of the requirements for the degree of
Doctor of Philosophy
2009

Advisory Committee:
Professor Thomas E. Murphy, Chair/Advisor
Professor Julius Goldhar
Professor Mario Dagenais
Professor Gary M. Carter
Professor John T. Fourkas

Dedication

To my grandparents, my Dad and Mom.

Acknowledgments

I would like to thank all people who have helped and inspired me throughout my Ph.D. study.

First and foremost, I would like to thank my advisor, Prof. Thomas Murphy for his invaluable support, advice, and encouragement. He has always made himself available for help and advice. I have learned a lot from him, especially the way he has approached the problem and the way he resolved it, which is very effective. He also has taught me how to present my work effectively. He has always been supportive and encouraged me when things did not go quite right and motivated me to do my very best. It has been my pleasure to work with and learn from him.

I also would like to thank Prof. Julius Goldhar, Prof. Mario Dagenais, Prof. Gary Carter and Prof. John Fourkas for agreeing to serve on my thesis committee and for their valuable comments and suggestions.

Several projects included in my thesis have been done in Laboratory for Physical Sciences (LPS). The wavelength conversion project has been done in collaboration with Prof. Gary Carter's group from University of Maryland, Baltimore County (UMBC). I want to thank Prof. Carter for his support and useful discussions. I would also like to thank the researcher in his group, Dr. William Astar who has helped me throughout this work with advice, knowledge, and assistance. I have enjoyed working with him on this project.

I would like to thank the researchers and staff of cleanroom in LPS. Warren Berk, Dan Hinkel and Scott Horst have helped me a lot in developing process recipes and train-

ing me how to operate several equipments including an inductively coupled plasma etching system and a scanning electron microscope. Laurence Olver, Steve Brown and Lisa Lucas have helped me for the general cleanroom training. I am also grateful to Prof. Goldhar for allowing me to use the equipments in his lab and to Victor Yun for training me how to use these equipments. I also would like to thank Dr. Christopher Richardson and his student, Dyan Ali for valuable advices and assistance for waveguide characterization.

I would like to thank cleanroom staff of the Nanocenter at the University of Maryland, College Park. Tom Loughran is the first person who trained me how to work in cleanroom. I also would like to thank Jonathan Hummel for helping me when I had problems with the electron-beam lithography machine.

I am grateful to the members of our Photonics Research Laboratory. Shu Zee Alencious (Alen) Lo is an expert in operating an optical parametric oscillator in our lab. My projects could not have been accomplished without Alen's helpful advice and assistance. He also has helped me out in many ways in the lab and has been a very nice officemate. Resa Salem is also a very nice officemate. I have used several simulation softwares developed by him. I always had a very useful discussions with him during several parts of my research. I also would like to thank Dr. Andrea Rossi, a postdoctoral researcher in our lab. He was the person who fabricated porous silicon waveguides for me. I am also grateful to Dr. Zhifu Liu. He was another postdoctoral researcher in our lab. With his life experience and his technical knowledge, I have always benefited from discussions with him.

I would like to thank all of my friends in College Park to make me feel like home during my Ph.D. study. We have a very nice and helpful community here that I am glad

to be a part of. I would like to express my appreciation to Pannipa Kiatbaramee for her support and patience during some of the most difficult time of my Ph.D. work. Her encouraging messages have always provided me strength and comfort.

Finally, I would like to express my gratitude to my family and my parents, Pew and Suganya Apiratikul for providing me with the best educational opportunities. It is their sacrifices and efforts that allow me to realize my own potential.

Table of Contents

List of Tables

List of Figures

Chapter 1

Introduction

Due to the increasing demand for high-speed data transmission over optical fiber in the future, the data rate for a single channel could exceed the speed of electrical circuits currently used in optical networks. Optical signal processing will have to be developed to provide a solution for high-speed optical networks. Optical signal processing is often based on ultrafast nonlinear effects in waveguide devices. The nonlinear interaction efficiency could be enhanced by confining optical waves in an optical waveguide with a small cross-sectional area and maintaining high optical intensity along the waveguide. This means that strong nonlinear interaction can be achieved over the long propagation length, therefore nonlinear waveguide-based devices can have a high nonlinear interaction efficiency at lower input power compared to nonlinear bulk devices [1]. Nonlinear waveguide devices based on a variety of nonlinear materials have been proposed for optical signal processing including periodically poled lithium niobate (PPLN) waveguides [2], semiconductor optical amplifiers (SOAs) [3], highly nonlinear fibers (HNLFs) [4,5], nonlinear polymer in slot waveguides [6, 7], Chalcogenide glass waveguides [8, 9], silicon-on-insulator (SOI) waveguides [10, 11] and III-V semiconductor waveguides [12, 13].

In this thesis, we focus on nonlinear optical signal processing based on third-order nonlinear effects including two-photon absorption (2PA), cross-absorption modulation (XAM), cross-phase modulation (XPM) and four-wave mixing (FWM) in semiconductor

waveguides. Two semiconductor waveguides investigated in this thesis are porous silicon waveguides and GaAs/AlGaAs waveguides.

Porous silicon waveguides provide an interesting alternative to conventional silicon-on-insulator (SOI) structures that could offer advantages for silicon interconnects, modulators and components. Porous silicon is a nanoscale composite material with an effective refractive index between that of air and silicon that can easily be fabricated in multi-layer structures. However, the linear and nonlinear properties of porous silicon have not been extensively explored. Prior reports of nonlinearity in porous silicon have been performed at the wavelengths below 1064 nm, where it is difficult to discern the role of free-carriers and interband absorption [14–16]. All of these studies did not differentiate between instantaneous effects (such as optical Kerr effect and two-photon absorption) and free-carrier effects. To our knowledge, there has been no reported study of nonlinear optical properties of porous silicon in the important 1.55 μm spectral regime, and no observation of nonlinear effects in a porous waveguide. In chapter 2, we describe the design, fabrication and report the first measurement of optical nonlinearities including two-photon absorption (2PA), self-phase modulation (SPM), free-carrier absorption (FCA), free-carrier dispersion (FCD), and free-carrier lifetime in a porous silicon waveguide at telecommunication wavelengths.

GaAs/AlGaAs waveguides provide interesting optical properties for nonlinear optical signal processing. In addition to the band-gap engineering capability, GaAs/AlGaAs has excellent electro-optic properties. The Optical Kerr coefficient of GaAs is approximately 4 times larger than that of crystalline silicon [17], which can relax fabrication processes, and facilitate coupling to the fiber. Several groups have reported on the third-

order nonlinear effects in GaAs/AlGaAs devices such as waveguides [18], microring resonators [19], photonic crystal cavities [20] and nanowires [21]. The nonlinear efficiency in these devices is typically limited by propagation loss. Recently, GaAs/AlGaAs waveguides with an effective area of 0.4 μm^2 have been demonstrated with the propagation loss as low as 0.9 dB/cm at 1550 nm [22].

Although optical signal processing using third-order nonlinearities in GaAs/AlGaAs devices has been demonstrated, there have been no reports on data performance metrics such as eye-diagrams or bit-error rate (BER) receiver sensitivity for these devices.

In chapter 3, we detail the fabrication process of GaAs/AlGaAs ridge waveguides with and without electrical contacts. The properties of these waveguides are also characterized.

In chapter 4, we demonstrate 10-Gb/s all-optical wavelength conversion systems exploiting XAM, XPM and FWM effects in these GaAs/AlGaAs waveguides. We, for the first time, measure eye-diagrams and bit-error rate receiver sensitivity for wavelength conversion using a GaAs/AlGaAs waveguide.

In chapter 5, we describe an ultrafast optical sampling system that uses nondegenerate two-photon absorption in a GaAs photodiode. We introduce a technique to suppress large photocurrent associated with two-photon absorption of the strong sampling pulses. We demonstrate a background-suppressed measurement of quasi 4-Tb/s eye diagrams. We also show preliminary results of a waveguide-based device that use this technique.

Chapter 2

Nonlinearities in Porous Silicon Optical Waveguides

In this chapter, we describe the measurement of nonlinear effects in porous silicon waveguides. We start by explaining the theoretical analysis of nonlinear propagation in an optical waveguide. Then we describe the fabrication process of porous silicon waveguides. Next, we show the experimental results of linear properties and nonlinear effects in porous silicon waveguides. Finally, we compare the results from porous silicon waveguides and those obtained from conventional silicon-on-insulator (SOI) ridge waveguides.

Porous silicon offers an interesting, although less explored, alternative to conventional silicon structures that could offer advantages for silicon interconnects, modulators and components. Porous silicon is fabricated by electrochemical etching of crystalline silicon, which produces a nanoporous skeleton comprised of silicon and air. The typical pore size formed in this process ranges from 5–100 nm, depending on the etching chemistry and substrate doping. The scanning electron micrograph in Fig. 2.1 shows a top-down view of the porous silicon layer with 80% porosity, illustrating the nanoscale texture. Because the pores are smaller than the optical wavelength, porous silicon behaves like an effective medium with refractive index between that of air and silicon. The refractive index depends on the porosity, which can be controlled by adjusting the electrochemical current density [23]. Complex multilayer porous structures can be fabricated by varying the current density during fabrication. Several groups have demonstrated op-

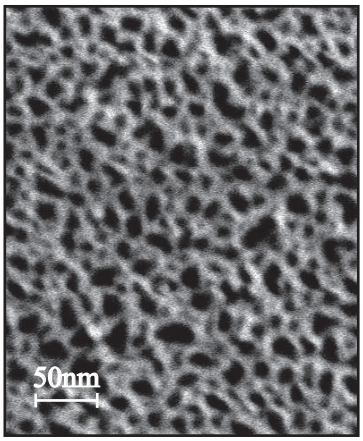

Figure 2.1: The scanning electron micrograph shows the top-down view of the porous silicon with 80% porosity.

toelectronic devices based on porous silicon including waveguides [24, 25], LEDs [26], photodetectors [27], passive optical filters [28], microcavities [29], sensors [30] and optical switches [31].

In addition to the flexibility of a controllable refractive index, porous silicon has a number of unique properties that make it attractive for modulators and sensors. It is electrically conductive in the direction perpendicular to the surface, while being optically transparent for signals polarized parallel to the surface, which could facilitate optoelectronic connectivity. As we will show in this chapter, the large internal surface area of porous silicon increases the surface recombination rate, which dramatically reduces the free-carrier lifetime.

Despite the potential applications, the nonlinear properties of porous silicon have not been extensively explored. Prior measurements of nonlinearities in porous silicon have all been performed at wavelengths below 1064 nm [14–16], where it is difficult to discern the role of free carriers and interband absorption. All of these studies did not dif-

ferentiate between instantaneous effects (such as optical Kerr effect and two-photon absorption) and free-carrier effects. In semiconductor waveguides, free carriers could lead to additional losses through free-carrier absorption (FCA) and refractive-index changes through free-carrier dispersion (FCD). Therefore, it is important to include both instantaneous nonlinear processes and free-carrier effects in numerical simulations of optical pulses propagating through semiconductor waveguides.

We report the first measurement of optical nonlinearities including two-photon absorption (2PA), self-phase modulation (SPM), free-carrier absorption, free-carrier dispersion, and free-carrier lifetime in a porous silicon waveguide at telecommunication wavelengths. We used a combination of three different measurements: pump-probe transient absorption, nonlinear changes in the transmitted power and nonlinear changes in the transmitted spectrum. By matching these measurements against numerical simulations, we estimated the coefficients that describe these nonlinear effects in porous silicon waveguides.

2.1 Nonlinear Pulse Propagation in Optical Waveguides

A complete description of nonlinear propagation in semiconductor waveguides must include both instantaneous nonlinear processes and free-carrier effects. The evolution of an optical signal in the waveguide can be modeled by the following propagation equa-

tion [32, 33]:

$$\frac{\partial}{\partial z}u(z,t) = -\frac{\alpha}{2}u(z,t) \tag{2.1a}$$

$$+\left[i\frac{\omega}{c}n_2 - \frac{\beta_{2PA}}{2}\right]\frac{|u(z,t)|^2}{A_{\text{eff}}}u(z,t) \tag{2.1b}$$

$$-\left[i\frac{\omega}{c}\Delta n_{\text{FCD}}(z,t) + \frac{1}{2}\Delta\alpha_{\text{FCA}}(z,t)\right]u(z,t)\ , \tag{2.1c}$$

where $u(z,t)$ is the slowly-varying field, normalized such that $|u(z,t)|^2$ represents the total optical power carried by the TE mode, α is the linear attenuation coefficient, n_2 is the optical Kerr coefficient, β_{2PA} is the two-photon absorption coefficient, and A_{eff} is the effective area of the TE mode.

Free-carrier plasma dispersion and free-carrier absorption are described by the quantities Δn_{FCD} and $\Delta\alpha_{\text{FCA}}$ appearing in Eq. (2.1c), both of which implicitly depend on the excess carrier density. For simplicity, we used a Drude model, in which Δn_{FCD} and $\Delta\alpha_{\text{FCA}}$ are assumed to be proportional to the excess carrier concentration ΔN:

$$\Delta\alpha_{\text{FCA}}(z,t) = \sigma_{\text{FCA}}\Delta N(z,t) \tag{2.2a}$$

$$\Delta n_{\text{FCD}}(z,t) = k_{\text{FCD}}\Delta N(z,t)\ , \tag{2.2b}$$

where σ_{FCA} is the free-carrier absorption cross section, k_{FCD} is the free-carrier dispersion coefficient, and $\Delta N(z,t)$ is the excess carrier density, averaged over the effective mode area. To simplify the calculations, we assume that σ_{FCA} and k_{FCD} are uniform over the effective mode area, we assume equal carrier concentrations and lifetimes for electrons and holes, and we neglect the sub-linear relationship between ΔN and Δn that has been empirically reported for holes in silicon [34, 35]. In general, there are several processes that can contribute to the carrier recombination, including surface recombination and bulk

carrier recombination. If we assume that free-carriers are generated exclusively by two-photon absorption, and that all carrier recombination processes can be described by a single time constant, then the excess carrier concentration evolves according to

$$\frac{\partial}{\partial t}\Delta N(z,t) = \frac{\beta_{2\mathrm{PA}}}{2\hbar\omega}\left[\frac{|u(z,t)|^2}{A_{\mathrm{eff}}}\right]^2 - \frac{\Delta N(z,t)}{\tau_c}\,, \tag{2.3}$$

where τ_c is the free-carrier lifetime.

Equations (2.1)-(2.3) describe two coupled nonlinear partial differential equations that must be simultaneously solved to determine $\Delta N(z,t)$ and $u(z,t)$. Although approximate analytical solutions can be formulated [36], in this work we numerically integrated the equations using the split-step Fourier method [37–39].

2.2 Porous Silicon Waveguide Fabrication

2.2.1 Fabrication of Porous Silicon Slab Waveguides

Figure 2.2 depicts the electrochemical etching cell for fabricating porous silicon slab waveguides. Porous silicon was formed on a p^{++} doped ($N \simeq 10^{20}$ cm^{-3}) silicon wafer. A solution of hydrofluoric acid, water and ethanol in the volume ratio (3:3:2) was used as an electrolyte. The surface layer formed in the process has a porosity that depends on the current density. During electrochemical etching process, silicon atoms were removed from the crystalline lattice by an electrolytic process that involved a transfer of charge in the form of holes from the substrate to the electrolyte [40]. The current was controlled by the computer and was adjusted during etching in order to produce a three-layer waveguide as shown in Fig. 2.3(a). When forming the cladding regions, the applied

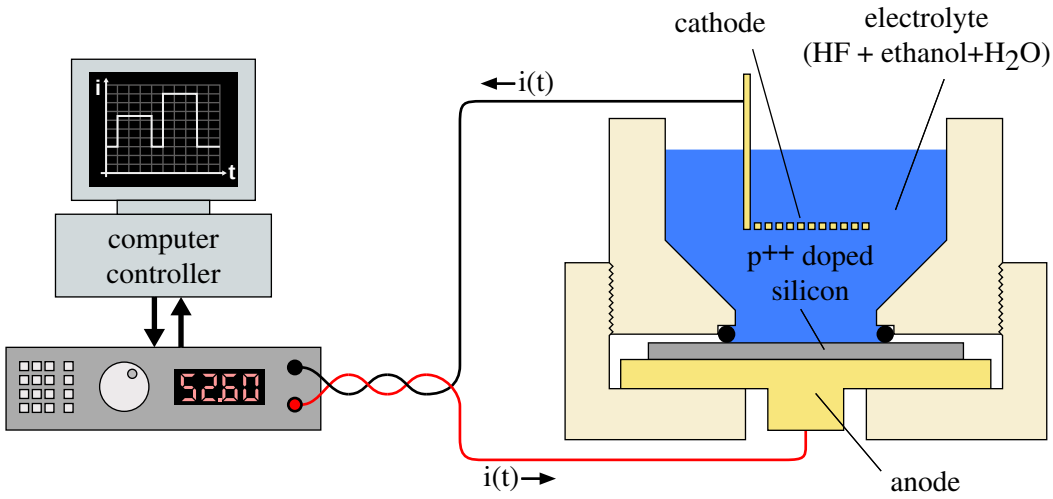

Figure 2.2: Electrochemical etching cell for fabricating porous silicon slab waveguides.

current density was 400 mA/cm^2, which was found to yield a 80% porous film with a refractive index of 1.6. The current density was temporarily reduced to 350 mA/cm^2 when etching the middle core layer, which produced a 70% porous layer with a refractive index of approximately 1.7. The refractive indices of the core and cladding layers were measured using normal-incidence spectral interferometry, performed on separately fabricated monolayer samples. This etching sequence produced a three-layer, slab waveguide composed of a 1.8 μm thick core layer sandwiched between two lower-index cladding regions with thicknesses of 1.5 and 4.3 μm, on top of a p^{++} silicon substrate. The micrograph in Fig. 2.3(b) shows a cross-section view of the three-layer porous silicon slab waveguide. The layer thicknesses were selected based on the refractive indices to ensure single-mode operation for the slab waveguide.

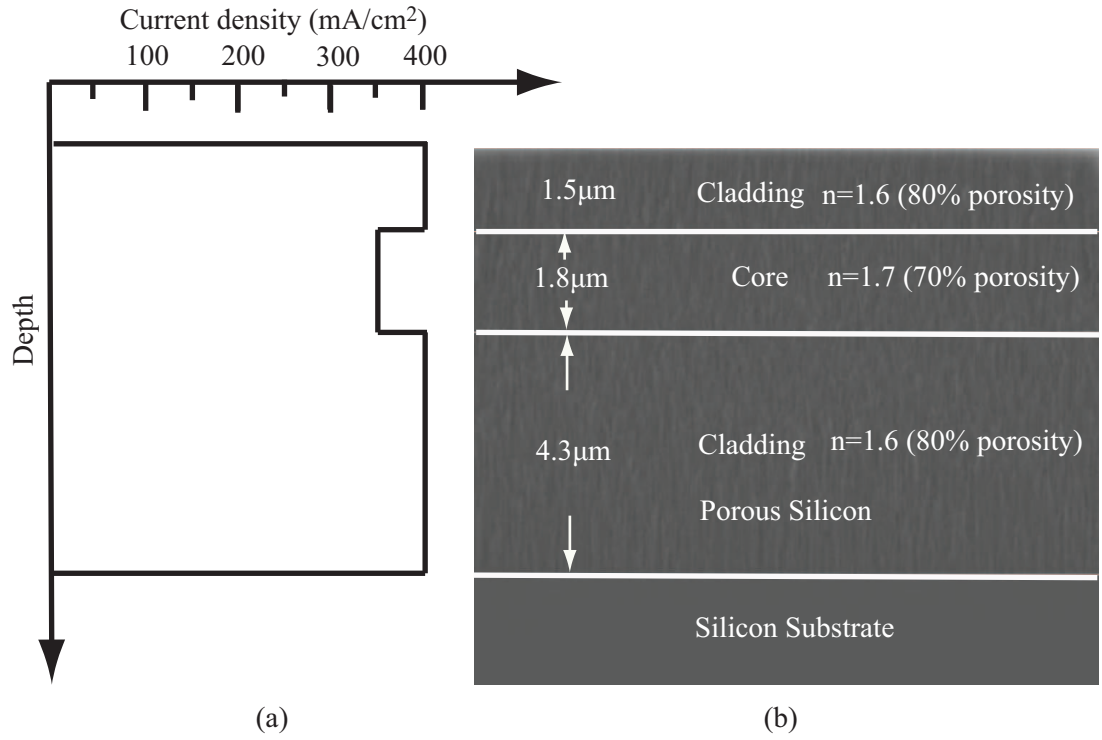

Figure 2.3: (a) The etching current sequence for producing three-layer porous silicon slab waveguide. (b) The cross-section view of the porous silicon slab waveguide.

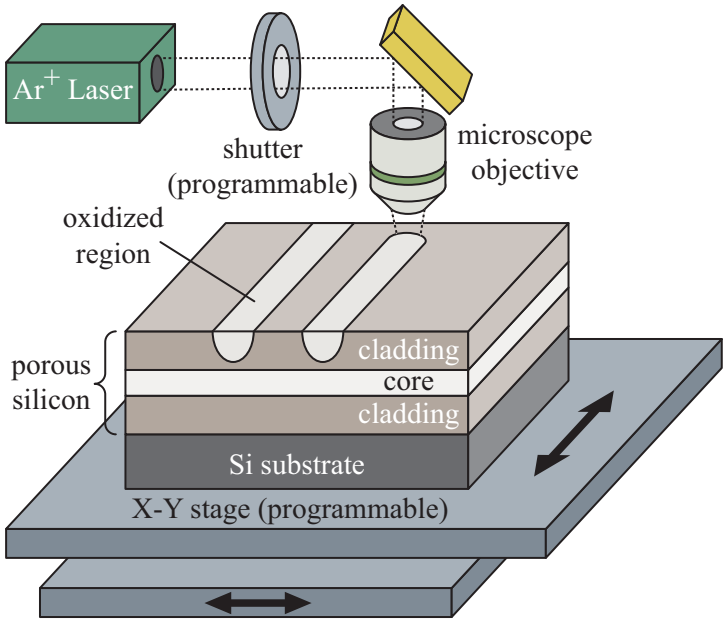

Figure 2.4: Scanning laser lithography system used to produce porous silicon waveguides through a process of laser-induced oxidation.

2.2.2 Fabrication of Porous Silicon Channel Waveguides

Many standard lithographic processes are incompatible with nanoporous silicon since most photoresist developers are alkaline solutions, which can quickly dissolve the porous matrix. Several alternative techniques have been proposed for the fabrication of porous silicon waveguides, including locally anodization using a nitride mask [24] or a silicon carbide mask [41], reactive ion etching using a nitride mask [25] and ion implantation to locally form a low-resistivity region [42]. In this work, we fabricated porous silicon channel waveguides using a laser-induced oxidation process described in [43]. This method allows the flexibility and control over the layer thicknesses and the waveguide dimensions and avoids the use of reactive ion etching (RIE), which can also pose problems because of the fragile, columnar nature of the porous silicon template.

After preparing the three-layer slab waveguide, a channel waveguide was patterned using the scanning laser lithography system depicted in Fig. 2.4. In this system, a 300 mW argon-krypton laser with wavelength of 647 nm was focused through a microscope objective onto the porous silicon sample, which caused localized heating and partial oxidation of the underlying porous silicon. The sample was then scanned beneath the focused beam to define two parallel lines, forming the left and right edges of the waveguide. The oxidized regions were then removed in a dilute hydrofluoric acid (HF) solution, forming two parallel trenches. As a final step, the entire sample was placed in an oven at 450 °C for 15 minutes to produce a thin, uniform, oxide layer in order to stabilize the freshly-etched porous silicon surface.

The degree of laser-induced oxidation depends on the temperature distribution under optical illumination. While the porous silicon directly beneath the microscope objective is completely oxidized, the adjacent regions are only partially oxidized. Therefore, in addition to the two parallel trenches, the HF dip is also thought to produce a graded index region that confines the optical mode in a region much narrower than the inscribed lines might otherwise suggest. We fabricated waveguides with several different line spacings, and in each case observed the transmitted mode pattern on a camera for evidence of higher-order spatial modes. Waveguides wider than 20 μm were observed to support higher-order modes, and waveguides narrower than 20 μm suffered higher loss. Figure 2.5 shows the scanning electron micrograph of the 20-μm wide porous silicon channel waveguide defined by laser-induced oxidation.

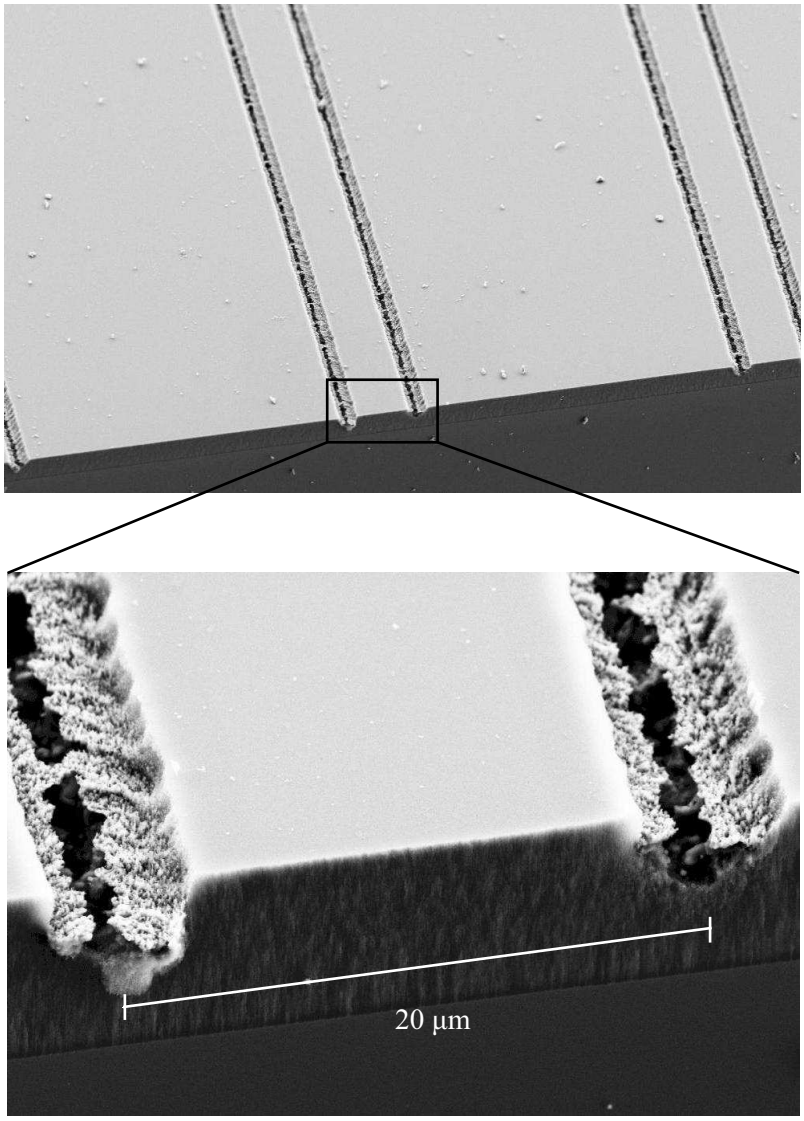

Figure 2.5: Scanning electron micrographs illustrating the porous silicon waveguides produced through a process of laser-induced oxidation.

2.3 Linear Measurements

2.3.1 Propagation Loss Measurement

We estimated propagation loss in a porous silicon waveguide by measuring scattered power along the waveguide. The experimental setup for this measurement is shown in Fig. 2.6. The continuous wave (CW) input signal at the wavelength of 1550 nm was coupled to a porous silicon waveguide. The scattered light from the surface of the waveguide was collected by an objective lens. The propagation loss α was measured by scanning the objective lens along the waveguide. By assuming that the scattered power is proportional to guided power at each point along the waveguide, the scattered power can be described by

$$P(z_2) = P(z_1)\exp[-\alpha(z_2 - z_1)]\,, \tag{2.4}$$

where $P(z_1)$ and $P(z_2)$ are the scattered power collected at distance z_1 and z_2 from the front facet, respectively. We measured 9-13 dB/cm for waveguides with 20-μm line spacing operating in TE mode. The measured propagation loss is consistent with the value inferred from the measurement of the insertion loss.

TM loss was observed to be very high in the porous silicon waveguide. The pores are preferentially oriented in the direction perpendicular to the surface of porous silicon, which causes significant form birefringence and polarization-dependent absorption in the waveguide. The porous waveguide is optically transparent for TE modes that are polarized orthogonal to the pores, but highly absorbing for signals that are polarized parallel to the

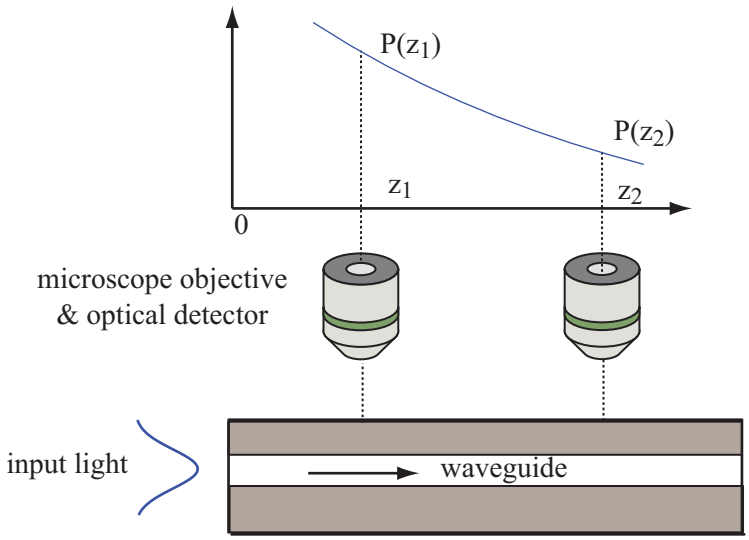

Figure 2.6: The experimental setup for measuring propagation loss in a porous silicon waveguide using scattering light measurement.

pores (TM modes). In this way, the heavily doped porous silicon behaves much like a wire-grid polarizer, which inhibits conductivity along the direction parallel to the wires.

2.3.2 Group Index Measurement

The Fabry-Pérot technique can be used for measuring the propagation loss and group index of the waveguides [44]. The technique relies on cleaved waveguide facets to form a Fabry-Pérot cavity. The propagation loss measurement requires an accurate value of the endfacet reflectivity, which is difficult to measure in porous silicon waveguide. Because of the fragile, columnar nature of the porous silicon, the cleaved facets are often not perfectly perpendicular to the waveguide edge. The endfacet reflectivity is very low because of the small difference between refractive index of porous silicon and that of air. Nonetheless, we measured group index of the waveguide using the Fabry-Pérot tech-

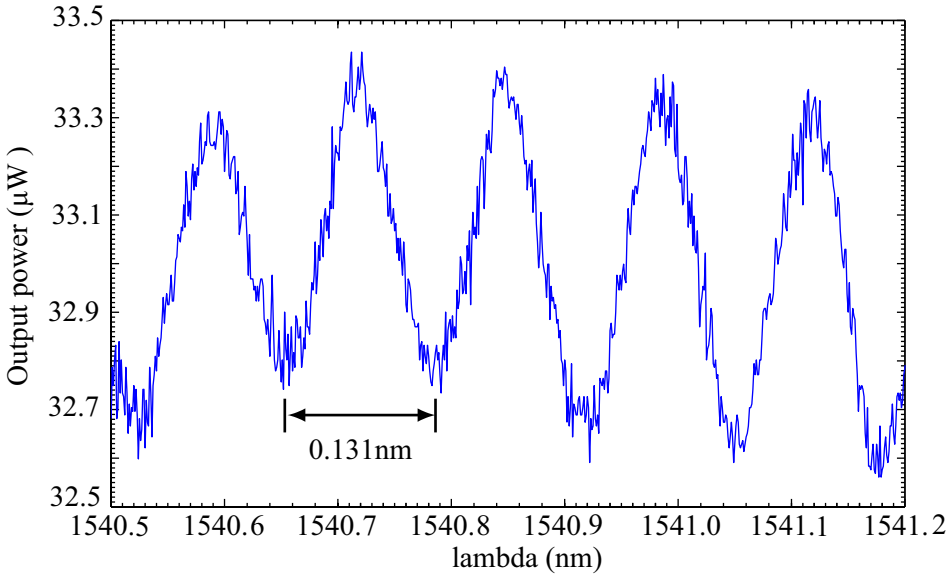

Figure 2.7: Transmission power fringes of 5.5-mm long porous silicon waveguide.

nique since it does not require the estimation of facet reflectivity. The transmitted power is measured while the input wavelength is scanned. Because of the reflectivity of the cleaved facets, the transmission spectrum shows a periodic sequence of peaks associated with the longitudinal modes of the Fabry-Pérot cavity. From the wavelength difference $\triangle\lambda$ between adjacent maximum or minimum transmitted power of the waveguide, the group index n_{eff} can be written by

$$n_{\text{eff}} = \frac{\lambda^2}{2\triangle\lambda L} , \tag{2.5}$$

where λ is the center wavelength of the wavelength-scanning range and L is the length of the waveguide. Figure 2.7 depicts the experimental results of the Fabry-Pérot measurement of 5.5-mm long porous silicon waveguide. The wavelength difference between adjacent minimum transmitted power was measured to be 0.131 nm . The corresponding group index of the waveguide was estimated to be 1.65.

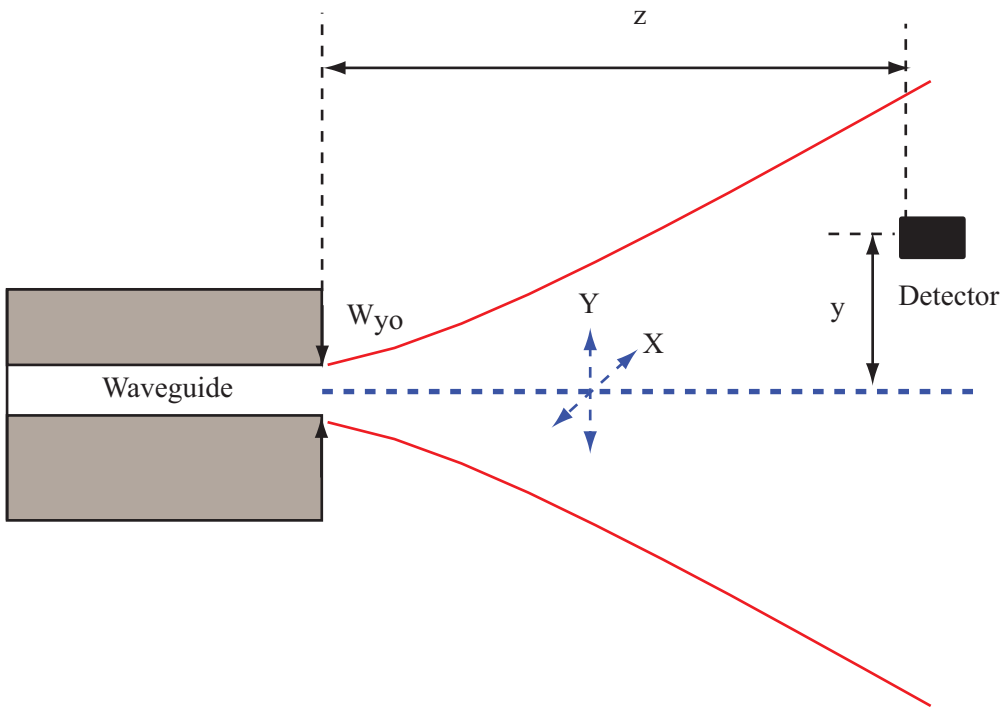

Figure 2.8: Experimental setup for estimating optical mode contours and effective area of porous silicon waveguide.

2.3.3 Optical Mode Contours and Effective Area Measurement

The refractive index profile of the porous waveguide defined by laser-induced oxidation is difficult to measure precisely, which makes numerical calculation of the optical mode challenging. Rather than simulating the electromagnetic mode, we estimate the mode size of porous silicon waveguide by measuring the far-field diffraction angles of light emerging from the porous waveguide. We assume, for simplicity, that light coming out of the waveguide has a two-dimensional elliptical Gaussian beam intensity profile. I.e, at the endfacet of the waveguide, the output intensity I can be approximated by

$$I(x,y) = I_{\mathrm{o}} \exp\left(-\frac{2x^2}{w_{\mathrm{xo}}^2} - \frac{2y^2}{w_{\mathrm{yo}}^2}\right) , \tag{2.6}$$

Where I_{o} is the maximum output intensity along the axis of the beam. x and y are two perpendicular distances away from the center axis of the beam. w_{xo} and w_{yo} are the beam waists along X and Y direction respectively. The output beam spreads out as it propagates away from the waveguide. At the distance z from the waveguide, the output intensity becomes

$$I(x,y,z) = I_{\mathrm{o}}(z) \exp\left(-\frac{2x^2}{w_{\mathrm{x}}^2(z)} - \frac{2y^2}{w_{\mathrm{y}}^2(z)}\right) , \tag{2.7}$$

where $w_{\mathrm{x}}(z)$ and $w_{\mathrm{y}}(z)$ are the beam waist at the distance z along X and Y direction respectively. $w_{\mathrm{x}}(z)$ and $w_{\mathrm{y}}(z)$ are related to the beam waists at the output facet of the waveguide w_{xo} and w_{yo} by following equations

$$w_{\mathrm{x}}^2(z) = w_{\mathrm{xo}}^2 \left[1 + \left(\frac{z}{z_{\mathrm{xo}}}\right)^2\right] \tag{2.8}$$

$$w_y^2(z) = w_{yo}^2 \left[1 + \left(\frac{z}{z_{yo}} \right)^2 \right] , \tag{2.9}$$

where $z_{xo} = \frac{\pi w_{xo}^2}{\lambda}$ and $z_{yo} = \frac{\pi w_{yo}^2}{\lambda}$ are confocal beam parameters along X and Y direction, respectively.

We measured the diffracted beam emerging from the waveguide in both the X and Y directions and inferred the beam waists at the facet of the waveguides using Gaussian beam propagation as described in Eq. (2.8)-(2.9). The experiment setup is shown in Fig. 2.8. The TE-polarized, continuous-wave input signal at the wavelength of 1550 nm was coupled to the porous silicon waveguide with 20-μm line spacings. The transmitted intensity profile was measured at the distance z from the facet. The detector was moved along the X and Y directions using a translation stage. Since the detector size is much smaller than the diffracted beam size, the detected optical power represents the beam intensity at each point in the far field. Figure 2.9 depicts the measured intensity profiles of transmitted light in both the X (a) and Y (b) directions. The beam waists of the diffracted beam 5.7 cm away from the waveguide facet were estimated by a nonlinear least squares fit to Eq. (2.7) and were found to be 7.7 mm and 14.4 mm , corresponding to w_{xo} and w_{yo} of 3.4 μm and 1.8 μm, respectively.

The nonlinear effective area A_{eff} is given by

$$A_{eff} = \frac{\left[\int_{-\infty}^{\infty} E(x,y)^2 dxdy \right]^2}{\int_{-\infty}^{\infty} E(x,y)^4 dxdy} , \tag{2.10}$$

where $E(x,y)$ is the electric field profile of the fundamental mode of the waveguide. For the waveguide with the fundamental mode approximated by a Gaussian beam intensity profile described in Eq. (2.6), the effective area could be integrated analytically to be

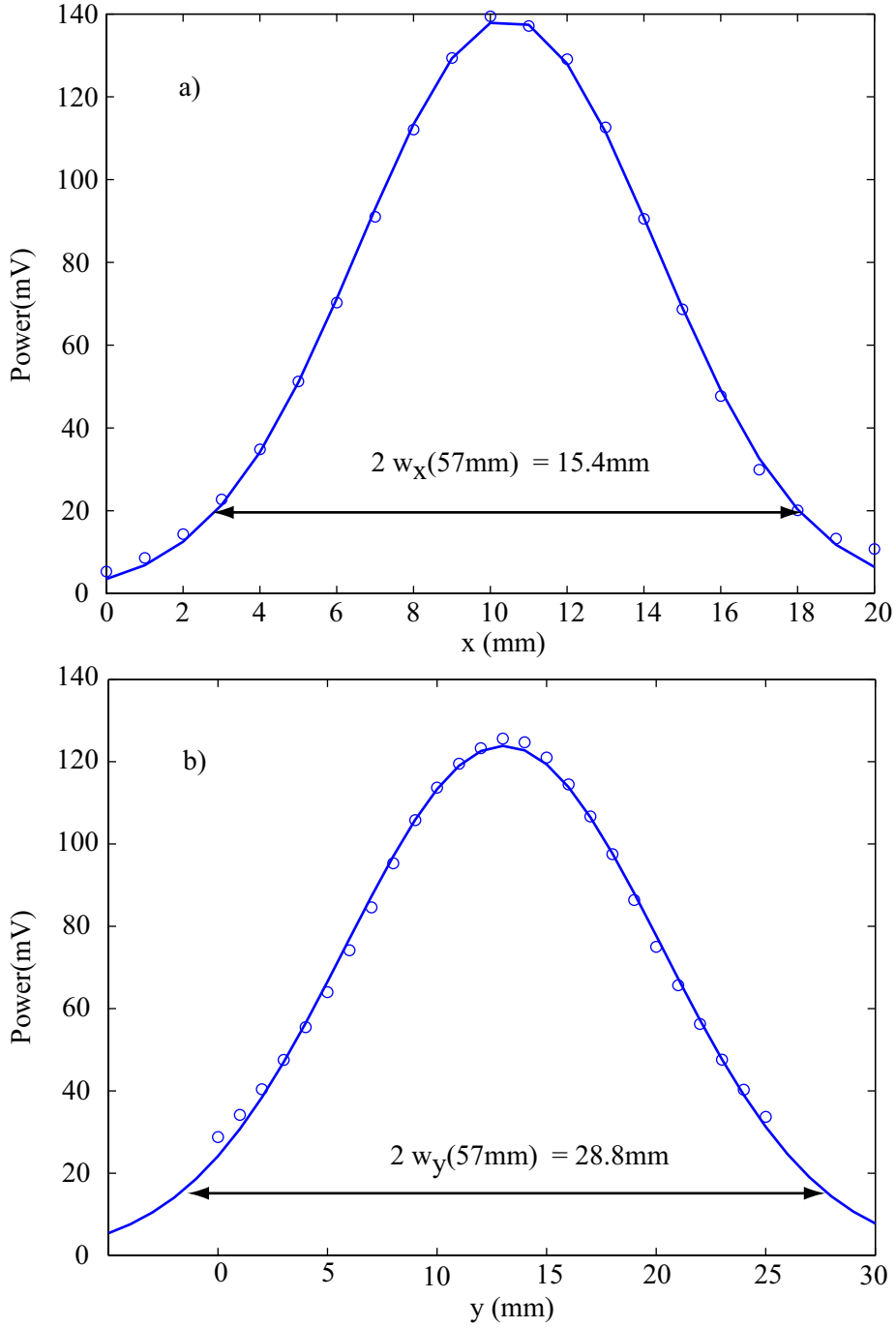

Figure 2.9: Measurements of diffracted beam profile and best-fit Gaussian of the output intensity at 5.7 cm away from the porous silicon waveguide. (a) In the X direction. (b) In the Y direction.

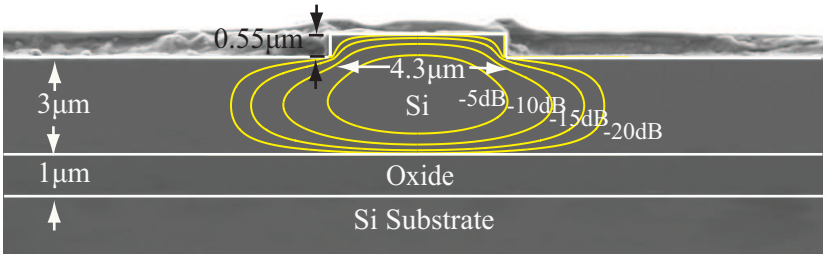

(a)

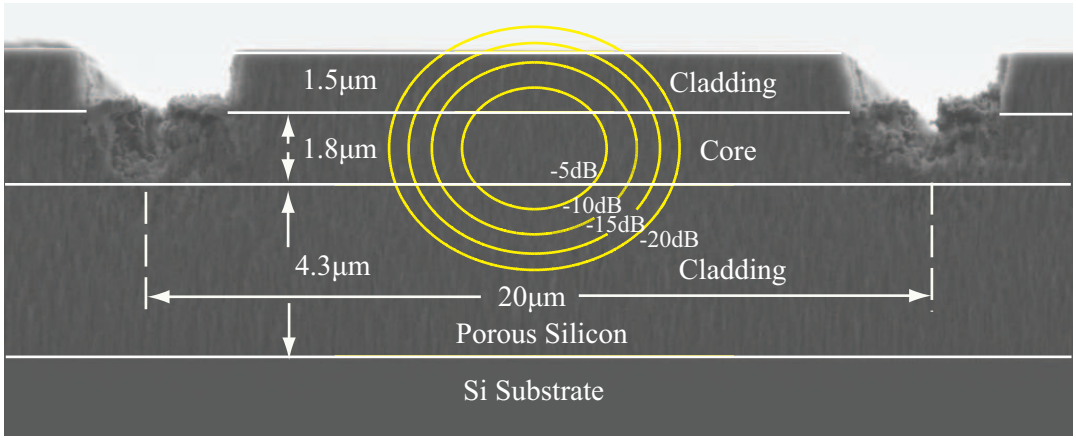

(b)

Figure 2.10: Scanning electron micrographs comparing the cross sections of (a) silicon on insulator ridge waveguide and (b) porous silicon waveguide.

$A_{\text{eff}} = \pi w_{\text{xo}} w_{\text{yo}}$. The effective area of the porous silicon waveguide with 20-μm line spacing was therefore estimated to be 19.3 μm^2.

For comparison, we also measured linear characteristics in a conventional silicon-on-insulator ridge waveguide, which was fabricated using photolithography and reactive ion etching of commercially-available silicon-on-insulator substrates (for details, see [45].) Figure 2.10(a) shows cross-sectional scanning electron micrographs of the SOI ridge waveguide in comparison to the porous silicon waveguide used in the experiment.

The mode contours that are superposed on the micrograph in Fig. 2.10(a) were

parameter	SOI ridge waveguide	porous silicon waveguide	(unit)
n_{eff}	3.49	1.65	—
A_{eff}	10.0	19.3	(μm^2)
L	17	5.5	(mm)
α	3–5	9–13	(dB/cm)
$L_{\text{eff}} \equiv (1-e^{-\alpha L})/\alpha$	7.5–10	2.7–3.3	(mm)
Insertion loss	20.2	15.3	(dB)

Table 2.1: Mode parameters and linear properties of SOI ridge waveguide and porous silicon waveguide.

numerically calculated using the known refractive indices and measured waveguide dimensions of the SOI ridge waveguide. The contours shown in Fig. 2.10(b) indicate the approximate two-dimensional Gaussian mode shape baesd on the measured beam waists w_{xo} and w_{yo}. The two micrographs are shown to scale (i.e., with identical magnification), to emphasize the similarity in mode size.

Table 2.1 summarizes the important linear characteristics of the two waveguides considered here. As previously mentioned, the group index n_{eff} and loss coefficient α were estimated using a combination of Fabry Pérot spectral measurements and scattering light measurement. The effective area of the TE mode of the porous silicon waveguide was estimated to be approximately $2\times$ larger than that of the silicon-on-insulator waveguide. The total insertion losses listed in Table 2.1 include the propagation loss, the coupling loss between the aspheric lens and the front facet and the coupling loss between the lensed fiber and the rear facet of the waveguide.

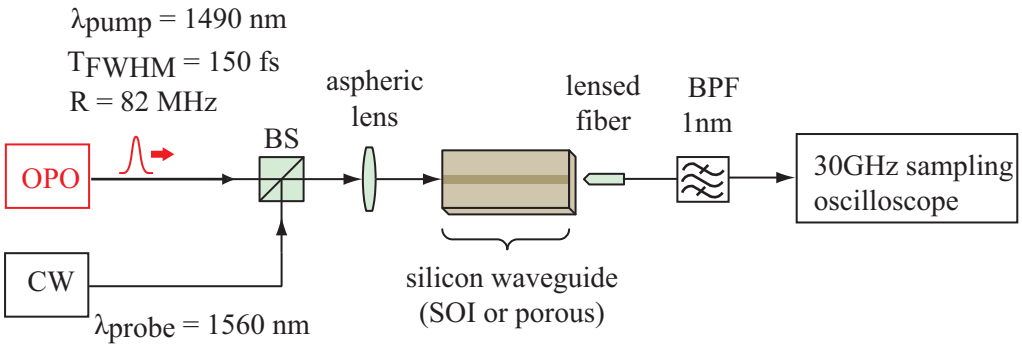

Figure 2.11: Experimental setup for measuring free-carrier lifetime in SOI waveguides and porous silicon waveguides. (OPO : optical parametric oscillator; BS : beam splitter; BPF : bandpass filter)

2.4 Free-Carrier Lifetime Measurement

One of the key parameters that govern the operation of optoelectronic devices is the excess carrier lifetime τ_c. We measured the carrier lifetime for both porous silicon waveguides and crystalline silicon waveguides using a pump-probe experiment. Figure 2.11 depicts the experimental setup used to measure free-carrier lifetime. A Ti:sapphire-pumped optical parametric oscillator was used to deliver 150 fs pump pulses at a repetition rate of 82 MHz with center wavelength of 1490 nm, which generates free-carriers in the waveguide through two-photon absorption. The probe signal was a continuous wave, co-propagating laser with a wavelength of 1560 nm. The pump and probe were combined using a beamsplitter and coupled from free-space into the waveguides using an aspheric lens. The average coupled input powers for the pump and probe were estimated to be 10 mW and 1 mW, respectively. The light emerging from the waveguide was collected using a lensed fiber and was bandpass-filtered to isolate the probe signal spectrally. The probe

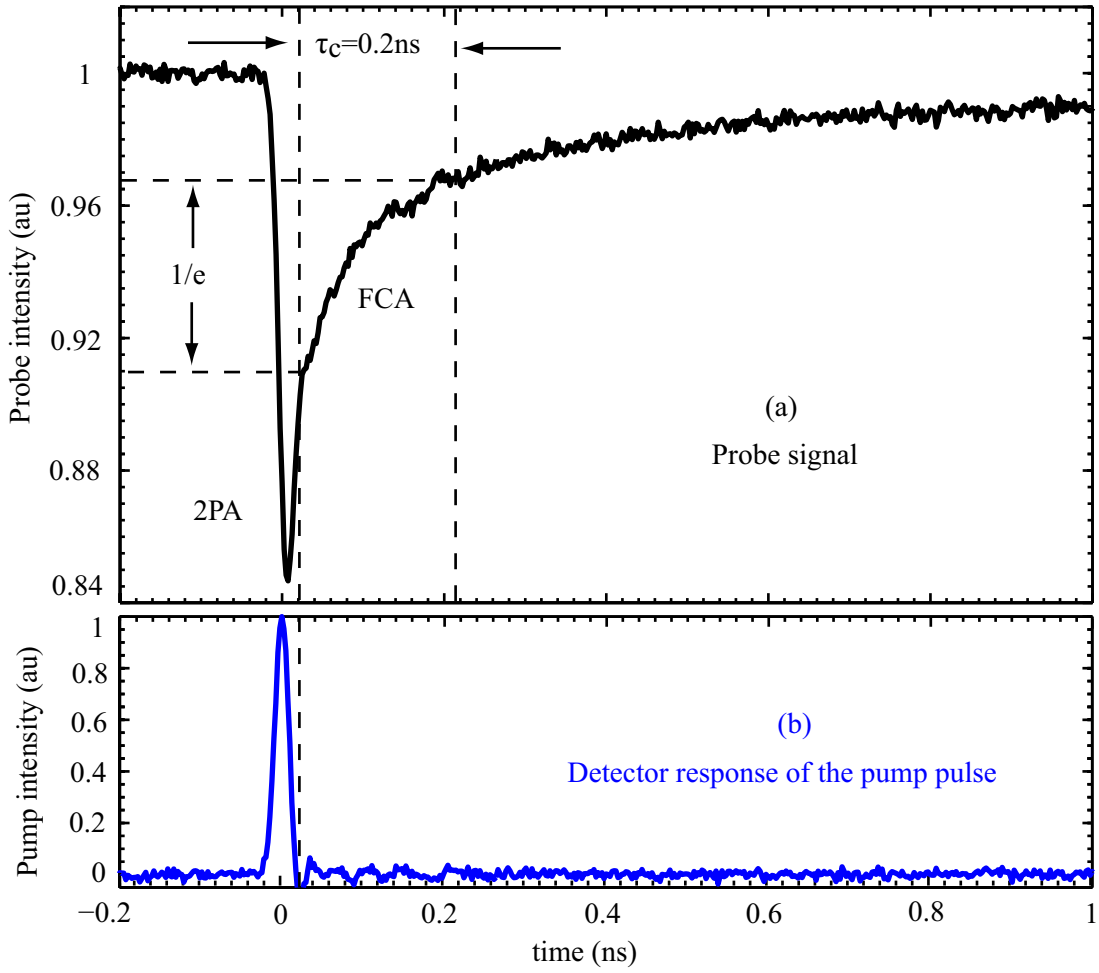

Figure 2.12: (a) Free-carrier lifetime measurement of porous silicon waveguide. (b) Impulse response of the photodetector.

signal was observed on a 30-GHz bandwidth optical sampling oscilloscope to monitor the transient change in transmission caused by free-carrier absorption.

Figure 2.12(a) plots the transmitted probe signals from porous silicon waveguides. The measured probe signal is normalized to their CW values in the absence of a pump pulse. The transmitted probe exhibits a sharp, impulse-like dip followed by a slower asymptotic recovery.

The initial dip in transmission can be attributed to pump-induced two-photon ab-

sorption, i.e., simultaneous absorption of one pump photon and one probe photon. Because two-photon absorption is an ultrafast nonlinear process, the duration of this dip should closely match the input pump pulse shape. Figure 2.12(b) plots the measured impulse response of the photoreceiver. The detector response is estimated to be 30 ps, which is not fast enough to resolve the depth or duration of this instantaneous dip.

The slower recovery time is attributed to optical absorption by free-carriers, which remain in the waveguide even after the pump pulse has passed. As described by Eq. (2.2a), the excess absorption is proportional to the carrier population, and therefore the observed recovery time in transmission gives a direct measurement of the free-carrier lifetime. We obtain an estimate of the free-carrier lifetime by measuring the $1/e$ recovery time, after neglecting the initial impulse contribution from two-photon absorption. The porous silicon waveguide exhibits a carrier lifetime of approximately 200 ps.

The measured carrier recovery trace shown by a solid line shown in Fig. 2.13(a), does not match with an estimated exponential recovery, shown by the dashed line. Figure 2.13(b) plots the fractional absorption of the probe signal, on a semilogarithmic scale. The fractional absorption clearly does not exhibit the linear decrease, when plotted on a logarithmic scale, which suggests that more than one physical process contributes to the carrier recombination. The combination of the surface recombination and the slower bulk carrier recombination could contribute to the free-carrier recombination. We believe that carrier diffusion does not play an important role in the free-carrier lifetime in the porous silicon waveguide since the diffusion length is likely to be shorter than the waveguide cross-section based on the carrier diffusion coefficient reported in [46]. Nonetheless, we obtain an estimate of the free-carrier lifetime using a single time constant by measuring

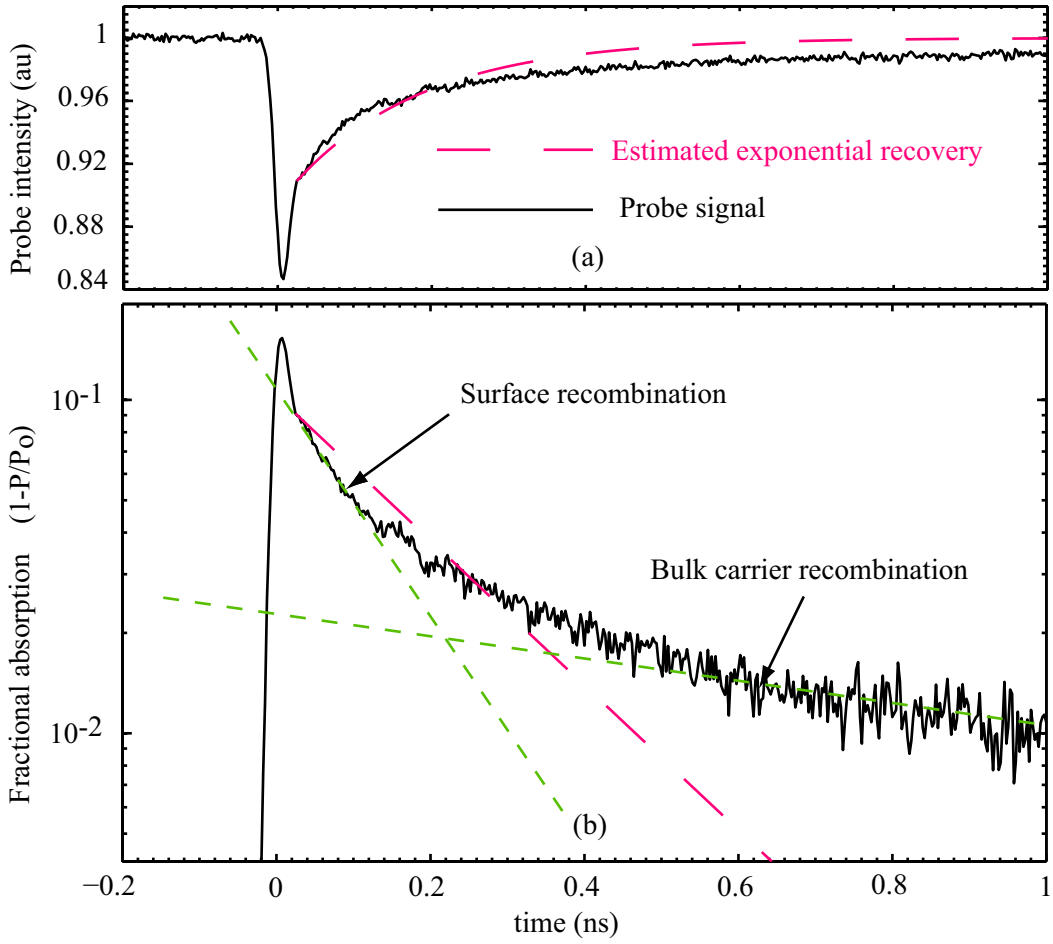

Figure 2.13: (a)The free-carrier lifetime recovery trace in porous silicon waveguides. (b) The fractional of absorption of the probe pulse in logarithmic scale. The solid line corresponds to the actual recovery while the dashed line corresponds to the estimated exponential recovery.

the $1/e$ recovery time as previously mentioned.

For comparison, we measured the free-carrier lifetime in SOI waveguide conducted in a similar measurement. The inset in Fig. 2.14(a) shows an enlarged view of the first 1.5 ns after arrival of the pump pulse. The SOI ridge waveguide exhibits a carrier lifetime of approximately 1.1 ns, which is consistent with earlier measurements reported for similar silicon waveguides [47]. Compared to the free-carrier lifetime of 200 ps in porous silicon waveguide, which has a comparable mode area to the SOI waveguide, porous silicon has a faster free-carrier lifetime. This could be explained by the much higher surface recombination rate in the nanoporous material as well as the much faster Auger recombination lifetime in the heavily doped material. We note that in both cases, the observed carrier lifetime is much shorter than the repetition rate of the pump laser, which allows us to neglect the cumulative buildup of free-carriers generated by prior pulses.

2.5 Nonlinear Measurements

2.5.1 Nonlinear Absorption

The instantaneous and carrier-based nonlinear properties were determined by launching pulses into the waveguide and measuring the output power and output spectrum as a function of the input optical power. For low input power, the output power is directly proportional to the input power and the output spectrum has the same shape as the input spectrum. As the input power is increased, the ratio of transmitted to input power decreases as a result of two-photon absorption and free-carrier absorption. Similarly, at higher input power, the output spectrum broadens and shifts as a result of the self-phase

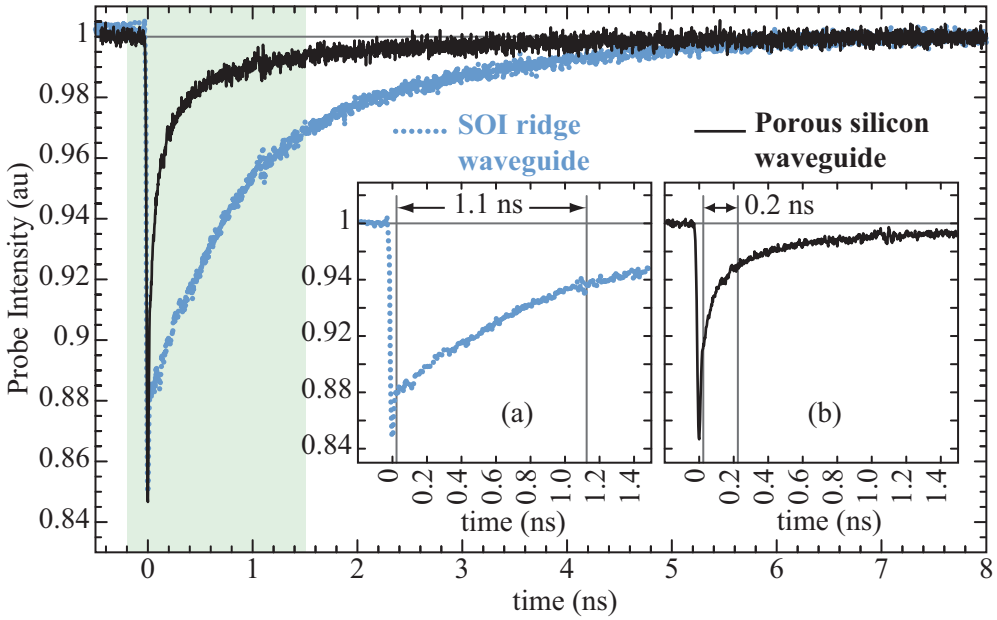

Figure 2.14: Free-carrier lifetime measurements of silicon waveguide and porous silicon waveguide. Inset: (a) zoomed in plot for the silicon waveguide, and (b) zoomed in plot for the porous silicon waveguide.

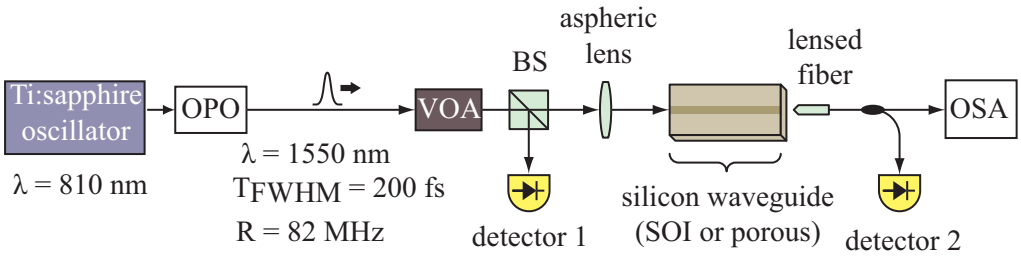

Figure 2.15: Experimental setup for measuring optical nonlinear parameters in SOI waveguides and porous silicon waveguides. (OPO : optical parametric oscillator; VOA : variable optical attenuator; BS : beam splitter; OSA : optical spectrum analyzer)

modulation and free-carrier dispersion.

Figure 2.15 depicts the experimental setup used to observe these nonlinear effects [48]. The input pulses were generated using a Ti:sapphire-pumped optical parametric oscillator, which produced transform-limited 200 fs pulses with a center frequency of 1550 nm and repetition rate of 82 MHz. The input power was adjusted using a variable attenuator, and coupled from free space into the waveguide through a high numerical aperture aspheric lens. In all measurements, the input polarization state was adjusted to excite only the TE mode of the waveguide. The light emerging from the waveguide was collected using a tapered single-mode optical fiber and directed to either an optical spectrum analyzer or a power meter.

The open squares in Fig. 2.16 show the measured output power vs. input power for the SOI ridge waveguide depicted in Fig. 2.2(a). For this waveguide, the maximum average coupled input power was 5.4 mW, which corresponds to a peak intensity of 3 GW/cm^2. The power transmission ratio decreases at higher input power, as evidenced by the downward curvature in the plot of P_{out} vs. P_{in}. The theoretical curves shown in Fig. 2.16 were obtained by numerically solving Eqs. (2.1)-(2.3). When performing the numerical simulations, we used previously measured values for α, and adjusted $\beta_{2\text{PA}}$ and σ_{FCA} in order to best fit the experimental measurements.

In the SOI waveguide, we found that at the optical intensities considered here, the nonlinear relationship between P_{out} vs. P_{in} can be almost entirely described by instantaneous two-photon absorption, with very little contribution from free carriers. The dashed curve shown in Fig. 2.16 was obtained by neglecting free-carrier absorption in the simulation (i.e., by setting $\sigma_{\text{FCA}} = 0$), which gives results that are almost indistinguishable from

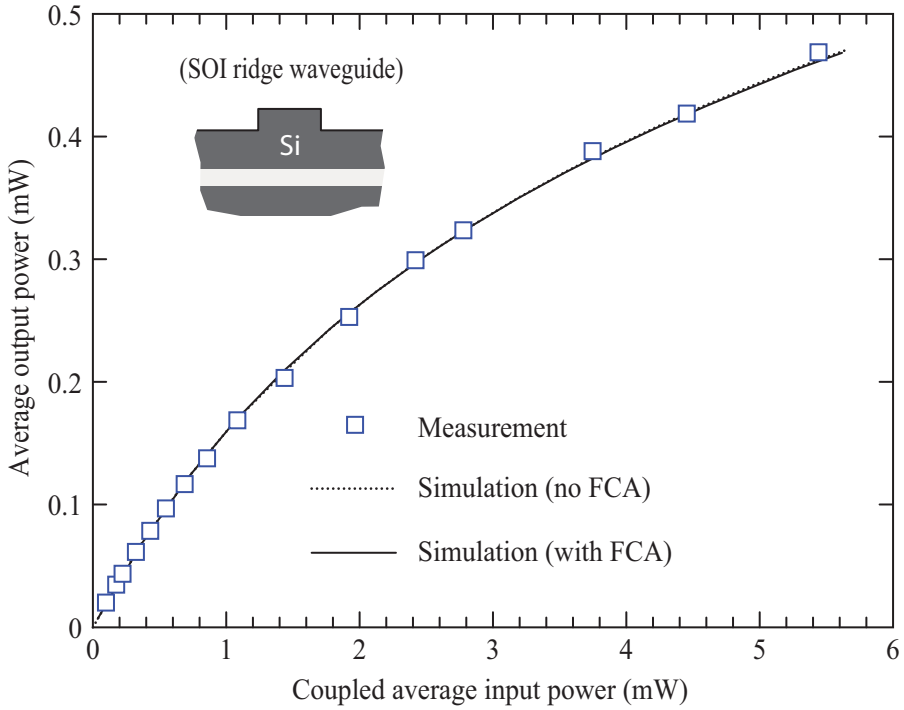

Figure 2.16: Output power vs. input coupled power for the SOI ridge waveguide waveguide. The open squares indicate the measured data, whereas the curves show theoretical fits obtained from numerical simulation. The dashed curve indicates the fit obtained by neglecting free-carrier effects, whereas the solid curve includes both two-photon absorption and free-carrier absorption.

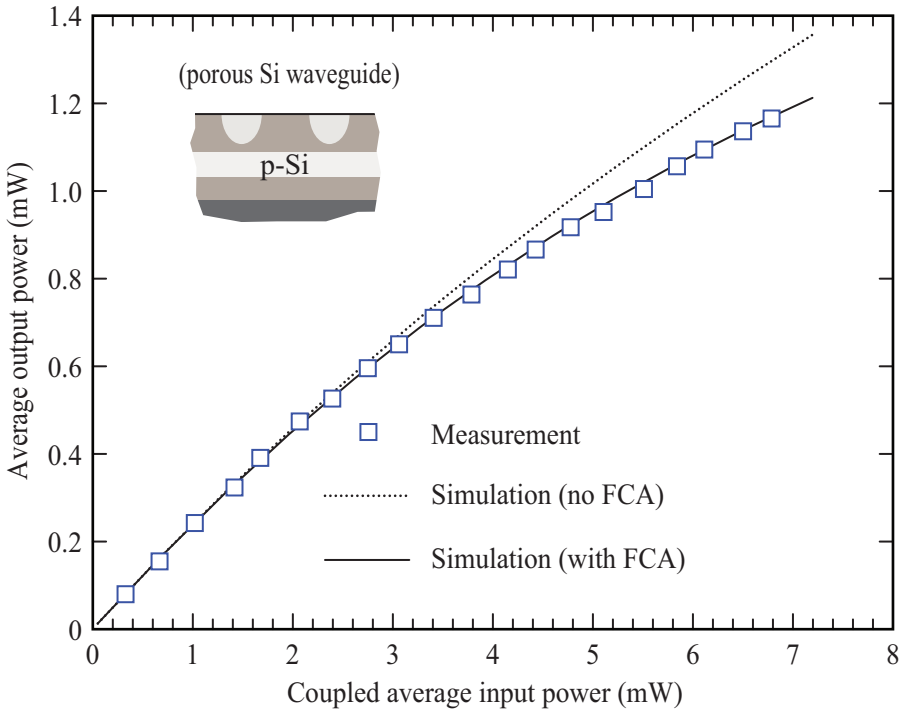

Figure 2.17: Output power vs. input coupled power for the porous silicon waveguide waveguide. The open squares indicate the measured data, whereas the curves show theoretical fits obtained from numerical simulation. The dashed curve indicates the fit obtained by neglecting free-carrier effects, whereas the solid curve includes both two-photon absorption and free-carrier absorption.

the solid curve, which used the previously reported value $\sigma_{\mathrm{FCA}} = 1.45 \times 10^{-17}$ cm^2 [35]. We therefore conclude that for the SOI waveguide, the measurement of P_{out} vs. P_{in} alone does not permit accurate determination of the free-carrier absorption cross section. By fitting the simulations and experiments, we estimated the two-photon absorption coefficient of silicon to be $\beta_{\mathrm{2PA}} = 1 \pm 0.25$ cm/GW, which is consistent with previously reported measurements in silicon [17, 32]. The uncertainty in our estimate of β_{2PA} is attributed primarily to uncertainty in the coupling efficiencies at the input and output facets.

Figure 2.17 shows a similar measurement performed on the porous silicon waveguide shown in Fig. 2.2(b). In this case, the maximum attainable average coupled input power was 7 mW, which corresponds to a peak intensity of 2 GW/cm^2. As with the SOI ridge waveguide, the power transmission ratio decreases at high intensity due to nonlinear absorption. In this case, however, the measured data cannot be explained without including free-carrier absorption. The dashed curve shows a best-fit simulation neglecting free-carrier absorption, whereas the solid curve includes both two-photon absorption and free-carrier absorption, and gives excellent agreement with the observations. From this fit, the 2PA coefficient and free-carrier absorption cross section in porous silicon waveguide were estimated to be 0.8 ± 0.1 cm/GW and $(100 \pm 20) \times 10^{-17}$ cm^2, respectively. Even though the waveguides are 70-80% porous, the 2PA coefficient in porous silicon is only slightly lower than the value in silicon. Surprisingly, the free-carrier absorption cross section in porous silicon waveguide is approximately two-orders-of-magnitude larger than what is reported for bulk silicon [35], as summarized in Table 2.3. The anomalously high free-carrier cross section could be explained by the higher collision frequency due to the lower mobility of the heavily-doped porous silicon skeleton.

2.5.2 Nonlinear Refraction

Figure 2.18 plots the measured (a) and simulated (b) output optical spectrum from the SOI ridge waveguide, measured for three different input intensities. The input intensities were calculated based on the coupled input power and effective mode area of the SOI waveguide. In order to better compare the spectral shapes, all three of the spectra

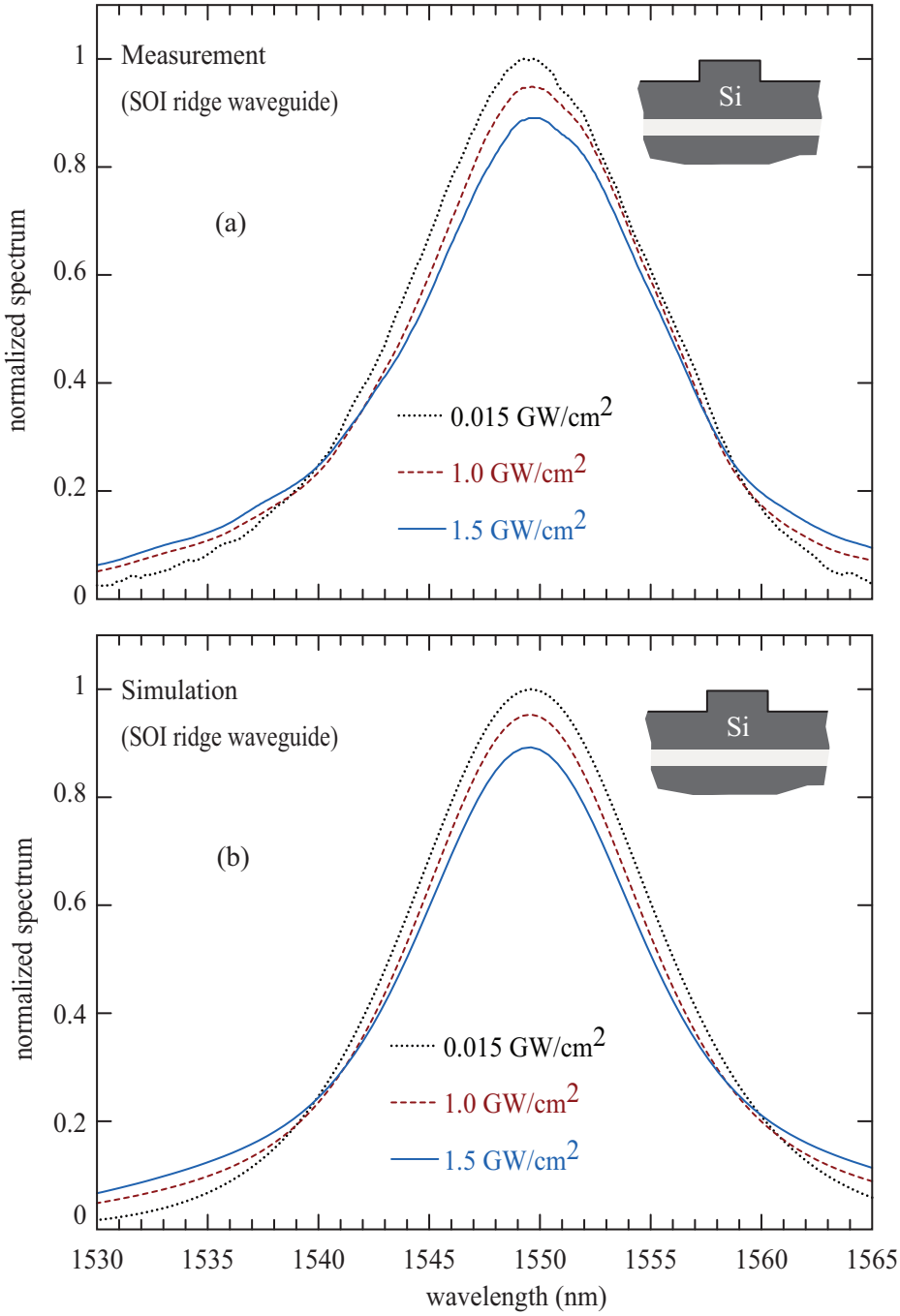

Figure 2.18: (a) Experimentally measured output spectra for three different input intensities for the SOI ridge waveguide, showing spectral broadening caused by self-phase modulation. (b) Corresponding numerical simulations used to match the measurements.

Optical Kerr coefficient (cm^2W^{-1})	wavelength (nm)	Reference	Method
6×10^{-14}	1536	[50]	Self-phase modulation
4.5×10^{-14}	1540	[17]	z-scan
7×10^{-14}	1530	[32]	Spectral transmission
3.7×10^{-14}	1559	[47]	Self-phase modulation
9×10^{-14}	1547	[51]	Four-wave mixing
4.5×10^{-14}	1550	[52]	Four-wave mixing
14.5×10^{-14}	1550	[53]	Self-phase modulation
5×10^{-14}	1500	[54]	Self-phase modulation
6×10^{-14}	1550	[55]	z-scan
2.8×10^{-14}	1500	[56]	z-scan
4.2×10^{-14}	1550	This work	Spectral transmission

Table 2.2: Published values of the optical Kerr coefficient of silicon.

were normalized to have the same integrated power. As the input intensity is increased, the output spectrum broadens slightly as a result of self-phase modulation. The spectral broadening can be entirely described by the inclusion of self-phase modulation (n_2) in the simulation. As with the nonlinear absorption measurements, the inclusion of free-carrier effects in the model was found to have no clearly discernable effect on the simulated spectra, for the parameters considered here. By matching simulations and measurements, we estimated nonlinear refractive index for silicon to be $n_2 = (4.2 \pm 0.8) \times 10^{-14}$ cm^2/W, which agrees with the results reported in the literature as listed in Table 2.2 [49].

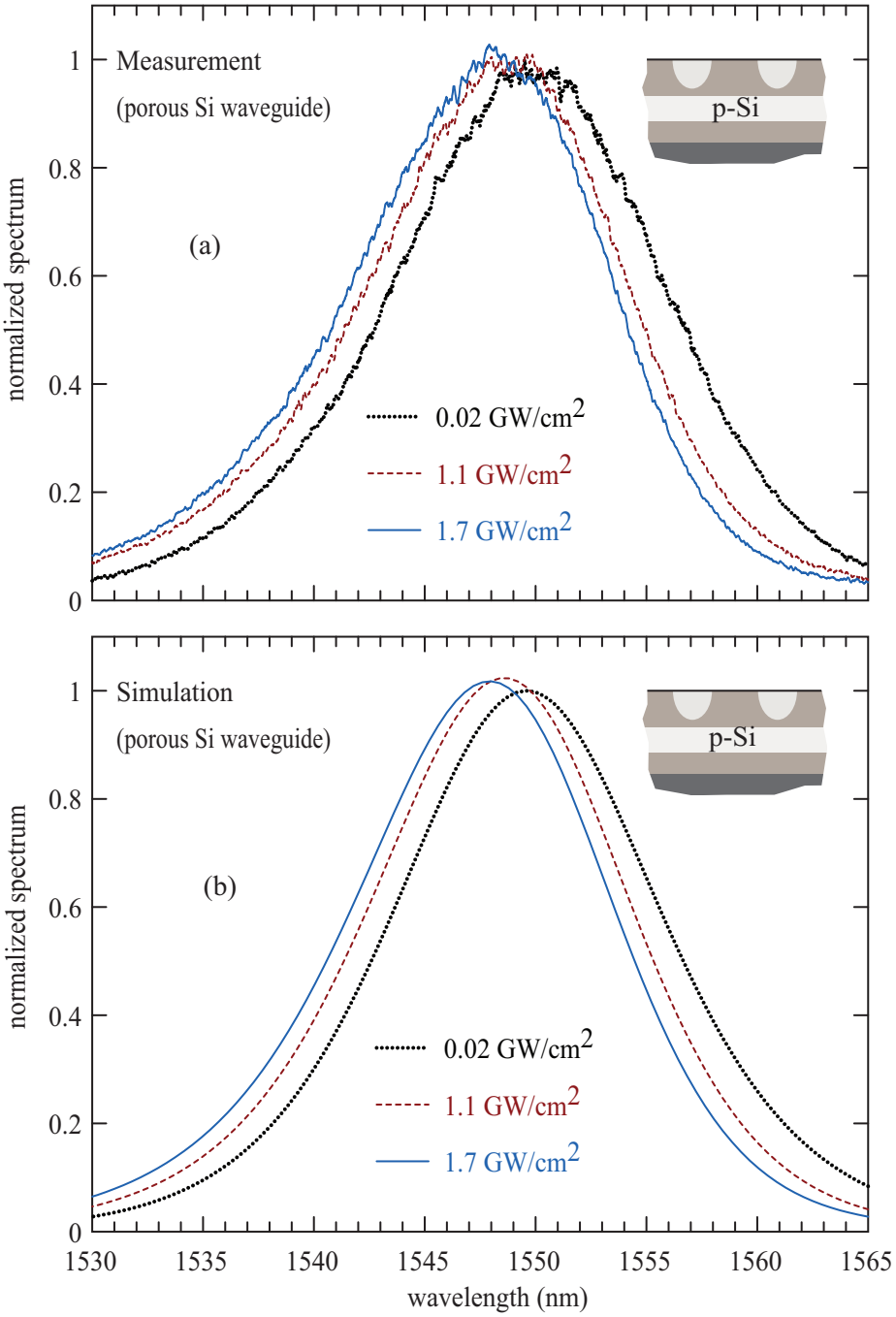

Figure 2.19: (a) Experimentally measured output spectra for three different input intensities, for the porous silicon waveguide, showing blue-shift associated with free-carrier dispersion. (b) Corresponding numerical simulations.

Figure 2.19 plots similar spectral measurements (a) and simulations (b) for the porous silicon waveguide considered here. In this case, the spectrum exhibits a pronounced blue shift at higher input intensities, which is a signature of free-carrier dispersion. By fitting the blue-shift to the theoretical models, we determined the free-carrier dispersion coefficient to be $k_{\mathrm{FCD}} = (90 \pm 15) \times 10^{-21}$ cm^3. As indicated in Table 2.3, this figure is more than an order of magnitude higher than what is reported for crystalline silicon [34, 35].

Aside from the blue-shift, the spectrum shows very little change in width as the power is increased, which suggests that the self-phase modulation does not play an important role. However, through a careful analysis we found that the simulations cannot be made to match the experiments without also including self-phase modulation terms (n_2). If SPM terms are neglected, but two-photon absorption terms are included, then the spectrum would become narrower at higher intensities, as a result of 2PA-induced pulsewidth spreading. The inclusion of SPM causes spectral broadening, which counteracts the spectral narrowing caused by 2PA. By modeling both effects, we were able to match the experimentally observed spectra, from which we estimate the nonlinear refractive index of porous silicon to be $n_2 = (2.3 \pm 0.7) \times 10^{-14}$ cm^2/W. We emphasize that this estimate requires finding a self-consistent fit to both the spectral measurements in Fig. 2.19 and the transmission measurements in Fig. 2.17. Despite a high porosity of 70-80%, the porous silicon exhibits a nonlinear refractive index that is comparable in magnitude to that of crystalline silicon, as summarized in Table 2.3.

parameter	SOI ridge waveguide	porous silicon waveguide	(unit)
τ_c	1.1	0.2	(ns)
β_{2PA}	1 ± 0.25	0.8 ± 0.1	(cm/GW)
n_2	4.2 ± 0.8	2.3 ± 0.7	($\times 10^{-14}$ cm^2/W)
σ_{FCA}	1.45 [a]	100 ± 20	($\times 10^{-17}$ cm^2)
k_{FCD}	3.5–7.5[b]	90 ± 15	($\times 10^{-21}$ cm^3)

Table 2.3: Comparison of nonlinear properties measured from crystalline SOI ridge waveguide and porous silicon waveguide.

[a] For the SOI ridge waveguide, the value of σ_{FCA} could not be reliably estimated from our measurements. For comparison, we tabulate here the accepted value of σ_{FCA} for crystalline silicon, as reported in the literature [34, 35].

[b] For the SOI ridge waveguide considered here, the value of k_{FCD} was too small to be reliably determined from our measurements. The range tabulated here was calculated using the empirical model given in [35], for carrier concentrations in the range 10^{15}–10^{17} cm^{-3}.

2.6 Summary

We report here the first experimental measurement of the instantaneous and carrier-based nonlinear effects in porous silicon waveguides at 1550 nm. We used a combination of three different measurements: pump-probe transient absorption, nonlinear changes in the transmitted power and nonlinear changes in the transmitted spectrum. By matching these measurements against numerical simulations, we estimated the coefficients that describe two-photon absorption, self-phase modulation, free-carrier absorption, free-carrier dispersion, and carrier lifetime. For comparison, and to confirm the credibility of our models, we conducted identical measurements on a conventional silicon-on-insulator ridge waveguide, which gave results consistent with those that have been reported in the literature.

The instantaneous nonlinear parameters that describe self-phase modulation and two-photon absorption (n_2 and β_{2PA}) in porous silicon were found to be comparable in magnitude to those reported in the literature (and confirmed by our measurements) for crystalline silicon waveguides. These results are surprising because the porous waveguides considered here are comprised of 70–80% air and only 20–30% silicon, and for the TE-polarized mode, the optical mode is expected to strongly concentrate in the low-index air voids [57].

The carrier-based nonlinearities in porous silicon are markedly stronger and faster in porous silicon, compared to what has been reported for crystalline silicon. The carrier lifetime in porous silicon is significantly shorter than in conventional silicon waveguides, which we attribute to the very high surface-area of the nanoporous skeleton. The Drude

coefficients that best describe the plasma dispersion effect in porous silicon are found to be much larger than what has been reported earlier for crystalline silicon. The physical origin of this anomaly merits further investigation, but it could be related to the dramatically altered mobility in nanoscale composites, or the high doping concentration of the porous silicon used here.

These results suggest that porous silicon could be an interesting alternative to crystalline silicon for future applications in all-optical switching or fast electrooptic modulators.

Chapter 3

Fabrication and Characterization of Gallium Arsenide Waveguides

In this chapter, we describe the fabrication and the measurements of GaAs waveguides. We start by explaining the fabrication process of the GaAs waveguides that we use in wavelength conversion experiments in chapter 4. Next, we describe how we fabricated the waveguide-based two-photon absorption detectors that we use in chapter 5. Finally, we characterize mode parameters and optical properties of passive GaAs waveguides and GaAs waveguide detectors.

GaAs/AlGaAs waveguides provide interesting optical properties for nonlinear optical signal processing. The optical Kerr coefficient (nonlinear refractive index) n_2 of GaAs is approximately 4 times larger than that of crystalline silicon [17] and three orders of magnitude larger than that of standard optical fiber. Table 3.1 compares parameters such as propagation loss (α), optical Kerr coefficient (n_2) and nonlinear parameter (γ) of some of the nonlinear waveguides that have been proposed for optical signal processing.

One of the parameters used to evaluate the efficiency of third-order-nonlinearity-based waveguide devices is the nonlinear parameter γ, which depends not only on material nonlinearity (n_2), but also on the geometry of the waveguide. γ is defined as [39].

$$\gamma = \frac{2\pi n_2}{\lambda A_{\text{eff}}}, \tag{3.1}$$

where λ is the signal wavelength, and A_{eff} is the effective area of the waveguide. Note

Waveguide devices	α dB/cm	n_2 cm^2/W	A_{eff} μm^2	γ W^{-1}m^{-1}
Standard fiber (SMF-28) [58]	5×10^{-7}	2.2×10^{-16}	80	1.1×10^{-3}
Bismuth-Oxide fiber [59, 60]	3×10^{-2}	8.2×10^{-15}	3	1.1
Chalcogenide fiber taper [61]	1.7	1.1×10^{-13}	0.64	68
Chalcogenide waveguide [8]	0.2	3×10^{-14}	7.2	1.7
Organic $\chi^{(3)}$ in slot waveguide [6]	23	8.2×10^{-15}	0.1	104
Silicon nanowire [17, 62]	3.6	4.5×10^{-14}	0.14	130
AlGaAs nanowire [17, 21]	82.5	1.5×10^{-13}	0.3	202
GaAs ridge waveguide (this work)	4–6	2.9×10^{-13}	1.8	64

Table 3.1: Comparison among parameters in nonlinear waveguide devices

that for nanoscale semiconductor waveguides, this nonlinear factor (γ) has to to be re-defined to take into account the tensor nature of the third-order nonlinear susceptibility ($\chi^{(3)}$), the direction of propagation relative to the crystal axes and the vector nature of the electromagnetic mode, including non-zero z-components of the electric field [54, 63]. The nonlinear efficiency could be improved by using a material with large nonlinearity or by reducing the guided-mode area of the waveguides. However, the linear propagation loss and 2PA could impede the nonlinear interaction in the waveguide as the guided-mode area gets smaller.

In addition to the nonlinearity parameter (γ), another figure of merit that has been used to compare the nonlinearity in different materials and waveguides is FOM_{2PA}. FOM_{2PA} takes into account the two photon absorption loss (β_{2PA}) in addition to the nonlinearity

(n_2), which is defined as [64]

$$\mathrm{FOM}_{2\mathrm{PA}} = \frac{n_2}{\lambda \beta_{2\mathrm{PA}}} \,. \tag{3.2}$$

The GaAs/AlGaAs material system could be designed to achieve a large $\mathrm{FOM}_{2\mathrm{PA}}$. This material alloy allows for band-gap engineering: by adding Al into AlGaAs, the energy bandgap of AlGaAs can be altered. For example, the bandgap energy of AlGaAs can be designed such that the photon energy of the optical signal at communication wavelengths falls below the half-bandgap, thus avoiding two-photon absorption, while maintaining a large optical Kerr coefficient. GaAs waveguides could also allow for integration of nonlinear optical devices with optically active devices such as lasers, amplifiers, detectors and modulators [65].

A variety of GaAs/AlGaAs waveguide devices have been reported, including directional couplers [66], microring resonators [12, 67] and photonic crystal cavities [20]. Several groups have also reported GaAs and AlGaAs nanowire waveguides [21, 68–70]. A cross-section as small as 0.2 μm^2 has been achieved [71]. The linear propagation loss for these nanowire waveguides is approximately 50 dB/cm, which is still too high for practical nonlinear applications in these nanowire waveguides. Recently, GaAs/AlGaAs waveguides with an effective area of 0.4 μm^2 have been demonstrated with propagation loss as low as 0.9 dB/cm at 1550 nm [22].

In this chapter, we describe a process of fabricating passive GaAs/AlGaAs ridge waveguides using in a single contact-photolithographic step. As we will show in the next chapter, these GaAs/AlGaAs waveguides could be used for 10-Gb/s all-optical wave-

length conversion. We also describe the fabrication of waveguide-based two-photon absorption detectors that are used in chapter 5. The linear and nonlinear properties of these waveguides are also characterized.

3.1 Fabrication of Passive GaAs Waveguides

Figure 3.1 shows a cross-section of the material layer of our waveguide structure. Its epistructure was grown by molecular-beam epitaxy on a n-GaAs substrate. The structure comprises a 0.8-μm-thick GaAs guiding layer surrounding by a 1-μm-thick $Al_{0.2}Ga_{0.8}As$ upper cladding and a 3.5-μm-thick $Al_{0.2}Ga_{0.8}As$ lower cladding. The layer thicknesses were to ensure single-mode operation and to minimize leakage loss to the substrate. This structure was originally conceived as a p-i-n waveguide photodetector, but we also used the same epistructure to make a passive waveguide. Both parts of the top and bottom cladding layers, which are close to the core, are left undoped in order to help suppress free-carrier absorption (FCA) loss.

A 2.4-μm wide ridge waveguide was fabricated in a single photolithography step. First, we spin a 2000-nm positive photoresist (PR1-2000A) on a small cleaved sample (typically 1.5 cm $\times$ 1.5 cm). Next, the waveguide patterns are exposed using UV contact photolithography with a clear field mask. The waveguides are then etched to a depth of 1.8 μm via inductively coupled plasma (ICP) etching with gas mixtures of BCl_3 and Cl_2. For this process, the BCl_3 and Cl_2 flow rates are controlled to be 12.5 and 2.5 sccm, respectively, with a chamber pressure of 1 mTorr at a substrate temperature of 25 $^\circ$C. Two RF sources (70 mW and 500 mW) are used to generate a high-density plasma and

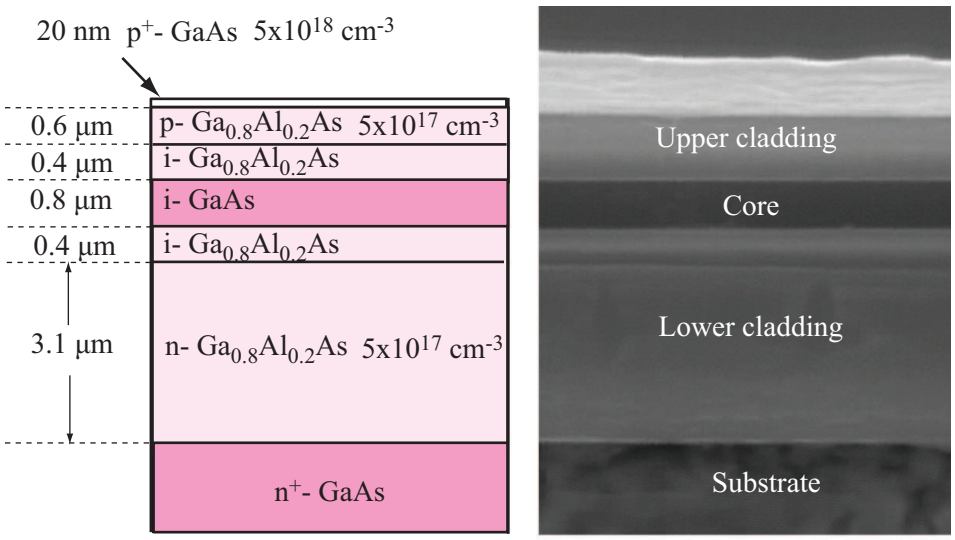

Figure 3.1: Schematic cross-section and scanning electron micrograph of material structure for a GaAs/AlGaAs optical waveguide.

to introduce a self-biased electrical field, respectively. With two RF power sources, the ICP system has the flexibility to control ion density and ion energy independently, unlike a conventional reactive ion etching system. These etching parameters are optimized to create a vertical etch profile with the smooth sidewalls required for a low-loss waveguide. For these parameters, the ICP etch rate was estimated to be 300-350 nm/min with a GaAs:photoresist selectivity of 3:1. Figure 3.2 depicts a cross-sectional schematic illustration and a scanning electron micrograph of a GaAs/AlGaAs waveguide. The calculated TE mode contours were superposed on the cross-section in Fig. 3.2(a) with the effective area A_{eff} estimated to be 1.8 μm^2, based on the calculated mode.

During the ICP etching process, a thin layer of photoresist byproducts containing Cl-C-H polymers is deposited on the top and sidewalls of the waveguides. These residual polymers are difficult to remove with standard solvent cleaning using acetone, methanol

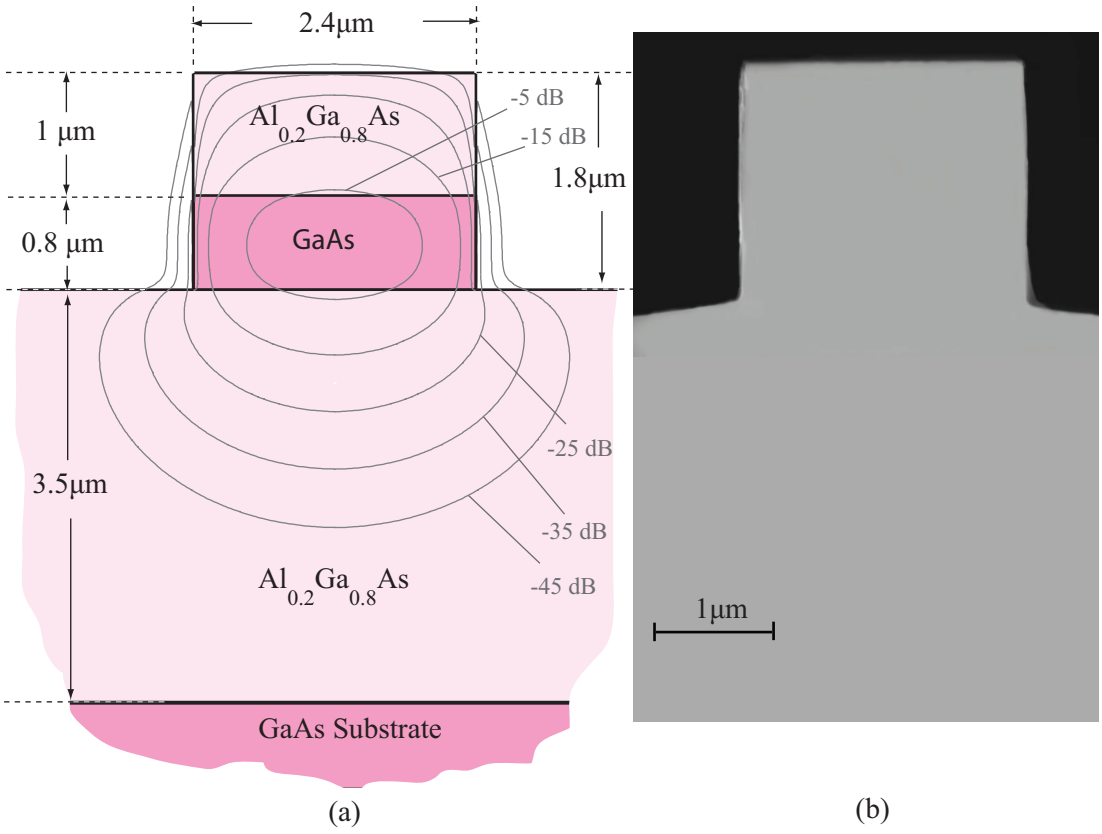

Figure 3.2: Cross-section of a GaAs/AlGaAs waveguide. (a) Schematic illustration with calculated fundamental TE mode profile (contours labelled in dB relative to peak value). (b) Scanning electron micrograph.

and isopropanol. Figure 3.3(a) depicts the scanning electron micrograph of the waveguide cleaned by standard solvent cleaning (i.e. acetone/methanal/isopropanal) after ICP etching. It is clear that there are residual polymers left on the waveguide. A more effective approach to remove these residues was suggested in [72]. The sample is dipped into H_3PO_4 at room temperature for 2 minutes immediately after the ICP etch, followed by O_2 plasma cleaning in a reactive ion etching (RIE) system for 5 minutes and solvent-based (NMP) stripping at 70 °C for 15 minutes. Using this method, this residue is successfully removed as shown in Fig. 3.3(b).

The sample substrate is then thinned down to 120 μm to facilitate accurate cleaving. After that, the sample is scribed using high-power laser scriber setup and is cleaved on the cleave stage on both facets to a length of 4.5 mm. Finally, a silicon nitride anti-reflection (Si_3N_4-AR) coating was deposited on both facets of the waveguide by high density chemical vapor deposition (HDCVD). First, ammonia (NH_3) is deposited for 3 minutes to improve the adhesion between the Si_3N_4 film and GaAs. Then, Si_3N_4 is deposited with gas mixtures of N_2 and SiH_4 with RF power of 500 W under the chamber pressure of 5 mTorr at 300 °C. Both N_2 and SiH_4 flow rates are controlled to be 10 sccm. Under this condition, the deposition rate for the horizontal surface was measured to be approximately 34-37 nm/min. The Si_3N_4 film has a refractive index n of 2 at the wavelength λ of 1550 nm. For a single layer AR coating, a quarter-wavelength-thick Si_3N_4 film is deposited at both facets of the waveguide. A quarter-wavelength thick film is chosen in order to minimize the normal incidence reflection. For applications operating at the wavelength of 1550 nm, the target Si_3N_4 thickness is calculated to be $\lambda/4n$ = 194 nm. The deposition time is calculated by taking into account that the deposition rate on verti-

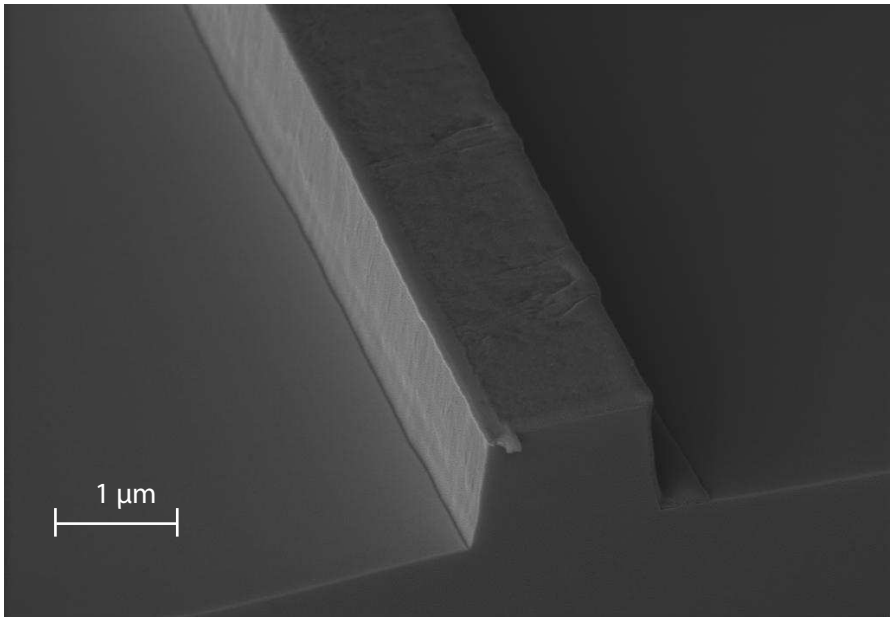

(a)

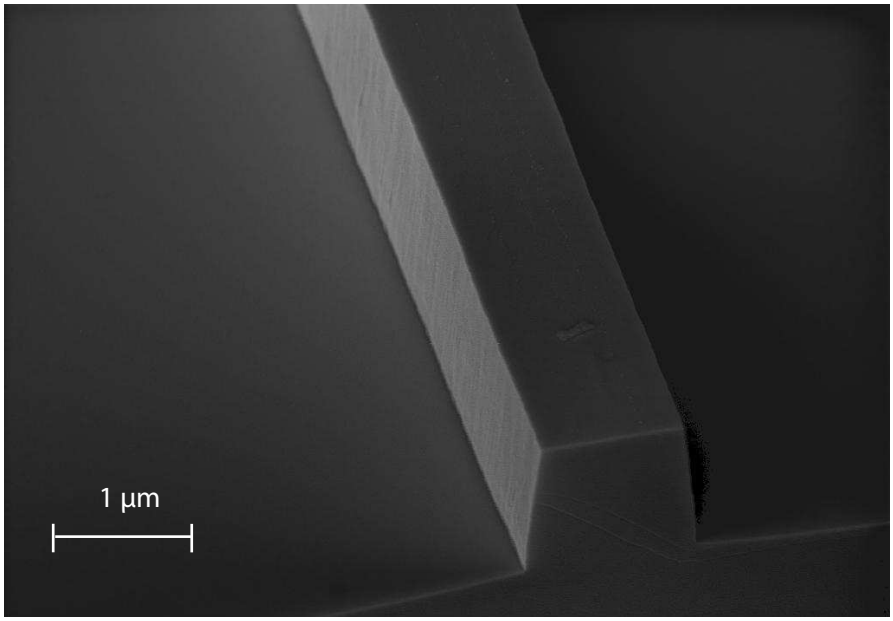

(b)

Figure 3.3: Scanning electron micrographs of the waveguide after ICP etching. (a) with standard solvent cleaning. (b) with H_3PO_4, following by O_2 plasma cleaning and NMP stripping.

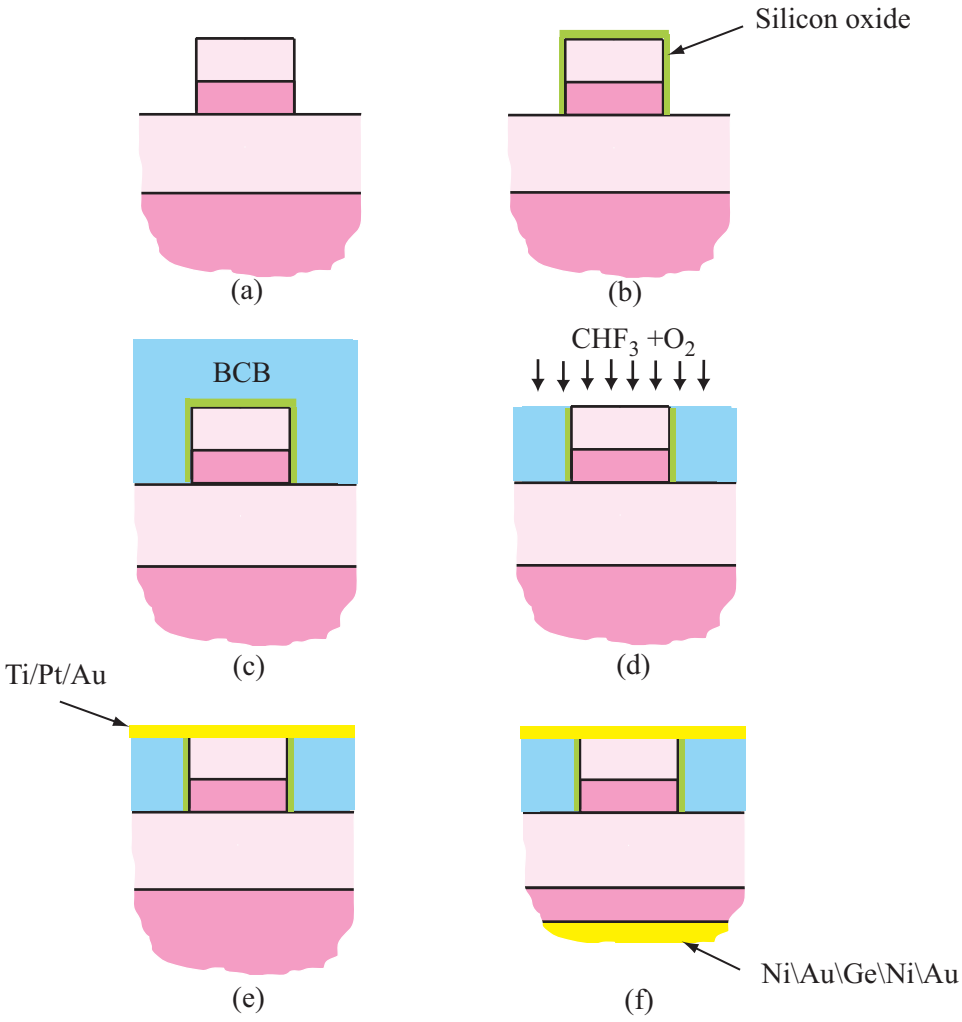

Figure 3.4: Overview of the process for fabricating GaAs waveguide-based photodetectors

cal surfaces, like the waveguide facets, is approximately 50% slower than on horizontal surfaces. After AR-coating, the sample is mounted to the submount and is ready to be tested.

3.2 Fabrication of GaAs Waveguide-Based Photodetectors

The fabrication process for waveguide photodetectors is similar, but contains additional steps for planarization and deposition of Ohmic contacts. Figure 3.4 illustrates the fabrication process of GaAs waveguide-based photodetectors. We fabricate GaAs waveguide-based photodetectors based on the same epistructure as depicted in Fig. 3.1. After the waveguide is patterned by ICP etching, the samples are then coated with a uniform layer of 30 nm of silicon oxide using plasma enhanced chemical vapor deposition (PECVD). The propose of this layer is to enhance adhesion for the subsequent benzocyclobutene (BCB) planarizing layer. BCB is a low-index and low-loss dielectric material that is widely used for planarization. The adhesion promoter (AP3000) and BCB (Cyclotene 3022-57 from Dow chemical) are spun on the oxidized sample and cured. The initial BCB film thickness is estimated to be 5.6 μm, measured from base of waveguides. BCB is then etched back by reactive ion etching (RIE) with a gas mixtures of CHF_3 and O_2 with flow rates of 5 and 20 sccm, respectively. The chamber pressure is set at 300 mTorr with a power of 175 W. The silicon oxide on the top of the waveguides is also etched back by RIE with gas mixture of CHF_3 and O_2 to expose the p-doped region on top of the waveguides. For silicon oxide etch, CHF_3 and O_2 flow rates are controlled to be 18 and 2 sccm, respectively, with a chamber pressure of 40 mTorr and a power of 175 W. After the BCB is planarized, a negative photoresist (NR7-1500PY) is spun on the sample and exposed in order to prepare for the liftoff of the p-type top contact. Ti (100Å)/Pt (300Å)/Au (4000Å) is deposited by an e-beam evaporator and lifted off to simultaneously form the top contact. The sample is then thinned down to 120 μm in order to deposit the

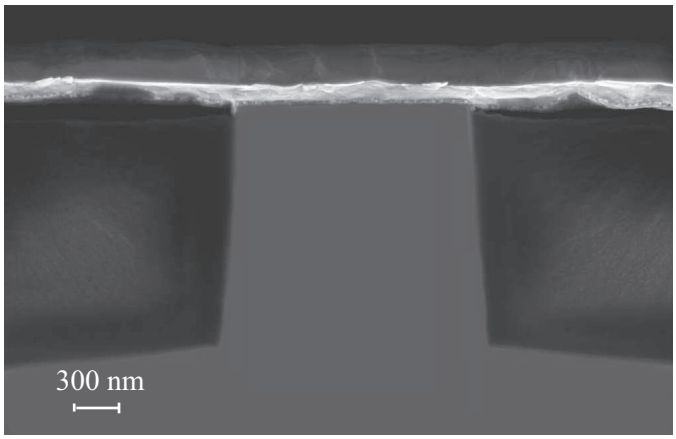

Figure 3.5: Scanning electron micrograph of a cross-section of a GaAs waveguide-based photodetector.

back contact and prepare for cleaving. After that, Ni (50Å)/Au (800Å)/Ge (400Å)/Ni (300Å)/Au (2000Å) is deposited at the back of the sample to form n-type contact. The sample is then put in the rapid thermal annealing (RTA) at 300°C for 1 minute and at 400°C for 40 seconds to simultaneously anneal both metal contacts. Finally, the sample is scribed using a high-power laser scriber setup and is cleaved on both facets. A scanning electron micrograph of a cross-section of GaAs waveguide after metal deposition is shown in Fig. 3.5.

3.3 Waveguide Measurements

3.3.1 Propagation Loss Measurement

As mentioned in chapter 2, propagation loss in the waveguide can be measured using the Fabry-Pérot technique [44]. The technique relies on cleaved waveguide facets to form a Fabry-Pérot cavity. The transmitted power is measured while the input wavelength

is scanned. Because of the Fresnel reflectivity between Air and GaAs at the cleaved facets, the transmission spectrum shows a periodic sequence of peaks associated with the longitudinal modes of the Fabry-Pérot cavity. From the maximum and minimum transmitted power, P_{max} and P_{min}, the contrast (K) is defined as

$$K = \frac{P_{\max} - P_{\min}}{P_{\max} + P_{\min}}, \tag{3.3}$$

Which is related to the propagation loss α by :

$$\ln[1 - (1 - K^2)^{\frac{1}{2}}/K] = \ln R - \alpha L, \tag{3.4}$$

where L is the waveguide length and R is the endfacet reflectivity. If we assume that R is approximately 30% (based on Fresnel reflectivity between air and GaAs), α can be determined by measuring the contrast K in the waveguide. The solid line in Fig. 3.6 represents the transmission power fringes of a representative 5.4-mm long passive waveguide prior to AR coating. TE-polarized light was launched into these waveguides. From Eq.(3.4), the TE propagation loss of these waveguides was estimated to be 4-6 dB/cm. TM loss is typically higher than TE loss in these waveguides and was measured to be 8-9 dB/cm.

The dashed line in Fig. 3.6 represents the transmission of TE-polarized light in the same waveguide after AR coating was deposited. No transmission power fringe was observed, which means that almost zero reflectivity at the facet is achieved after AR coating. Low facet reflectivity is also evident in the decrease in the total insertion loss of the waveguide.

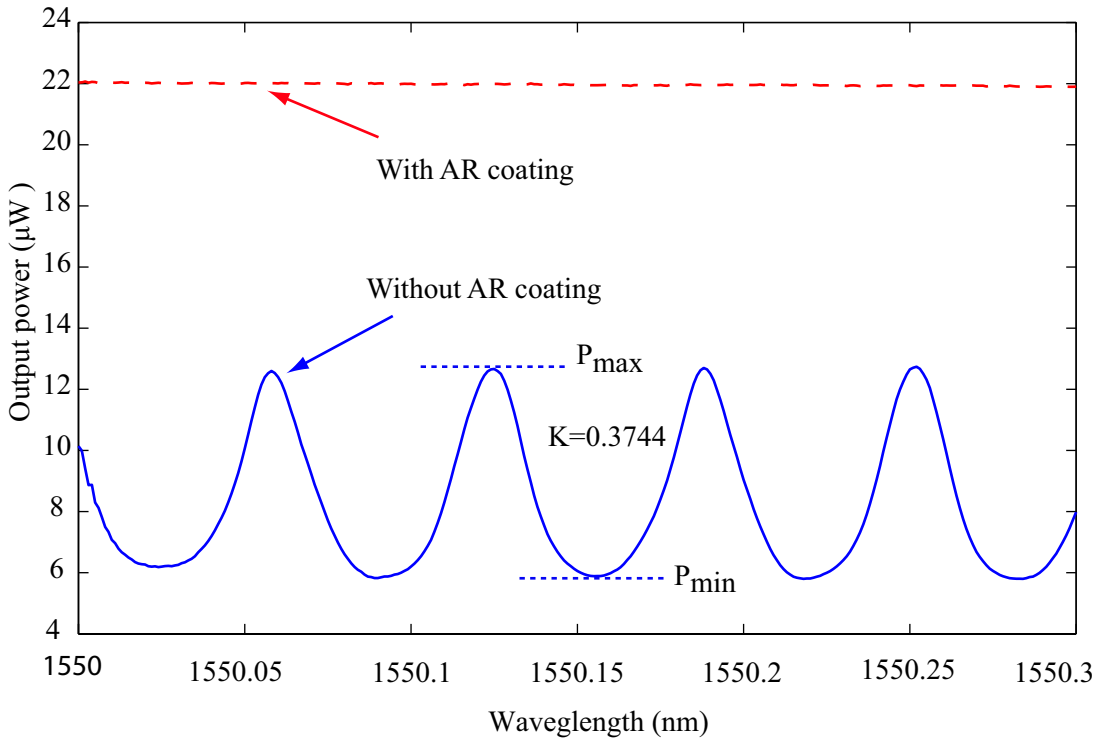

Figure 3.6: Transmission power fringes of TE-polarized light in a 5.4-mm long waveguide. Solid line : without AR coating, Dashed line : with AR coating

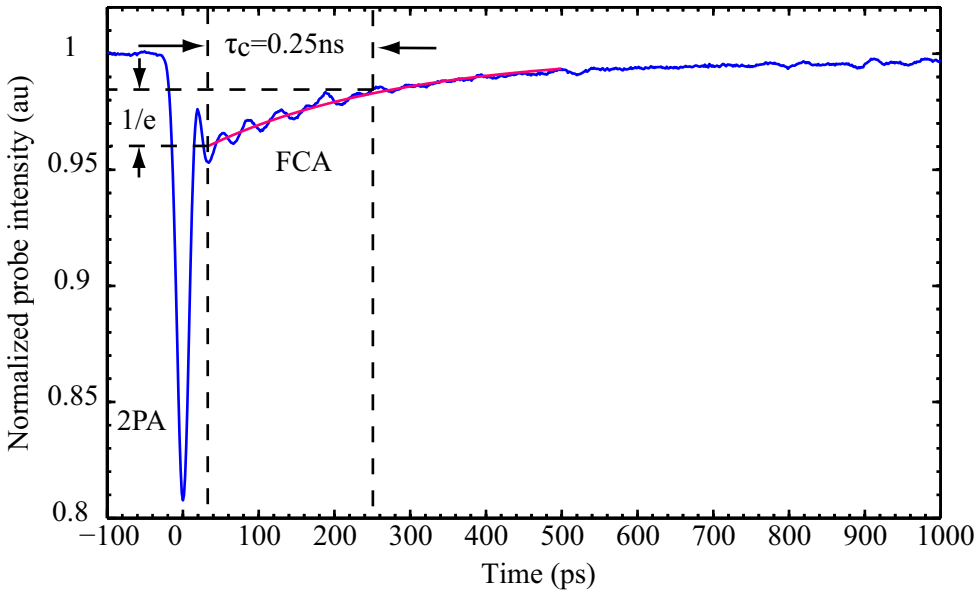

Figure 3.7: The measured free-carrier lifetime recovery trace in a GaAs waveguide. The red line corresponds to the estimated exponential recovery.

3.3.2 Free-Carrier Lifetime Measurement

The measurement of the carrier lifetime in a GaAs waveguide is similar to that described earlier for a porous silicon waveguide described in chapter 2. I.e, we launch a strong pump pulse into the waveguide and measure the transient absorption of a a weaker, co-propagating CW probe signal. Figure 3.7 plots the transmitted probe signal from the GaAs waveguide. We obtain an estimate of the free-carrier lifetime by measuring the $1/e$ recovery time, ignoring the initial, instantaneous two-photon absorption. The GaAs waveguide exhibits a carrier lifetime of approximately 250 ps.

3.3.3 Measurement of Two-Photon Absorption Coefficient

There have been several reports on the measurement of the 2PA coefficient β_{2PA} in semiconductors including Si [17, 32, 50, 73, 74], GaAs [17, 18] and InP [75] in the 1550 nm wavelength regime. These measurements have been performed using several techniques including inverse transmission [18, 50, 73, 74], z-scan [17] and by modeling transmission change as we described in chapter 2 and in [32]. Among these measurement techniques, the inverse transmission technique has been most frequently employed for the measurement of the 2PA coefficient in semiconductor waveguides. At low input powers, for which the free-carrier absorption (FCA) can be neglected, β_{2PA} can be obtained by measuring the reciprocal of the nonlinear transmission $1/T$ as a function of coupled peak input power P_{in} [76]. The reciprocal of the nonlinear transmission through a waveguide of length L with an effective area A_{eff} and a linear propagation loss α can be described by

$$\frac{1}{T} = \frac{P_{in}}{P_{out}} \simeq e^{\alpha L}\left[1 + \frac{\beta_{2PA}}{\Gamma A_{eff}} L_{eff} P_{in}\right], \tag{3.5}$$

where L_{eff} is defined as $(1 - e^{-\alpha L})/\alpha$. Γ is a dimensionless 2PA correction factor, which depends on the temporal profile and optical power of the input pulse. The 2PA correction factor is described in detail in Appendix A of this thesis. β_{2PA} can be obtained from the slope of the reciprocal of the transmission. Figure 3.8 shows a measurement of the inverse transmission in a GaAs waveguide. We used an optical parametric oscillator (OPO) pumped by Ti:sapphire laser to produce input pulses at 1550 nm with a repetition rate of 82 MHz. The input pulsewidth broadened to 2.2 ps at the front facet of the waveguide as a result of chromatic dispersion in the fiber. Using the value of α from Fabry-Pérot mea-

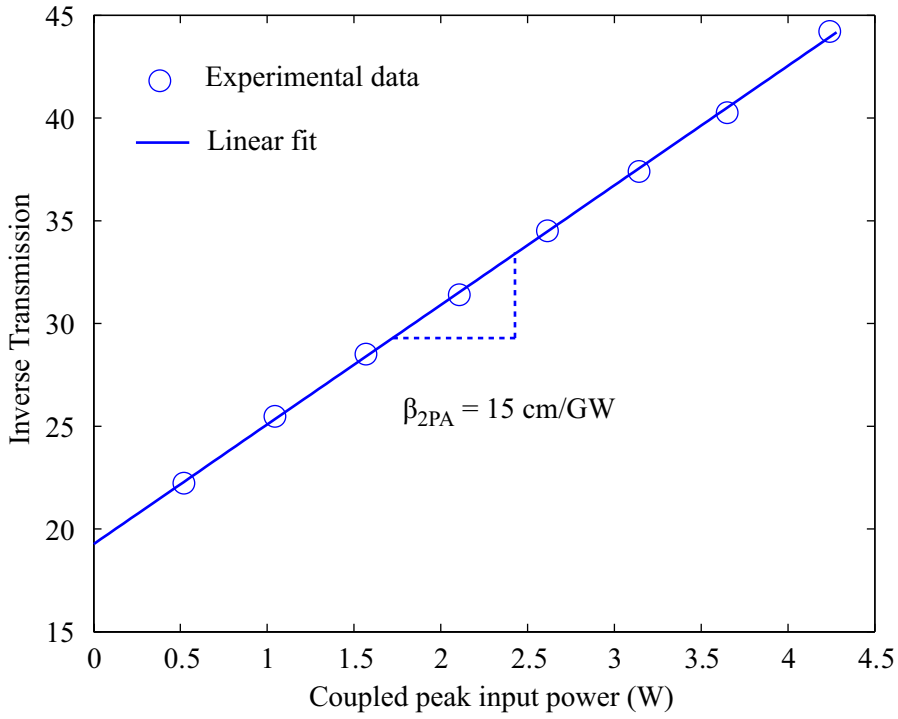

Figure 3.8: The reciprocal of the nonlinear transmission of a 5-mm long GaAs waveguide as a function of coupled peak input power.

surement and Γ described in Appendix A, β_{2PA} was estimated to be 15 cm/GW, which is comparable to prior measurements conducted on GaAs waveguides using the inverse transmission technique [18] and in bulk GaAs using the z-scan technique [17].

3.3.4 Measurement of Two-Photon Absorption Photocurrent

Another way to observe two-photon absorption is to measure the photocurrent generated when the waveguide is illuminated below the bandgap. Figure 3.9 shows the measured nonlinear photocurrent of a waveguide detector as a function of input intensity for both TE and TM modes. GaAs has a bandgap that allows linear absorption at wavelengths shorter than 870 nm and degenerate 2PA at wavelengths shorter than 1740 nm. Here, 1550-nm optical pulses generated from the OPO are coupled into the waveguide using a lensed fiber. At low input intensity, the photocurrent is proportional to the input intensity, as seen from the slope of 1 on log-log scale in Fig. 3.9. In this region, linear absorption dominates. As the input power increases, two-photon absorption becomes a dominant effect. The photocurrent in this region is proportional to the square of the input intensity, as seen from the slope of 2 on log-log scale indicated in Fig. 3.9.

3.3.5 Autocorrelation Measurement

Autocorrelation is one method to check whether the nonlinear photocurrent from the waveguide is generated by ultrafast two-photon absorption, rather than by some slower nonlinear effects such as free-carrier absorption or thermal effects. The fabricated p-i-n waveguide is used as a detector for the autocorrelation measurement. The experimental

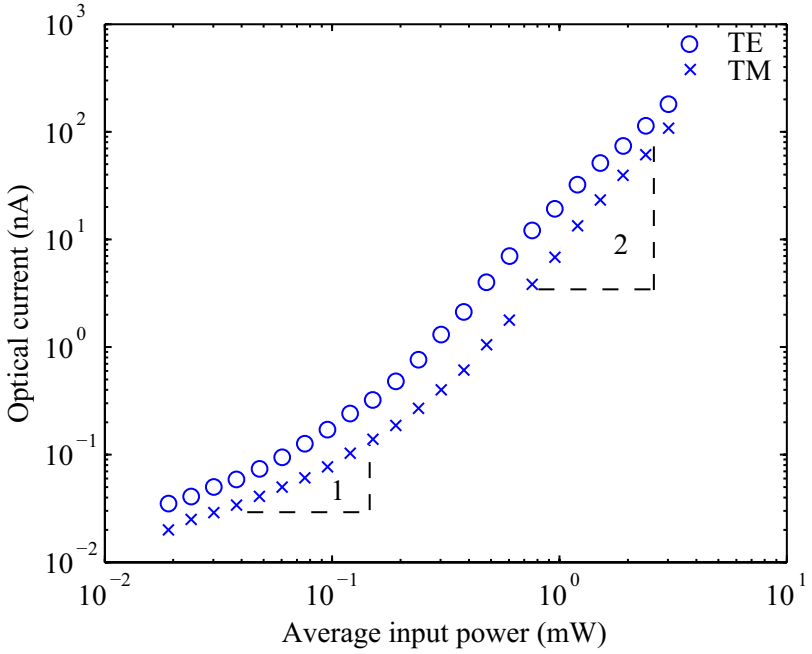

Figure 3.9: Nonlinear response of a p-i-n waveguide detector to incident pulses at 1550 nm.

setup is shown in Fig. 3.10.

The OPO was again used as the pulse source for this measurement. The first fiber polarization controller was adjusted so that both beams coming out of a polarizing beam-splitter have the same power. The two orthogonally polarized pulses were then recombined after one was delayed with a variable delay line. The second polarization controller was used to adjust the polarization of both beams to be at 45 degrees with respected to the axis of an in-line polarizer. After the polarizer, both beams were co-polarized. Finally, a lensed fiber was used to couple the beam into the p-i-n waveguide detector, where the photocurrent was measured in real time with a sampling oscilloscope as the delay was scanned.

Figure 3.11 shows the autocorrelation result from a p-i-n waveguide. The interfer-

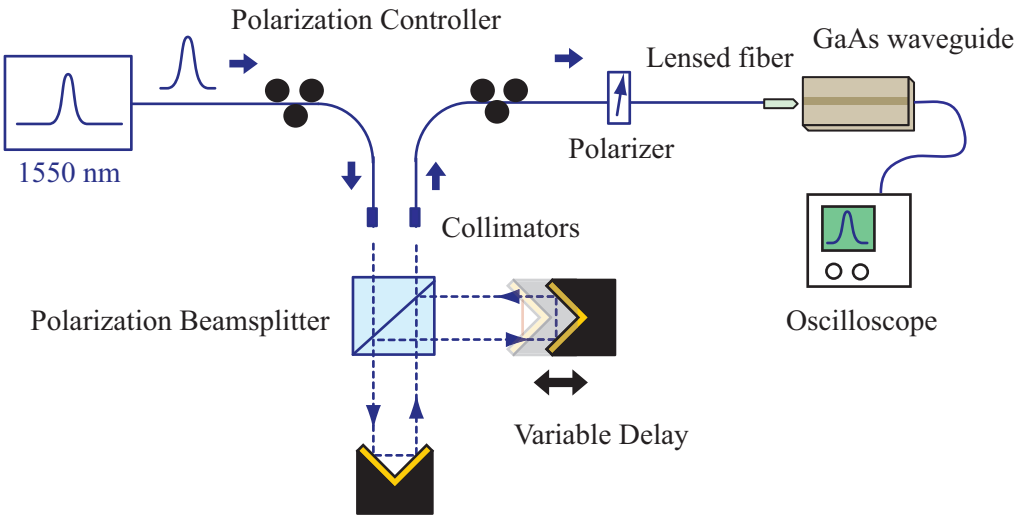

Figure 3.10: The experimental setup for autocorrelation measurement using a p-i-n waveguide detector.

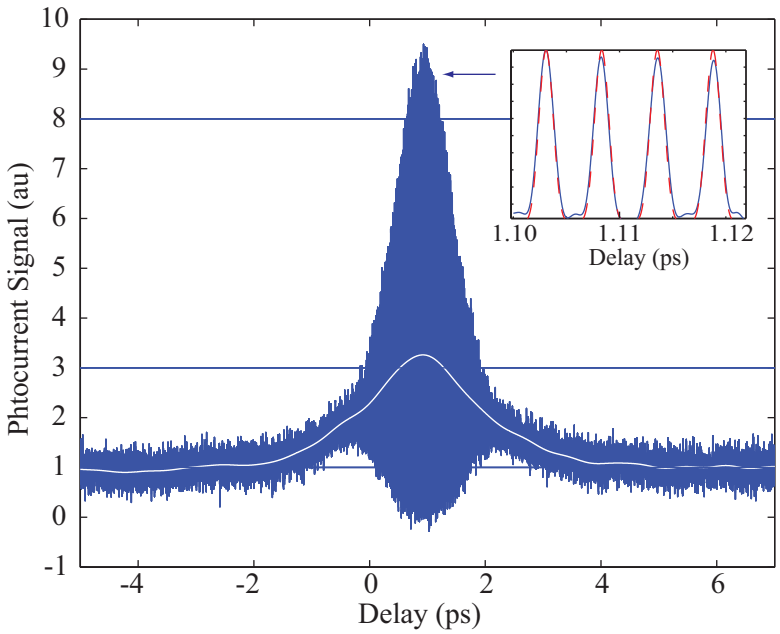

Figure 3.11: Measured interferometric autocorrelation.

ence fringes of the autocorrelation depicted in the inset show the expected $\cos^4$ fringe shape. The white curve is obtained by numerically low-pass filtering the interference fringe. The FWHM of the autocorelation is 3.36 ps, which corresponds to a pulse width of 2.18 ps assuming a hyperbolic secant squared (sech^2) pulse shape. The measured pulse width is in close agreement with independent measurements performed with second harmonic generation (SHG) based autocorrelation. The ratio of the correlation peak to background of the fringe result is a little bit higher than the 8:1 expected theoretically. The peak-to-background ratio of the average fringe result is also a little bit higher than the 3:1 expected. This could be attributed to nonlinear effects in the optical fiber from the laser source to the waveguide. Based on the observed autocorrelation fringes, we can infer that nonlinear photocurrent is generated by fast nonlinear process such as 2PA, and not from any slow nonlinear effects like free-carrier absorption or thermal effect.

3.4 Summary

We described the fabrication process of GaAs waveguides with and without electrical contacts. The characteristics of the waveguides are also tested. The mode parameters and properties of a GaAs ridge waveguide measured in this chapter are summarized in Table 3.2. For TE-polarized light, the fabricated 2.4-μm wide waveguides have a linear propagation loss of 4-6 dB/cm. The free-carrier lifetime in these waveguides estimated by measuring the 1/e recovery time is found to be 250 ps. The two-photon absorption coefficient is measured using the inverse transmission technique and is estimated to be 15 cm/GW. The intensity-dependence of the photocurrent generated from a GaAs waveguide

parameter	GaAs ridge waveguide	(unit)
Effective area A_{eff}	1.8	(μm^2)
Waveguide length L	4.6	(mm)
Linear loss α	$4-6$	(dB/cm)
2PA coefficient β_{2PA}	15	(dB/cm)
Free-carrier lifetime τ_c	250	(ps)
Effective length $L_{\text{eff}} \equiv (1-e^{-\alpha L})/\alpha$	3.3	(mm)
Total insertion loss	8.5	(dB)

Table 3.2: Mode parameters and optical properties of a GaAs/AlGaAs ridge waveguide.

detector is characterized. We can infer from the measurements that nonlinear photocurrent in this device is generated by two-photon absorption at 1550 nm.

Chapter 4

Wavelength Conversion in a Gallium Arsenide Waveguide

Wavelength conversion is essential for all-optical dense wavelength division multiplexing (DWDM) networks. A wavelength converter is used to convert an encoded signal from one wavelength to another. It provides the flexibility for optical interconnection by wavelength rerouting and increases the capability of the network by re-using the available wavelengths [77]. The conventional way of performing wavelength conversion is to electrically detect, and then re-modulate and transmit a second laser. Here, we are trying to achieve all-optical wavelength conversion, which uses nonlinear optics to convert from one wavelength to another without relying on electrical detection. This could be especially attractive because it allows conversion of high-speed signals that cannot be detected electrically.

In chapter 2, we showed that when a single optical signal propagates inside a nonlinear waveguide, its transmitted power and spectrum change due to the instantaneous and carrier-based nonlinear effects. As the input power is increased, the ratio of transmitted to input power decreases as a result of two-photon absorption and free-carrier absorption. Similarly, at higher input power, the output spectrum broadens and shifts as a result of self-phase modulation and free-carrier dispersion. When two or more optical signals with different carrier frequencies simultaneously propagate inside a nonlinear waveguide, they can interact with each other due to third-order nonlinearities. The amplitude of one

optical signal can be altered by the intensities of all other optical signals. This effect is called cross-amplitude modulation (XAM). Similarly, the phase of one optical signal can be altered by the intensities of all other optical signals via cross-phase modulation (XPM). Moreover, a new optical waveform with a different carrier frequency could be generated through nonlinear interactions such as four-wave mixing (FWM).

GaAs/AlGaAs waveguides provide interesting optical properties for nonlinear optical signal processing. Although there have been several demonstrations of all optical signal processing based on third-order nonlinearities in GaAs/AlGaAs waveguide devices [12, 13, 19, 20, 66], there have been no reports on data performance metrics such as eye-diagrams or bit-error rate (BER) receiver sensitivity for these devices.

In this chapter, we demonstrate all-optical wavelength conversion based on nonlinear effects in the GaAs/AlgaAs waveguides described in chapter 3, the properties of which are listed in Table 3.2. We measure, for the first time, eye-diagrams and bit-error rate receiver sensitivity in these systems. First, XAM-based wavelength conversion is detailed. We next describe a wavelength conversion system that uses XPM. In the last section, we describe the principle of FWM and how we exploit this effect for wavelength conversion in these waveguides.

4.1 Wavelength Conversion Using Cross-Amplitude Modulation

When a strong pump signal and a weak probe signal propagate along a waveguide, the amplitude of probe signal can be affected by the intensity of a pump signal due to non-degenerate two-photon absorption, i.e., simultaneous absorption of one pump photon and

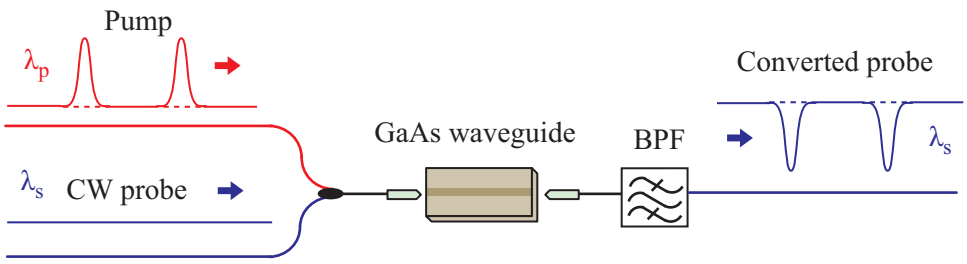

Figure 4.1: Wavelength conversion using cross-amplitude modulation in a GaAs waveguide. (BPF : bandpass filter)

one probe photon. This ultrafast effect can be employed for cross-amplitude modulation (XAM) in high-speed all optical switches and for wavelength conversion in semiconductor waveguides [78, 79]. Figure 4.1 depicts a simple diagram of XAM-based wavelength conversion. The XAM-based wavelength converter requires only a GaAs waveguide and a filter to isolate the probe signal. In the setup shown here, the two input signals are the pump pulses and the CW probe. The dip in the transmission of the probe signal is caused by pump-induced 2PA, which only occurs when the pump pulse is on.

The pump and probe signal are attenuated due to the linear loss as they co-propagate in the waveguide. The strong pump signal is also decreased as a result of degenerate 2PA from the pump signal, while the weaker probe signal is decreased by the non-degenerate 2PA induced by the pump pulses. Moreover, free-carriers generated from 2PA of the pump pulses could further deplete both signals due to free-carrier absorption as previously demonstrated in the free-carrier lifetime measurement shown in Fig. 3.7. Unlike free-carrier lifetime measurement where we purposely used strong pump pulses with very high peak power ($P_{peak} \sim 800$ W) to generate free-carrier through 2PA, we used pump pulses with a relatively low peak power ($P_{peak} \sim 3$ W) in the XAM measurement. As we will

show latter in this section, free-carrier effects can be neglected for the input powers used in the experiments as evidenced by the absence of a slow recovery in the transmission of the probe signal.

Not only we neglect free-carrier effects, but also we neglect the dispersion and pulse walk-off in the waveguide as well as the dispersion-based pulse broadening effects. We also assume that the probe is weak and the probe-induced 2PA can be neglected. Under these assumptions, the two coupled equations describing the powers of two input signals propagating along the waveguide can be modeled by:

$$\frac{\partial}{\partial z}P_1(z,t) = -\alpha P_1(z,t) - \frac{\beta_{2\mathrm{PA}_{11}}}{A_{\mathrm{eff}}}P_1^2(z,t) \tag{4.1}$$

and

$$\frac{\partial}{\partial z}P_2(z,t) = -\alpha P_2(z,t) - \frac{2\beta_{2\mathrm{PA}_{21}}}{A_{\mathrm{eff}}}P_1(z,t)P_2(z,t) \ , \tag{4.2}$$

where $P_1(z,t)$ and $P_2(z,t)$ are the powers of pump and probe signals at distance z and time t, respectively, α is the linear propagation loss, A_{eff} is the effective area of the waveguide, $\beta_{2\mathrm{PA}_{11}}$ is the degenerate 2PA coefficient of the pump signal, and $\beta_{2\mathrm{PA}_{21}}$ is the non-degenerate 2PA coefficient between pump and probe signals. Equation (4.1) can be directly integrated to obtain a solution for $P_1(z,t)$:

$$P_1(z,t) = \frac{P_1(0,t)\exp(-\alpha z)}{1+\frac{\beta_{2\mathrm{PA}_{11}}}{A_{\mathrm{eff}}}\left[\frac{1-\exp(-\alpha z)}{\alpha}\right]P_1(0,t)} \ . \tag{4.3}$$

If the wavelengths of pump and probe signals are close to each other, $\beta_{2\mathrm{PA}_{11}}$ and $\beta_{2\mathrm{PA}_{21}}$ are assumed to be equal by setting $\beta_{2\mathrm{PA}_{11}} = \beta_{2\mathrm{PA}_{21}} = \beta_{2\mathrm{PA}}$ in Eqs. (4.2) and (4.3). Substituting

$P_1(z,t)$ derived in Eq. (4.3) into Eq. (4.2), the probe power at the output of the waveguide with length l can be described as

$$P_2(l,t) = \frac{P_2(0,t)\exp(-\alpha l)}{\left[1+\frac{\beta_{2PA}}{A_{eff}}P_1(0,t)L_{eff}\right]^2} \quad , \tag{4.4}$$

where the effective length L_{eff} is defined as $[1-\exp(-\alpha l)]/\alpha$. For a pump pulse with peak power of P_{1o} at $t=0$, the modulation depth (M) can be defined as

$$M = 1 - \frac{T_{min}}{T_{max}} = \frac{P_2(l,0)|_{P_1=0} - P_2(l,0)|_{P_1=P_{1o}}}{P_2(l,0)|_{P_1=0}} \quad , \tag{4.5}$$

where T_{max} and T_{min} are the maximum and minimum ratio of transmitted to input power of the probe, respectively. $P_2(l,0)|_{P_1=P_{1o}}$ and $P_2(l,0)|_{P_1=0}$ are the transmitted probe in the presence and in the absence of the pump pulse, respectively. According to Eq.(4.4) and Eq.(4.5), the modulation depth of the CW probe at the output of the waveguide can be derived as

$$M = 1 - \frac{1}{\left[1+\frac{\beta_{2PA}}{A_{eff}}P_{1o}L_{eff}\right]^2} \quad . \tag{4.6}$$

The experimental setup for wavelength conversion based on XAM in GaAs waveguides is shown in Fig. 4.2. In this experiment, the 10-Gb/s return-to-zero on-off keying (RZ-OOK) pump signal centered at 1553.5 nm was generated by modulating the 3-ps pulse train from a mode-locked laser diode with a $(2^{31}-1)$ pseudorandom data pattern. The 10-Gb/s pump signal and the 1540-nm CW probe were amplified and coupled into the waveguide using a 50% coupler. The insertion loss was measured to be 8.5 dB, in-

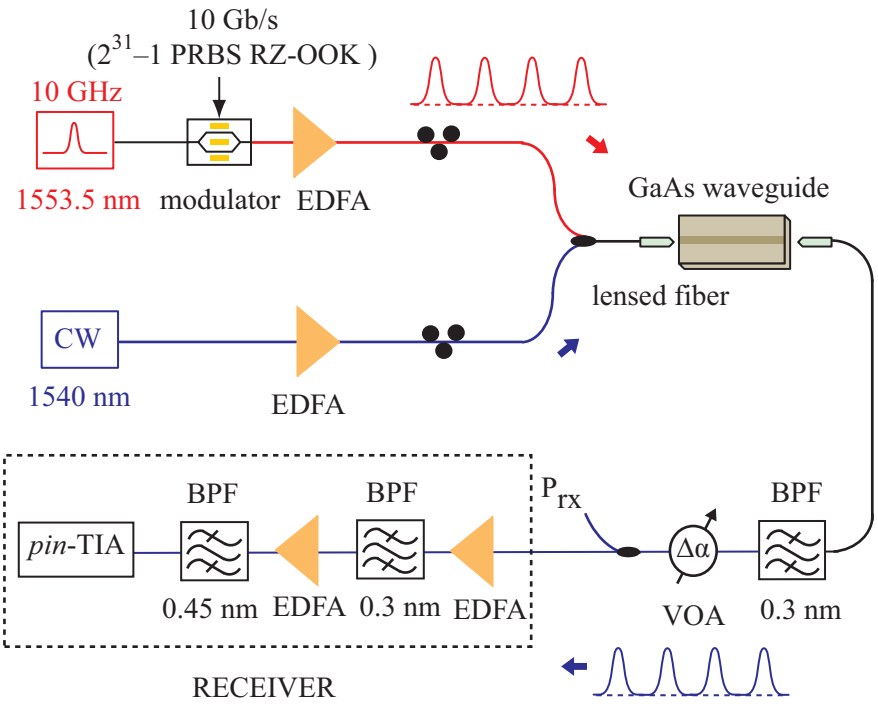

Figure 4.2: Experimental setup for 10 Gb/s XAM-based wavelength conversion. (P_{RX} : receiver power; VOA : variable optical attenuator; BPF : bandpass filter; EDFA : erbium-doped fiber amplifier; *pin*-TIA : p-i-n photodiode and transimpedance amplifier.)

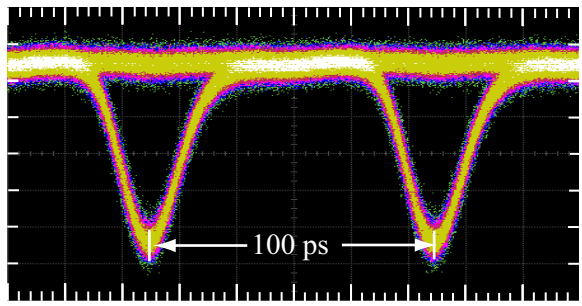

20 ps /div

(a)

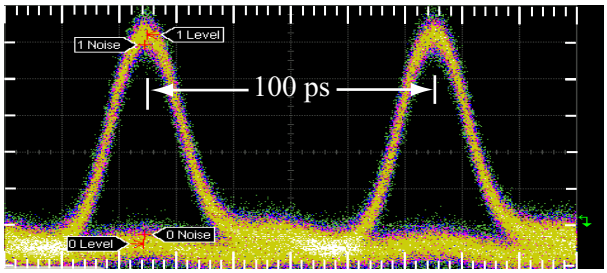

20 ps /div

(b)

Figure 4.3: Infinite-persistence 10 Gb/s sampling oscilloscope traces of converted RZ-OOK signal at the probe wavelength. (a) Optical signal before p-i-n photodetector. (b) Electrical signal generated from p-i-n photodiode after amplified by an inverting transimpedance amplifier.

cluding a linear propagation loss of 6 dB/cm and an estimated coupling loss of 3 dB per facet. The respective average coupled input powers of the pump and probe signals were 16 dBm and 14 dBm. Although the average powers are similar, the peak power of the pump is much larger than that of the CW probe. The signal emerging from the waveguide was processed with bandpass filters tuned to the probe carrier wavelength to spectrally isolate the probe. The modulated probe was then sent to a standard pre-amplified optical receiver where the bit error rate was measured as a function of the input probe power entering the preamplifier.

Figure 4.3(a) shows the eye-diagram of the probe signal before the p-i-n photodetector at a receiver power of -9 dBm. The dip in transmission of the converted probe induced by 2PA from the strong pump pulse only occurred when the pump pulse was on. Because two-photon absorption is an ultrafast nonlinear process, we believe that the impulse-like dip matches the shape of the input pulses. However, the impulse-like dip cannot be observed in Fig. 4.3(a) because the photoreceiver is not fast enough to resolve it. The detector used in this experiment has a 40-ps response time, which is not fast enough to measure the duration of the dip or the true optical modulation depth. As previously shown in Fig. 3.7, the free-carrier lifetime in these waveguides was measured to be 250 ps. If free-carrier is present, the detector used in this measurement should be fast enough to see a slow recovery trace due to free-carrier absorption. Since we do not see the slow recovery trace, we could assume that free-carrier effects can be neglected in this measurement. The calculated modulation depth was theoretically estimated to be 80% for the 16 dBm RZ-OOK pump signal. Fig. 4.3(b) shows the eye-diagram of the electrical signal generated from the p-i-n photodiode after amplification by an inverting transimpedance amplifier. The eye-diagram is clearly open.

Figure 4.4 depicts the receiver sensitivity measurement of 10-Gb/s, XAM-based wavelength conversion. The baseline receiver sensitivity was measured by bypassing the GaAs waveguide and the 0.3-nm filter before the receiver and tuning the remaining filters in the receiver to the pump wavelength. The converted RZ-OOK probe signal demonstrated a 10^{-9} BER receiver sensitivity penalty of 27 dB relative to the baseline RZ-OOK pump signal. The reason this sampling system has a large penalty is because the majority of the power of the converted signal is allocated to the constant background

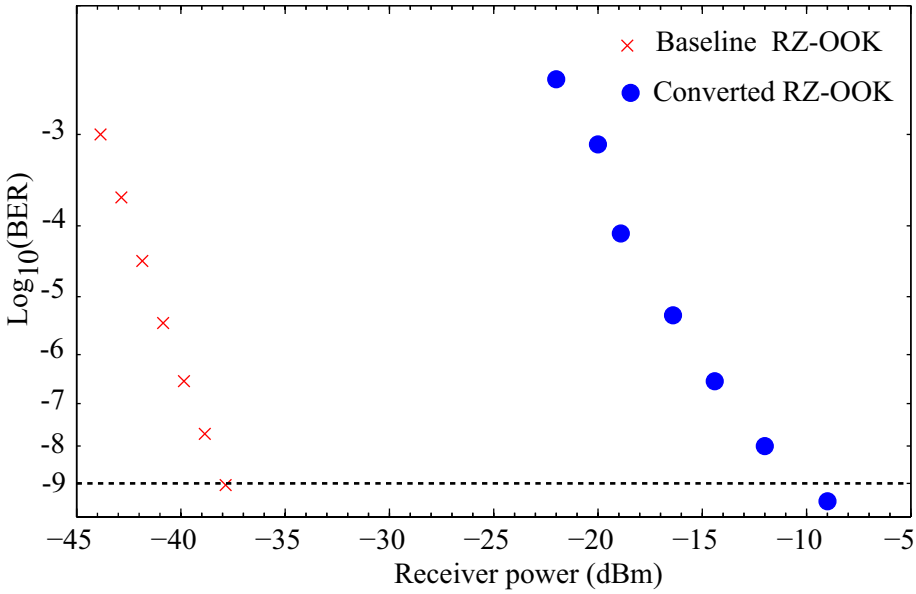

Figure 4.4: Bit-error rate versus received power for 10 Gb/s XAM-based wavelength conversion.

in the zero rail. The cross-amplitude-modulated signal is mostly continuous wave with brief dips in transmission. The XAM data signals can be separated into two components: $P(t) = P_o - P_{mod}(t)$, where P_o is the the power in the DC carrier and $P_{mod}(t)$ is the power in the dips induced by 2PA from the pump pulses. To estimate the ratio of the power in the DC carrier P_o to the average power in the dips $\langle P_{mod}(t) \rangle$, we assume that the impulse-like dips match the shape of the input pulses and the modulation depth is 80%, as theoretically estimated. Under these assumptions, P_o is approximately 19 dB larger than $\langle P_{mod}(t) \rangle$ in this measurement. The sensitivity of the sampling system can be improved by using a Mach-Zehnder interferometer to eliminate the DC carrier from the converted signal.

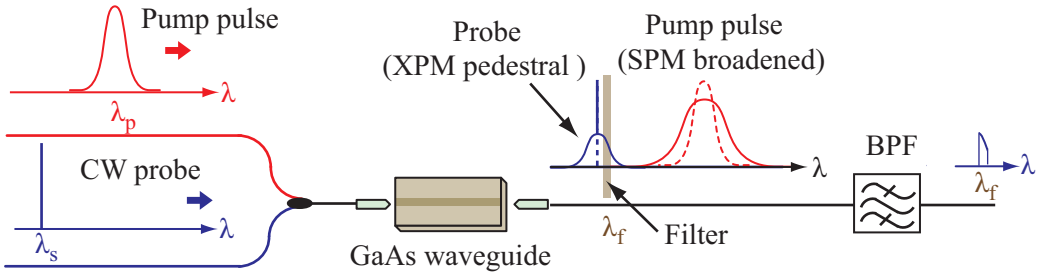

Figure 4.5: Wavelength conversion using cross-phase modulation in a GaAs waveguide.

4.2 Wavelength Conversion Using Cross-Phase Modulation

When a strong pump pulse and a co-propagating probe are launched in a waveguide, the strong pump pulse can induce a change in the refractive index of the material due to optical Kerr nonlinearity and free-carrier dispersion. This refractive index change not only causes a phased-shift of the pump pulse itself, but also alters the phase of the co-propagating probe signal. The former process is called self-phase modulation (SPM), while the latter is called cross-phase modulation (XPM). XPM has been used for wavelength conversion in several nonlinear devices including semiconductor optical amplifiers (SOAs) [80], silicon nanowires [81], highly nonlinear fibers (HNLFs) [82] and chalcogenide glass rib waveguides [8]

Although SPM and XPM effects have been studied in GaAs/AlGaAs waveguides [21, 83, 84], there has been no demonstration of all-optical signal processing using XPM in GaAs/AlGaAs waveguides, especially with the measurements of an eye-diagram or BER receiver sensitivity. In this section, we will demonstrate a 10-Gb/s XPM-based wavelength converter in GaAs waveguides. The wavelength conversion system is also evaluated in a receiver sensitivity experiment.

Figure 4.5 illustrates how wavelength conversion can be achieved using the XPM process. In the setup shown here, the two input signals are a pump pulse train and a CW probe. The pump pulses are broadened due to SPM, while the CW probe acquires a spectral pedestal as a result of XPM induced by the pump pulses. Because the pump is composed of a train of optical pulses, the pedestal of the probe exists only during the pump pulses. A filter is then used to spectrally select the XPM pedestal of the broadened probe signal.

In order to analytically solve for the nonlinear phase shift of the two signals propagating along the waveguide, we simplify the nonlinear coupled equations of the pump and probe signals by neglecting free-carrier effects. In the previous section, we showed that free-carrier absorption could be neglected at the input powers used in the experiment. We assume that free-carrier dispersion does not play an important role at these powers and any nonlinear phase shift is mainly attributable to optical Kerr nonlinearity. By neglecting free-carrier effects, the two coupled equations in Eq. (4.1) and in Eq. (4.2) can be used to describe the power of the two signals propagating along the waveguide. The coupled equations for the pump phase ϕ_1 and the probe phase ϕ_2 can be derived as

$$\frac{\partial}{\partial z}\phi_1(z,t) = -\frac{\omega_1 n_2}{cA_{\text{eff}}}P_1(z,t) \tag{4.7}$$

$$\frac{\partial}{\partial z}\phi_2(z,t) = -\frac{2\omega_2 n_2}{cA_{\text{eff}}}P_1(z,t), \tag{4.8}$$

where ω_1 and ω_2 are pump and probe frequencies, respectively, c is the light velocity, and n_2 is the optical Kerr coefficient. Since the pump intensity is much larger than the probe intensity, we neglect the SPM, XPM and 2PA induced by the probe signal in Eq. (4.7)

and Eq. (4.8). Substituting $P_1(z,t)$ derived in Eq. (4.3) into Eq. (4.8), the nonlinear phase shift of the probe signal at the output of the waveguide can be described as

$$\begin{aligned}\Delta\phi_2(t) &= \phi_2(l,t) - \phi_2(0,t) \\ &= -\frac{2\omega_2 n_2}{cA_{\text{eff}}}\frac{A_{\text{eff}}}{\beta_{\text{2PA}}}\ln\left[1+\frac{\beta_{\text{2PA}}}{A_{\text{eff}}}P_1(0,t)L_{\text{eff}}\right] \quad . \end{aligned} \tag{4.9}$$

For pump pulses with a peak power of $P_{1\text{o}}$, the maximum nonlinear phase shift of the CW probe signal can be derived as

$$\Delta\phi_2 = -\frac{2\omega_2 n_2}{cA_{\text{eff}}}\frac{A_{\text{eff}}}{\beta_{\text{2PA}}}\ln\left[1+\frac{\beta_{\text{2PA}}}{A_{\text{eff}}}P_{1\text{o}}L_{\text{eff}}\right] \quad . \tag{4.10}$$

The nonlinear phase shift of the probe signal $\Delta\phi_2$ in Eq. (4.10) is derived by including the effect of 2PA. By neglecting 2PA in Eq. (4.10), the nonlinear phase shift $\Delta\phi_2'$ becomes

$$\Delta\phi_2' = -\frac{2\omega_2 n_2}{cA_{\text{eff}}}P_{1\text{o}}L_{\text{eff}} \quad . \tag{4.11}$$

Figure 4.6 shows the result of a simulation of the nonlinear phase shift as a function of average pump input power with and without 2PA. For this simulation, we used the previously measured parameters of GaAs waveguides as listed in Table 3.2. The input pump used in this simulation is a 10 Gb/s RZ-OOK signal with the pulsewidth of 3 ps. The dashed line in Fig. 4.6 was obtained by neglecting 2PA in the simulation. In this case, the nonlinear phase shift grows in proportional to the pump input power. The solid line in Fig. 4.6 was obtained by including 2PA in the simulation. The nonlinear phase shift

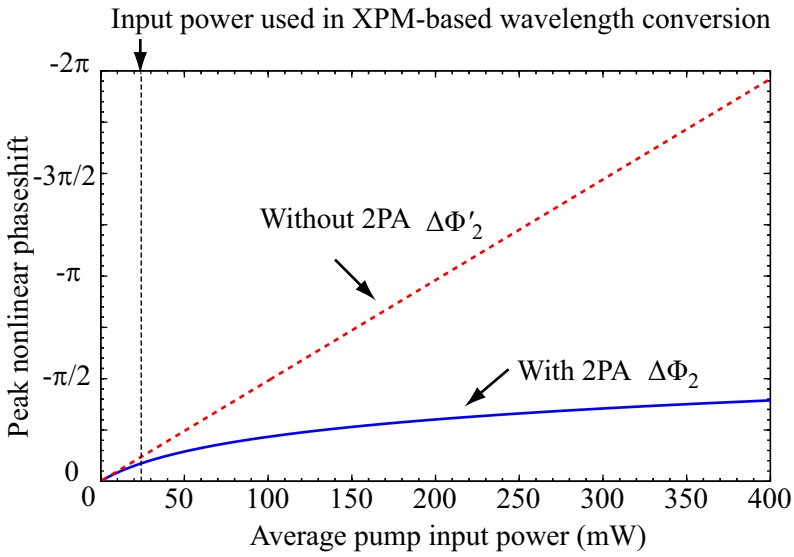

Figure 4.6: Simulation of the nonlinear phase shift as a function of average pump input power with and without 2PA.

grows logarithmically (much more slower) with the pump input power due to 2PA, which reduces the XPM efficiency in these waveguides.

The experimental setup for wavelength conversion using XPM in a GaAs waveguide is depicted in Fig. 4.7 [85]. The setup is similar to the experimental setup for XAM-based wavelength conversion shown in previous section except that here the filters are tuned to block the probe wavelength and only transmit the spectral pedestal associated with XPM. The pump signal was a 10-Gb/s RZ-OOK centered at 1553.5 nm and modulated with a (2^{31}-1) pseudorandom data pattern. The probe signal was a CW beam with a carrier wavelength of 1540 nm. The average coupled input powers of pump and probe signals were 14 dBm and 12 dBm, respectively.

Figure 4.8 summarizes the spectral profiles of the filters detuned to convert the XPM-induced phase modulation to amplitude modulation. The filters were measured

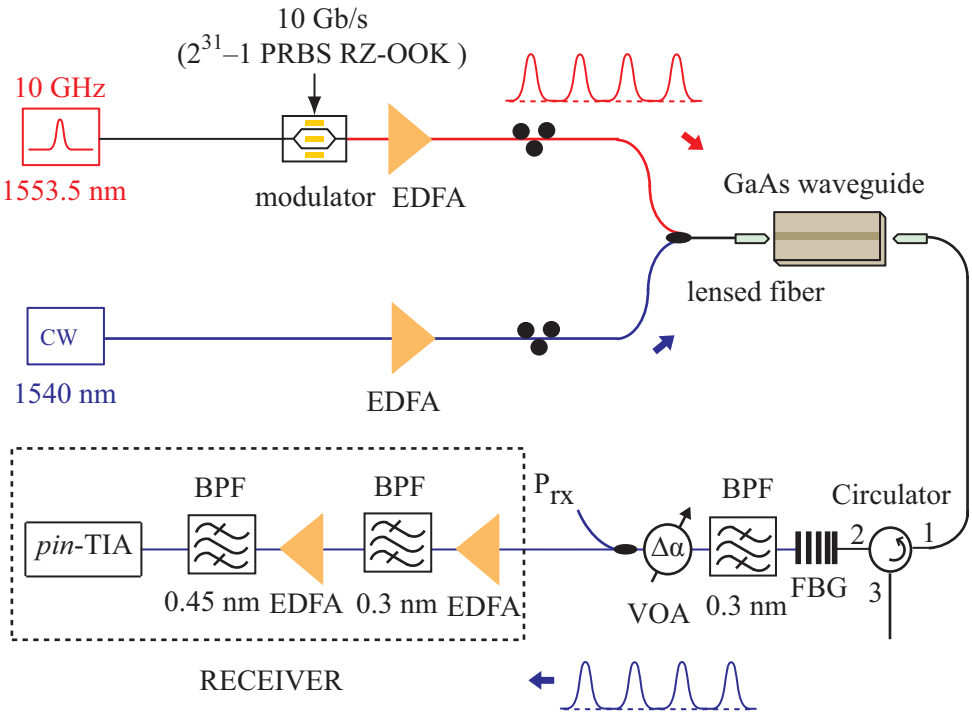

Figure 4.7: Experimental setup for 10 Gb/s wavelength conversion using XPM in a GaAs waveguide. (P_{RX} : receiver power; VOA : variable optical attenuator; EDFA : erbium-doped fiber amplifier; *pin*-TIA : p-i-n photodiode and transimpedance amplifier.)

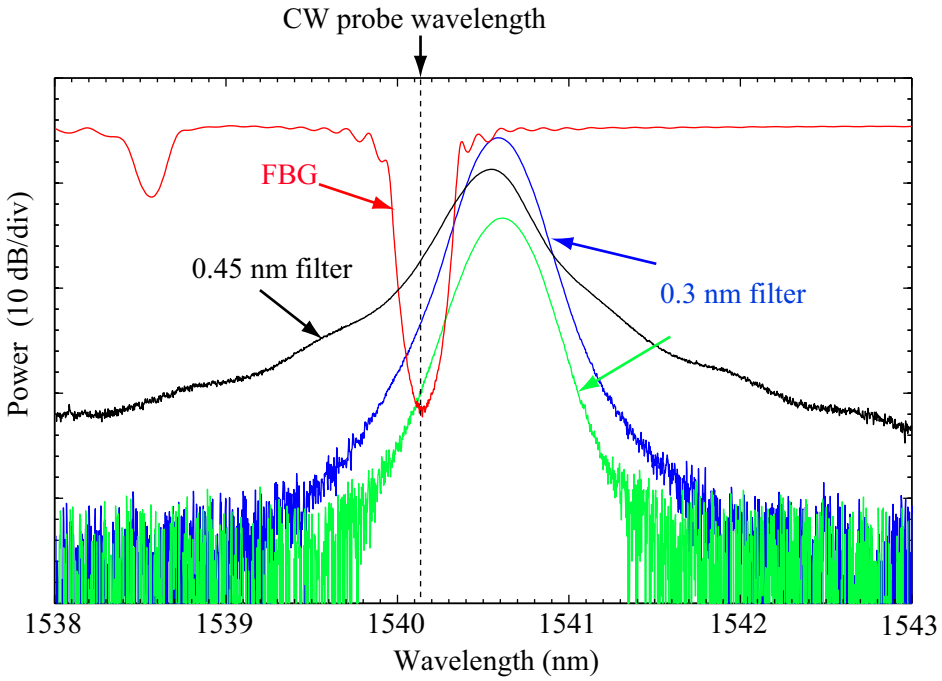

Figure 4.8: The spectral profiles of the filters used in XPM-based wavelength conversion.

by sending the amplified spontaneous emission (ASE) produced from the erbium-doped fiber amplifier (EDFA) to each filter and capturing the output spectrum. Unlike the XAM-based measurement in which all filters were tuned to the carrier wavelength of the CW probe, a fiber Bragg grating (FBG) notch filter was tuned to the carrier wavelength of CW probe in order to suppress the background probe signal. The remaining 0.3-nm filters and a 0.45-nm bandpass filter were detuned by 0.5 nm to the red side of the probe wavelength in order to select the XPM sideband of the probe signal. A circulator in front of the FBG filter was required to redirect the reflected optical power from the FBG notch filter, which would otherwise be reflected back into the waveguide and amplifiers.

Figure 4.9 shows the spectra captured at the input and the output of the waveguide. The spectral pedestal of the probe is attributed to the XPM induced by the pump pulses. We believe that free-carrier dispersion does not play an important role in the phase shift of

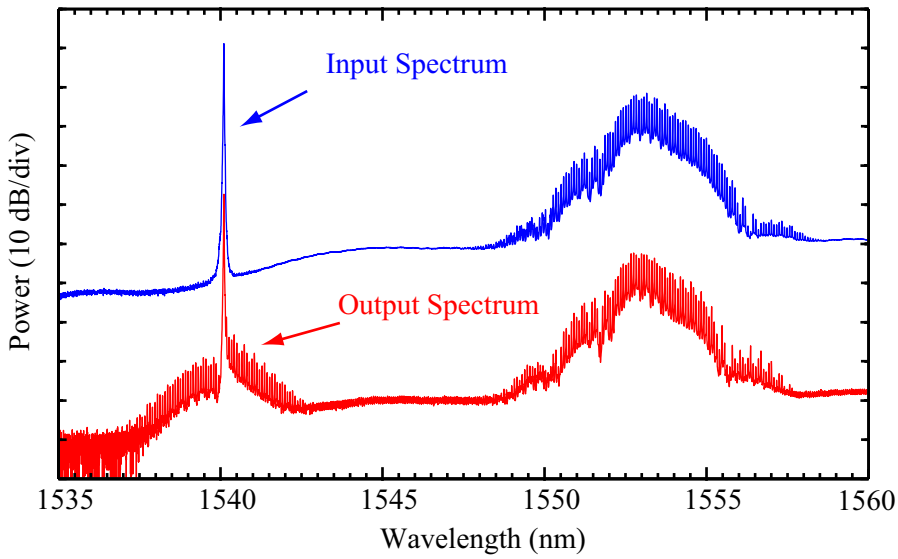

Figure 4.9: Signal spectra collected before the waveguide (blue line) and after the waveguide (red line). The spectra have been offset for clarity.

the probe at this range of input powers. The asymmetric pedestal of the probe is attributed primarily due to the spectral shape of the pump signal and the dispersion in the waveguide.

The dashed line in Fig. 4.10 represents the spectral profile of the composite bandpass filter formed by all filters used in the experiment. The -3 dB and -6 dB bandwidths of the composite filter were 0.17 nm and 0.26 nm, respectively. The red line and the blue line represent the spectra of the output probe before and after the composite filter, respectively. After the composite filter, the residual probe carrier (indicated with a red circle) was suppressed by 30 dB relative to the converted probe signal, when measured at 0.01 nm resolution bandwidth.

Fig. 4.11 shows the eye-diagram of the pump and the converted probe, each captured immediately before the receiver at a received power of -35 dBm. The data were efficiently transferred from the pump to the CW probe. However, the pulse-width of the

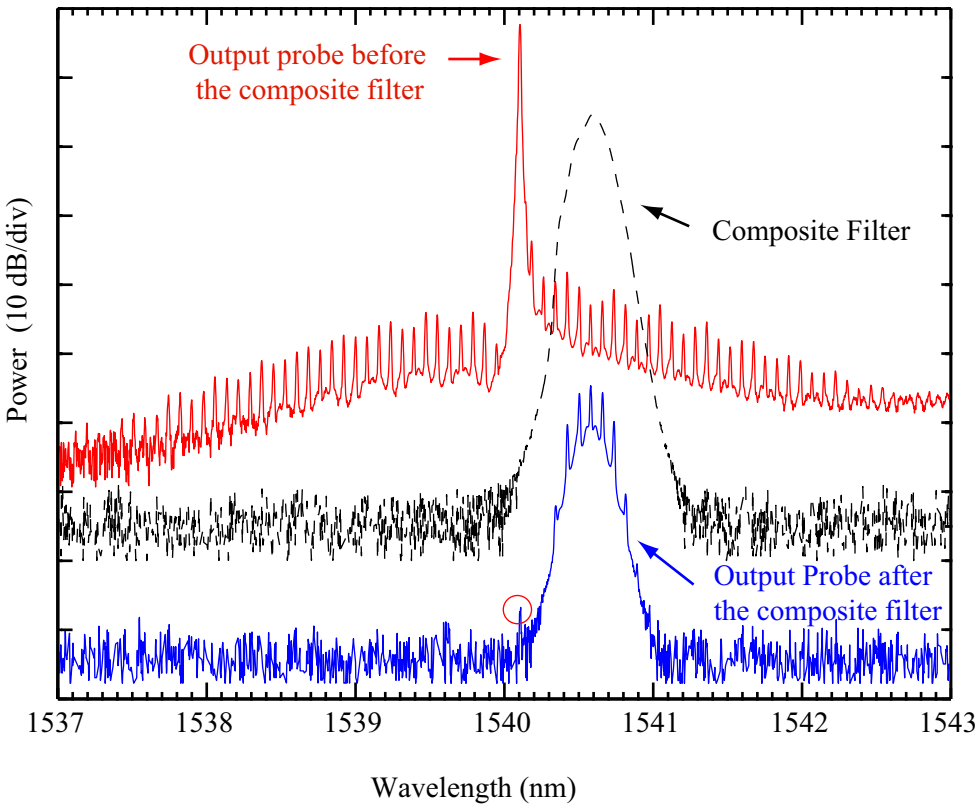

Figure 4.10: Zoomed-in spectra of the output probe before and after the composite filter. The dashed line represents the spectral profile of the composite filter.

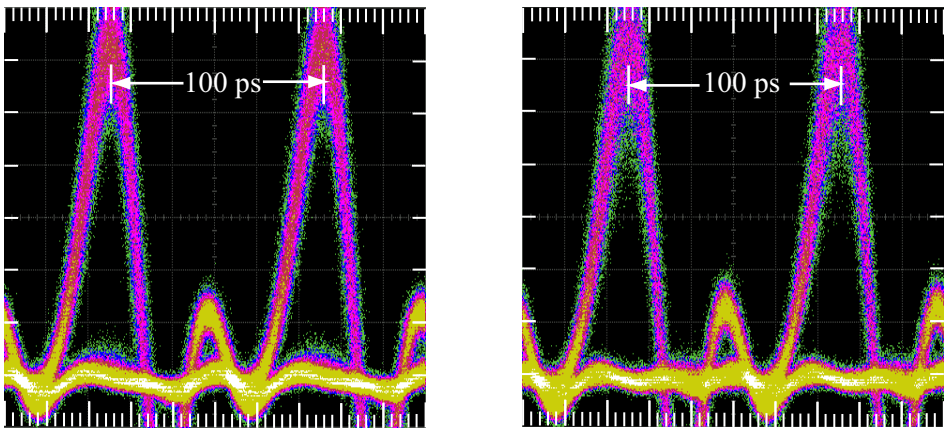

Figure 4.11: Infinite-persistence 10 Gb/s sampling oscilloscope traces: (a) RZ-OOK pump, and (b) converted probe. The artifact in the zero rail is ascribed to the sampling module's RF response.

converted probe was different from that of the pump due to the interaction of the probe with the composite filter. The pulse-width broadening was found to be no more than 20% (measured prior to detection), yielding respective pump and converted probe FWHM pulse-widths of 17 ps and 19 ps. The received pulse-widths were significantly larger than the 3 ps of the original pump, due to convolutions with the 0.17-nm composite bandpass filters. Consequently, no receiver sensitivity penalty due to pulse-width broadening was expected for the converted probe.

Fig. 4.12 summarizes the pre-amplified receiver sensitivity measurements. The baseline RZ-OOK pump receiver sensitivity was -37 dBm at 10^{-9} BER, and was measured by bypassing the GaAs waveguide, FBG notch filter and 0.3-nm filter before the receiver and tuning the remaining filters in the receiver to the pump wavelength. The converted RZ-OOK probe demonstrated a penalty of 0.7 dB relative to the baseline RZ-OOK

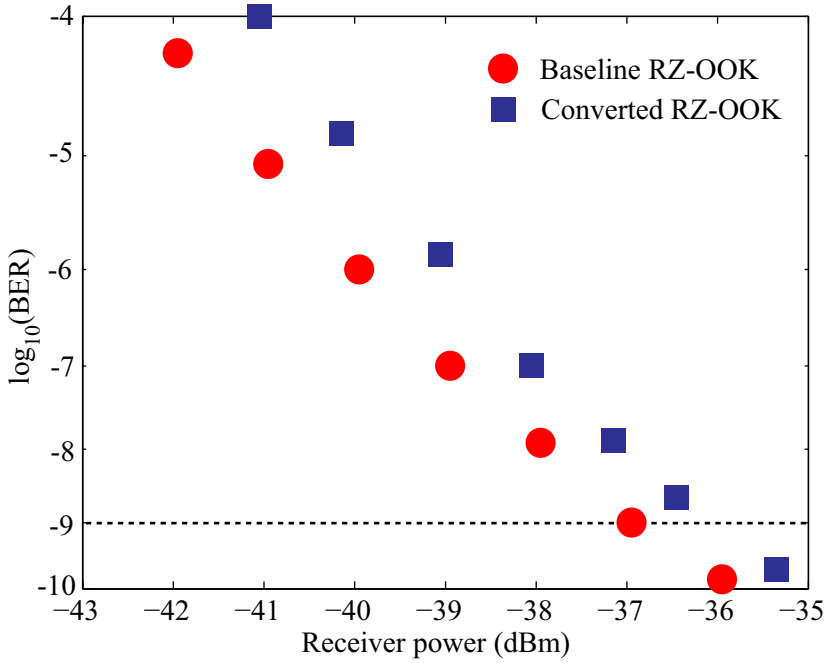

Figure 4.12: BER versus received power for 10 Gb/s XPM-based wavelength conversion.

from the pump signal.

4.3 Wavelength Conversion Using Four-Wave Mixing

Four-wave mixing (FWM) is another nonlinear processes that has been used for optical signal processing. Unlike cross-phase modulation, FWM involves the generation of new wavelengths via interaction between four optical waves. Figure 4.13 depicts the basic diagram of FWM process in an optical waveguide. When a strong pump at frequency ω_p and a co-propagating signal at frequency ω_s are launched in the waveguide, the refractive index of the waveguide can be periodically modulated by the optical Kerr nonlinear effect at the beat frequency of ω_s-ω_p. For partially-degenerate FWM, the pump wave at ω_p becomes phase modulated with the beat frequency ω_s-ω_p and generates sidebands at frequencies $\omega_p \pm (\omega_s\text{-}\omega_p)$ [5]. One sideband is located at ω_s which results in a gain for the

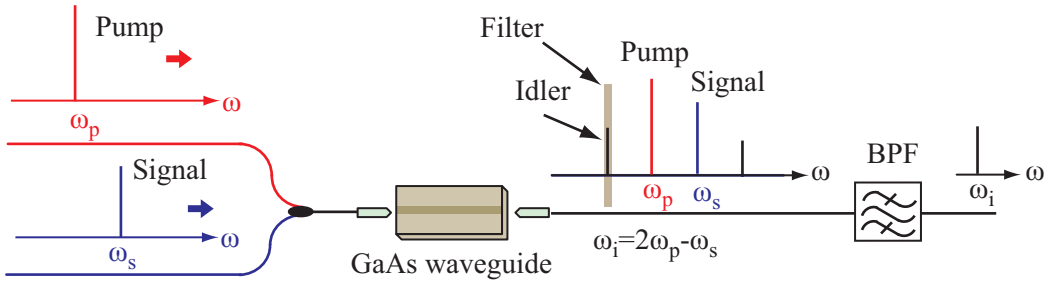

Figure 4.13: Wavelength conversion using four-wave mixing in a GaAs waveguide.

signal. The other sideband will generate a new optical wave at frequency $\omega_i = 2\omega_p - \omega_s$, which is called the idler. The idler is only generated in the presence of both the pump and the signal and its idler power is proportional to the signal power and the square of the pump power. Wavelength conversion using FWM can be achieved by spectrally isolating the idler wave. Note that a different idler wave can also be generated at $2\omega_s - \omega_p$ from the sideband of the signal at frequency ω_s. Its power is proportional to the pump power and the square of the signal power, which is weaker than the idler at ω_i.

The nonlinear optical interaction of the pump, signal and idler generated by FWM in the waveguide can be modeled by following propagation equations [86, 87]

$$\begin{aligned}\frac{dP_p(z)}{dz} = &-\alpha P_p(z) - \frac{\beta_{2PA}}{A_{eff}}\left[P_p(z) + 2P_s(z) + 2P_i(z)\right]P_p(z) \\ &- 4\frac{\omega n_2}{cA_{eff}}P_p(z)\sqrt{P_s(z)P_i(z)}\sin\left[\theta(z)\right] \\ &- \frac{2\beta_{2PA}}{A_{eff}}P_p(z)\sqrt{P_s(z)P_i(z)}\cos\left[\theta(z)\right] \end{aligned} \tag{4.12}$$

$$\frac{dP_s(z)}{dz} = -\alpha P_s(z) - \frac{\beta_{2PA}}{A_{\text{eff}}}\left[2P_p(z) + P_s(z) + 2P_i(z)\right]P_s(z) + 2\frac{\omega n_2}{cA_{\text{eff}}}P_p(z)\sqrt{P_s(z)P_i(z)}\sin\left[\theta(z)\right] - \frac{\beta_{2PA}}{A_{\text{eff}}}P_p(z)\sqrt{P_s(z)P_i(z)}\cos\left[\theta(z)\right] \tag{4.13}$$

$$\frac{dP_i(z)}{dz} = -\alpha P_i(z) - \frac{\beta_{2PA}}{A_{\text{eff}}}\left[2P_p(z) + 2P_s(z) + P_i(z)\right]P_i(z) + 2\frac{\omega n_2}{cA_{\text{eff}}}P_p(z)\sqrt{P_s(z)P_i(z)}\sin\left[\theta(z)\right] - \frac{\beta_{2PA}}{A_{\text{eff}}}P_p(z)\sqrt{P_s(z)P_i(z)}\cos\left[\theta(z)\right] \tag{4.14}$$

and

$$\begin{aligned}\frac{d\theta(z)}{dz} =& \Delta\beta_o + \phi_{\text{NL}} \\ =& \Delta\beta_o + \frac{\omega n_2}{cA_{\text{eff}}}\left[2P_p(z) - P_s(z) - P_i(z)\right] \\ &+ \frac{\omega n_2}{cA_{\text{eff}}}\left[P_p(z)\sqrt{\frac{P_s(z)}{P_i(z)}} + P_p(z)\sqrt{\frac{P_i(z)}{P_s(z)}} - 4\sqrt{(P_s(z)P_i(z)}\right]\cos\left[\theta(z)\right] \\ &+ \frac{\beta_{2PA}}{A_{\text{eff}}}\left[P_p(z)\sqrt{\frac{P_s(z)}{P_i(z)}} + P_p(z)\sqrt{\frac{P_i(z)}{P_s(z)}} - 4\sqrt{(P_s(z)P_i(z))}\right]\sin\left[\theta(z)\right] \quad ,\end{aligned} \tag{4.15}$$

where P_p, P_s and P_i are the respective pump, signal and idler powers, and $\theta = \Delta\beta_o z + \phi_{\text{NL}}$, $\phi_{\text{NL}} = \phi_s + \phi_i - 2\phi_p$ is the nonlinear phase shift, ϕ_p, ϕ_s and ϕ_i are the respective pump, signal and idler phases. $\Delta\beta_o = \beta_s + \beta_i - 2\beta_p$ is the linear phase mismatch, where β_p, β_s and β_i are the respective pump, signal and idler propagation constants, and c is the velocity of light. Here we assume that the optical angular frequencies of the pump, signal and idler are close to each other and can be represented as ω and we neglect the spectral dependence of n_2 and β_{2PA} over the region of wavelengths.

On the RHS of Eqs. (4.12)-(4.14), the second term corresponds to degenerate and non-degenerate 2PA. The third and the fourth terms correspond to FWM contributed from the real and imaginary parts of the third-order nonlinear susceptibility $\chi^{(3)}$, respectively. These last two terms are also responsible for the power transfer between the interacting signals, governed by the phase relation θ. Note that $\theta = \pi/2$ at the input of the waveguide, provide that the pump and signal are incident and the idler is generated after an infinitesimal propagation distance in the waveguide [86]. The coupled equations (4.12)-(4.15) can be solved numerically to simulate the FWM conversion efficiency and bandwidth in a GaAs waveguide.

To better understand the conversion efficiency and bandwidth of the FWM process, Eqs. (4.12)-(4.14) are simplified under the assumption that the pump remains undepleted ($\frac{dP_p(z)}{dz} = 0$). The propagation loss and 2PA are also neglected. An approximate solution can be derived for the remaining coupled equation as [5, 39, 87]

$$P_s(L) = P_s(0)\left(1 + \left[\frac{\gamma P_p}{g}\sinh(gL)\right]^2\right) \tag{4.16}$$

$$P_i(L) = P_s(0)\left[\frac{\gamma P_p}{g}\sinh(gL)\right]^2 , \tag{4.17}$$

where L is the waveguide length and $\gamma = \omega n_2/cA_{\text{eff}}$ is the nonlinear parameter. The parametric gain coefficient g is defined as

$$g^2 = [(\gamma P_p)^2 - (\kappa/2)^2] = -\Delta\beta_o\left[\frac{\Delta\beta_o}{4} + \gamma P_p\right] , \tag{4.18}$$

where $\kappa = \Delta\beta_o + 2\gamma P_p$ is an effective phase mismatch, $\Delta\beta_o \cong -(2\pi c/\lambda_p^2)D\Delta\lambda^2$ where D is the second-order dispersion parameter and $\Delta\lambda$ is the wavelength detuning of the signal

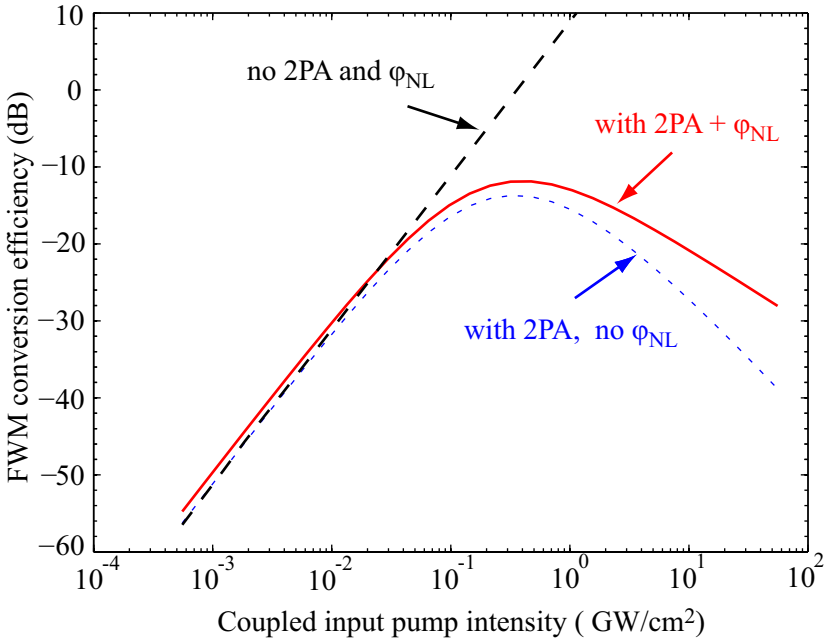

Figure 4.14: Simulation of FWM conversion efficiency when $\Delta\lambda \approx 0$ as a function of average coupled input intensity of the pump. The black dashed line represents η without 2PA and ϕ_{NL}. The blue dashed curve represents η with 2PA, but no ϕ_{NL}. The red solid curve represents η with both 2PA and ϕ_{NL}.

from the pump. The GaAs waveguide used in this experiment has a relative large effective area ($1.8\mu m^2$), therefore the material dispersion is the dominant source of dispersion in this waveguide, rather than modal dispersion. GaAs exhibits normal dispersion ($D < 0$) at the 1500-nm spectral regime. As a result, $\Delta\beta_o$ becomes positive and g becomes imaginary. The FWM conversion efficiency η, defined as the ratio between output power of the idler and the input power of the signal, can be described as

$$\eta = \frac{P_i(L)}{P_s(0)} = (\gamma P_p L)^2 \mathrm{sinc}^2(|g|L) \quad . \tag{4.19}$$

According to Eq. (4.19), the FWM conversion efficiency η is a sinc^2 function of the wavelength detuning $\Delta\lambda$. The largest conversion efficiency η occurs when $\Delta\lambda \approx 0$

($\omega_p \approx \omega_s$). η can be improved by increasing the pump power or using a waveguide with a higher nonlinear parameter γ or with a longer interaction length. As previously mentioned, γ could be further increased by reducing the guided-mode area of the waveguides. However, the linear propagation loss and 2PA, which were not included in the derivation of Eq. (4.19), could impede the nonlinear interaction in the waveguide as the guided-mode area gets smaller or the pump power gets stronger.

To account for both linear propagation loss and 2PA, Eqs. (4.12)-(4.14) are simplified under the assumption that $|P_p| \gg |P_s| \gg |P_i|$ such that the signal and the idler induced 2PA can be neglected. We neglect FWM terms for the pump and signal (the third and the fourth terms in Eq. (4.12) and Eq. (4.13)). We also neglect the linear phase mismatch ($\Delta\beta_o = 0$) and the nonlinear phase shift ($\phi_{NL} = 0$). We also set $\theta = \pi/2$ at the input of the waveguide. Under these assumptions, FWM conversion efficiency η can be solved analytically [88]:

$$\eta = \frac{P_i(L)}{P_s(0)} = \exp(-\alpha L)\left[\frac{A_{\text{eff}}\gamma}{\beta_{2PA}}\right]^2 \left[\frac{\ln\left(1+\frac{\beta_{2PA}P_{po}L_{\text{eff}}}{A_{\text{eff}}}\right)}{\left(1+\frac{\beta_{2PA}P_{po}L_{\text{eff}}}{A_{\text{eff}}}\right)}\right]^2 , \tag{4.20}$$

where P_{po} is the input pump power.

We simulated the FWM conversion efficiency η as a function of average coupled input intensity of the pump wave, as shown in Fig. 4.14. The black dashed line represents the FWM conversion efficiency obtained by neglecting the linear propagation loss, 2PA and nonlinear phase shift ϕ_{NL} using Eq. (4.19). In this lossless case, η grows in proportional to the square of the input pump intensity, as expected. The blue dashed curve shown in Fig. 4.14 was obtained by including the propagation loss and 2PA, but neglect-

ing ϕ_{NL} in the simulation based on Eq. (4.20). At high input intensity, η deviates from the straight line, obtained in the lossless case, and eventually decreases as the input intensity increases due to 2PA. In this case, η reaches the maximum value of

$$\eta_{max} = \exp(-\alpha L)\left[\frac{A_{eff}\gamma}{\beta_{2PA}}\right]^2 \quad , \tag{4.21}$$

at an optimum input intensity of

$$I_{po}^{opt} = \frac{P_{po}^{opt}}{A_{eff}} = \frac{e-1}{\beta_{2PA}L_{eff}} \quad . \tag{4.22}$$

In the previous two cases, we set $\theta = \pi/2$ at the input of the waveguide. Since $\Delta\beta_o + \phi_{NL} = 0$, θ stays $\pi/2$. As a result, the FWM contributed from $\mathrm{Im}\{\chi^{(3)}\}$ does not contribute to the generation of the idler ($\cos(\theta) = 0$). The red solid curve shown in Fig. 4.14 was obtained by numerically solving Eqs. (4.12)-(4.15), which includes the propagation loss, 2PA and ϕ_{NL} in the simulation. ϕ_{NL} causes a change in θ in Eq. (4.15) and lead to the inclusion of the FWM contributed from both $\mathrm{Re}\{\chi^{(3)}\}$ and $\mathrm{Im}\{\chi^{(3)}\}$. As a result, η is slightly larger than that in the previous two cases.

To characterize FWM in a GaAs waveguide, we measured the FWM conversion efficiency as a function of wavelength detuning as shown in Fig. 4.15. In this measurement, the pump and signal were generated from two tunable CW lasers. Both pump and signal were combined and coupled to the GaAs waveguide using a lensed fiber with coupled input powers estimated to be 21.3 dBm and 18.5 dBm respectively. The 3-dB conversion bandwidth (half-width) was measured to be 24 nm. Figure 4.15(a) depicts the output spectrum from the waveguide for the pump-signal detuning of 5 nm, showing a FWM

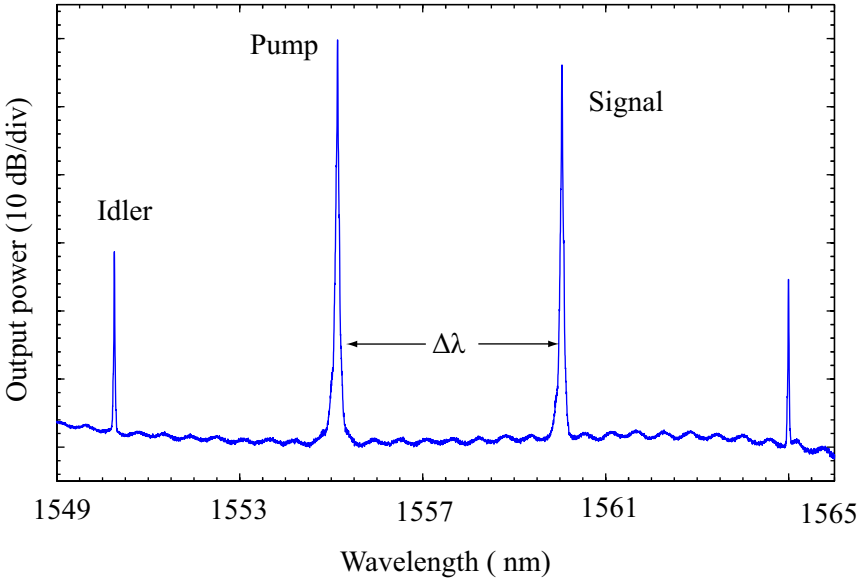

(a)

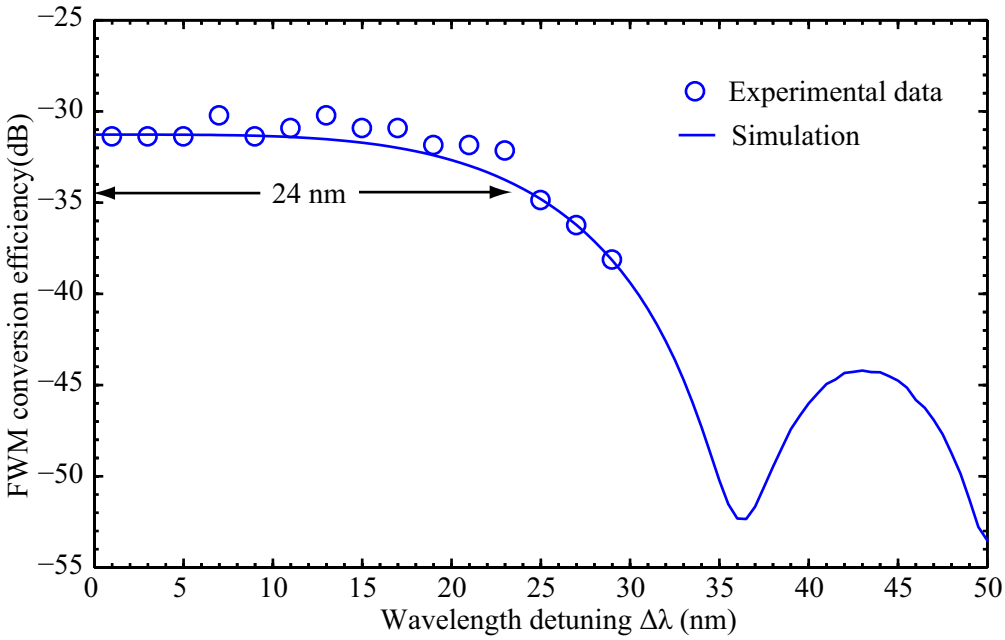

(b)

Figure 4.15: (a) The FWM output spectrum measured after a GaAs waveguide with the wavelength detuning of 5 nm. (b) Measured and simulated conversion efficiency as a function of wavelength detuning.

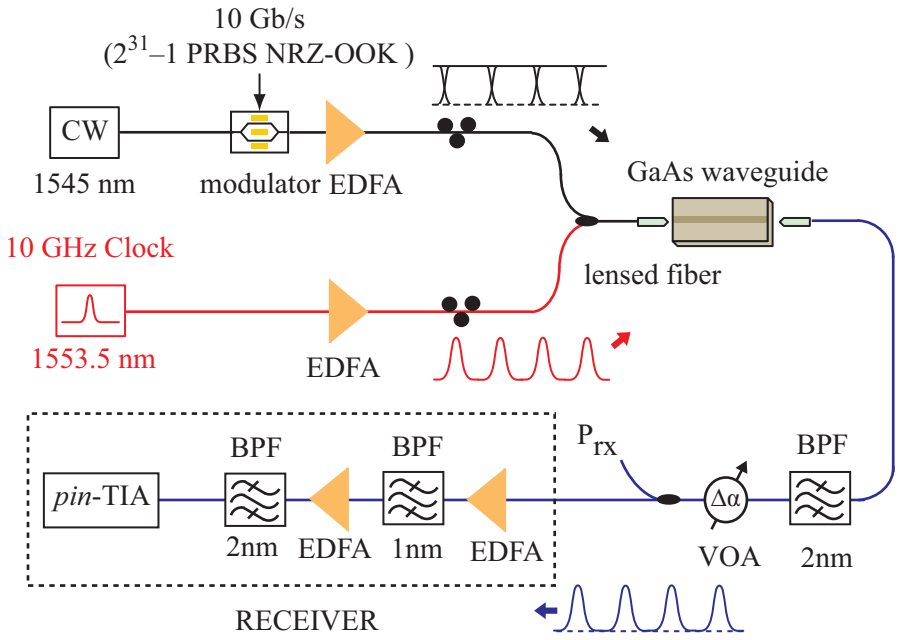

Figure 4.16: Experimental setup for 10 Gb/s NRZ-to-RZ format and wavelength conversion. (P_{RX} : receiver power; VOA : variable optical attenuator; EDFA : erbium-doped fiber amplifier; *pin*-TIA : p-i-n photodiode and transimpedance amplifier.)

conversion efficiency of -31.5 dB.

The solid line in Fig. 4.15(b) shows the best-fit simulation. Based on the peak conversion efficiency measured for small wavelength separation, γ is estimated to be 64 $W^{-1}m^{-1}$, comparable to the calculated value of 35 $W^{-1}m^{-1}$ based on n_2 previously published in [17]. The discrepancy is attributed to a pump-signal polarization mismatch and the uncertainty in the coupling efficiencies at the input and output facets. The measurement wavelength range was limited by the gain of the EDFA, which precluded the measurement of FWM conversion efficiency beyond 30 nm. The dispersion parameter D of the waveguide is estimated to be -1340 ps/(nm-km) based on the 3-dB conversion bandwidth.

The experimental setup for the NRZ-to-RZ format and wavelength conversion using FWM in a GaAs waveguide is shown in Fig. 4.16 [89]. The NRZ-OOK data signal at the wavelength of 1545 nm was generated by modulating the output from a CW laser with a (2^{31}-1) pseudorandom data pattern. The 10-GHz clock pulse train was generated from a mode-locked laser diode centered at 1553.5 nm with the pulse width of 3 ps. The NRZ signal and the clock pulse train were combined and coupled into the waveguide using a lensed fiber. The average coupled input powers for the NRZ-OOK signal and the clock pulse train were estimated to be 23 dBm and 13.6 dBm respectively. The signal emerging from the waveguide was then collected using a lensed fiber and bandpass-filtered by a 2-nm tunable grating filter to spectrally isolate the generated RZ-OOK signal from the original NRZ-OOK and the clock pulses. The pre-amplified receiver, which was pre-optimized for RZ-OOK reception, consisted of a low-noise linear EDFA, a 1-nm filter, a power EDFA, and a 2-nm filter. The detected signal was then amplified using a linear trans-impedance amplifier prior to BER evaluation.

Figure 4.17 depicts the optical spectrum output from the waveguide. The generated RZ-OOK was at the idler wavelength of 1536.5 nm for a pump-signal detuning of 8.5 nm, which was within the range where the FWM conversion efficiency was flat. The dashed trace in Fig. 4.17 represents the spectral profile of the composite bandpass filter, which includes the grating filter and the two filters in the receiver. Figure 4.18 shows the spectrum of converted signal after passing through these filters.

Figure 4.19(a), (b) and (c) show the eye-diagrams of the baseline NRZ-OOK, baseline RZ-OOK and converted RZ-OOK signals respectively. The converted signal quality slightly degraded compared to the baseline, which we attribute to the low conversion ef-

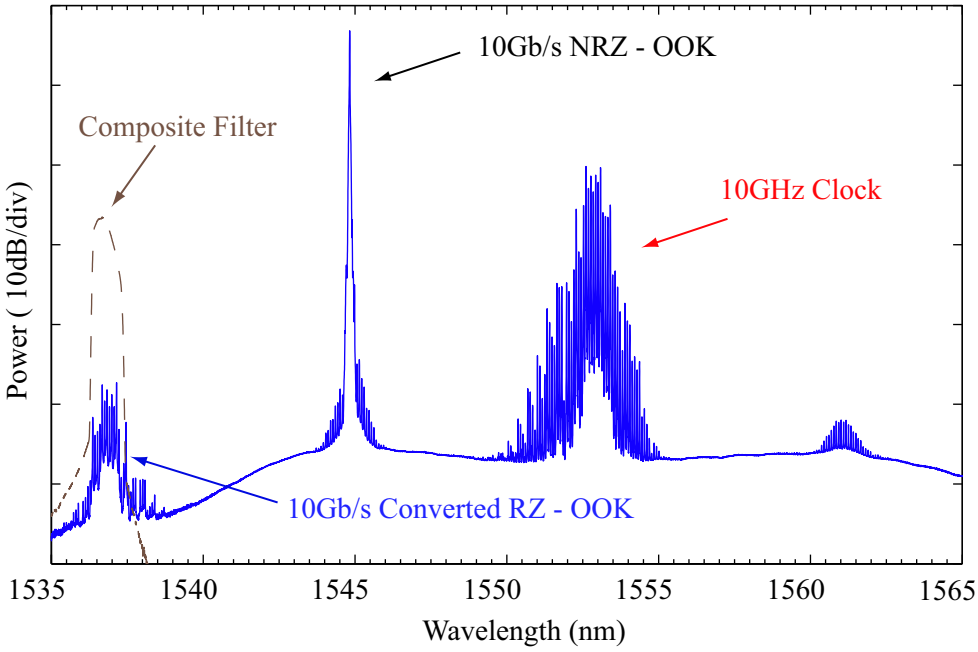

Figure 4.17: Optical spectrum of the output beam from the waveguide (solid line) and the spectral profile of the bandpass filter (dashed line).

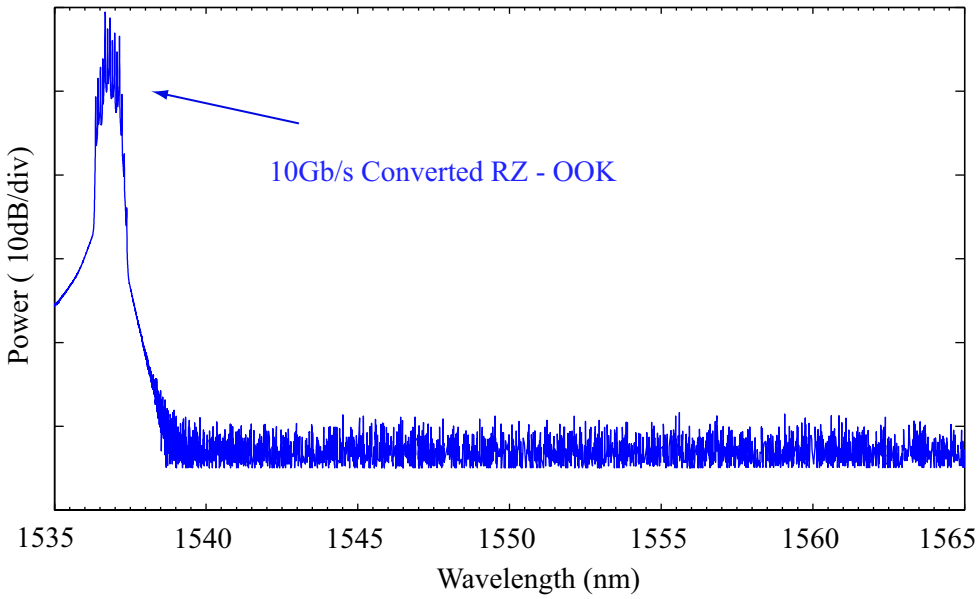

Figure 4.18: Zoomed-in spectrum of converted signal after passing through filters.

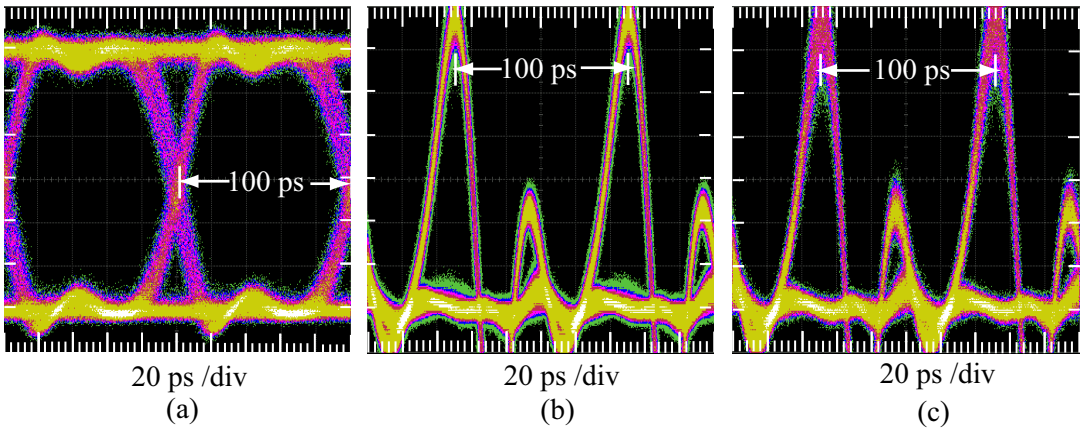

Figure 4.19: Infinite-persistence sampling oscilloscope traces of (a) Baseline NRZ-OOK signal, (b) Baseline RZ-OOK signal, and (c) Converted RZ-OOK signal. Each trace was captured at -25 dBm receiver power, using a 10-Gb/s sampling module.

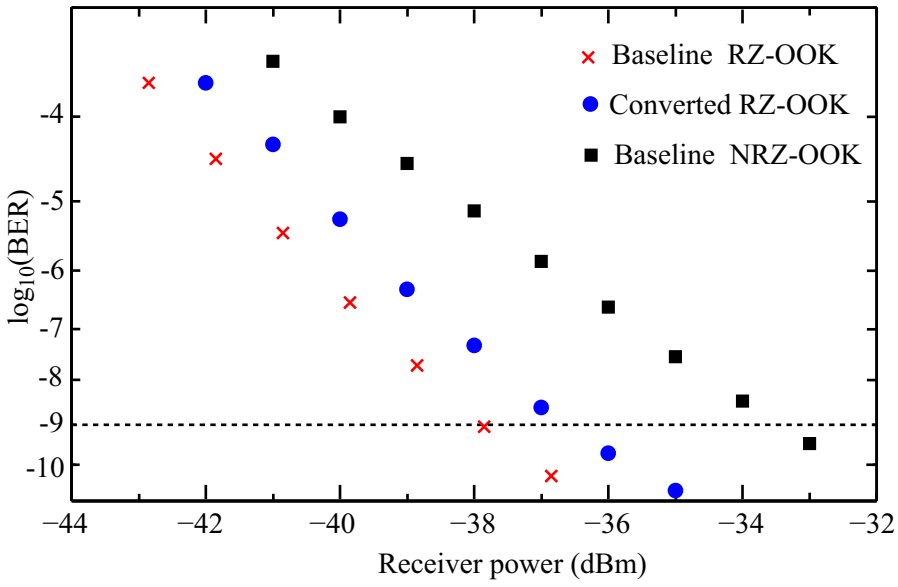

Figure 4.20: Bit-error rate versus received power for 10-Gb/s NRZ-RZ format conversion.

ficiency, for the pump and signal powers used in the experiment. Figure 4.20 shows the receiver sensitivity measurement of the converted signal, in comparison to back-to-back transmission. The converted RZ-OOK signal demonstrated a 10^{-9} BER receiver sensitivity improvement of 2.5 dB relative to the baseline NRZ-OOK signal, and a penalty of 1 dB relative to the baseline RZ-OOK signal.

4.4 Summary

We have demonstrated, for the first time, 10-Gb/s wavelength conversion using cross-amplitude modulation, cross-phase modulation and four-wave mixing in a GaAs bulk waveguide. The XAM-based wavelength conversion has a large BER receiver sensitivity penalty because the majority of the power of the converted signal is allocated to the constant background. The transmitted probe shows no evidence of slow recovery trace induced by free-carrier absorption at the input powers used in the experiment. Wavelength conversion using XPM in a GaAs waveguide with a detuned filter was demonstrated with open eye diagrams and a BER penalty less than 1 dB relative to the baseline RZ-OOK from the pump signal. An all-optical NRZ-to-RZ format and wavelength conversion using FWM in a GaAs waveguide is also described. The FWM system achieves a conversion efficiency of -31.5 dB and the 3-dB bandwidth of 48 nm at the pump power of 21.3 dBm. The converted RZ-OOK signal demonstrated a BER receiver sensitivity improvement of 2.5 dB relative to the baseline NRZ-OOK signal, and a penalty of 1 dB relative to the baseline RZ-OOK signal.

The XPM and FWM effects in GaAs waveguides are limited by two-photon ab-

sorption. This could be suppressed by using an AlGaAs alloy that is designed to have a bandgap larger than twice the photon energy [21]. The XPM and FWM conversion efficiency could be further enhanced with improvements in fabrication to make a waveguide with a lower loss and a smaller guided-mode area. Nonetheless, these experiments demonstrate that GaAs/AlGaAs waveguides are viable for nonlinear optical signal processing.

Chapter 5

Background-free Ultrafast Optical Sampling Using Nondegenerate Two-Photon Absorption in a Gallium Arsenide Photodiode

In this chapter, we describe an ultrafast optical sampling system based on nondegenerate two-photon absorption (2PA) in a GaAs photodiode. We propose the idea of using sampling pulses with a photon energy below the half-bandgap of GaAs for suppressing the large photocurrent associated with two-photon absorption of the strong sampling pulses. We demonstrate a background-suppressed measurement of quasi 4-Tb/s eye diagrams, with temporal resolution that is limited only by the sampling pulsewidth. Finally, we shows preliminary results of a 2PA measurement in a GaAs waveguide detector.

5.1 Sampling Techniques

High-speed waveform sampling is an important diagnostic for optical telecommunication systems. Because optical signals deteriorate as they propagate along the transmission fiber, it is necessary to monitor and keep track of waveform qualities such as rise and fall time, timing jitter and extinction ratio. Figure 5.1 depicts the schematic of three techniques that have been used for sampling of optical waveforms [90].

The most commonly used technique for waveform sampling is an electronic sampling scheme that uses a high-speed photodiode and a high bandwidth sampling oscilloscope, as depicted in Fig. 5.1(a). The sampling resolution is limited to approximately

15–20 ps by the bandwidth of photodiode and electrical circuits. Figure 5.1(b) depicts the sampling scheme, which uses a fast electroabsorption modulator driven by an electrical short pulse to function as a temporal gate. This sampling scheme employs an equivalent-time sampling technique. Optical waveforms can be sampled at a low repetition rate. Therefore, it does not require a fast photodetector or electronics with a response time comparable to the duration of optical waveforms. Sampling systems with bandwidth of 100–200 GHz have been reported using this technique. This system bandwidth is limited by the timing jitter of an electrical short pulse. [91, 92].

Figure 5.1(c) shows a schematic of a nonlinear optical sampling system. Nonlinear optical sampling systems use the nonlinear interaction between the signal and sampling pulses to function as a fast temporal gate opened by a short optical sampling pulse. Several techniques have been proposed for optical sampling including sum-frequency generation (SFG) in nonlinear crystals [93], and four-wave mixing (FWM) or cross-phase modulation (XPM) in highly nonlinear fibers [94, 95] or semiconductor optical amplifiers [96]. The temporal resolution and optical bandwidth of these systems are determined by the combination of the pulse width and the timing jitter of the sampling pulse, as well as by other characteristics of the sampling process such as the walk-off and phase mismatch [97]. Nonetheless, the optical sampling with the temporal bandwidth as fast as 640 GHz has been reported [93]. Note that not only nonlinear effects can be used for optical sampling, but also coherent mixing, which uses linear optics and square-law integrating detectors can be used for optical sampling, as demonstrated in [98].

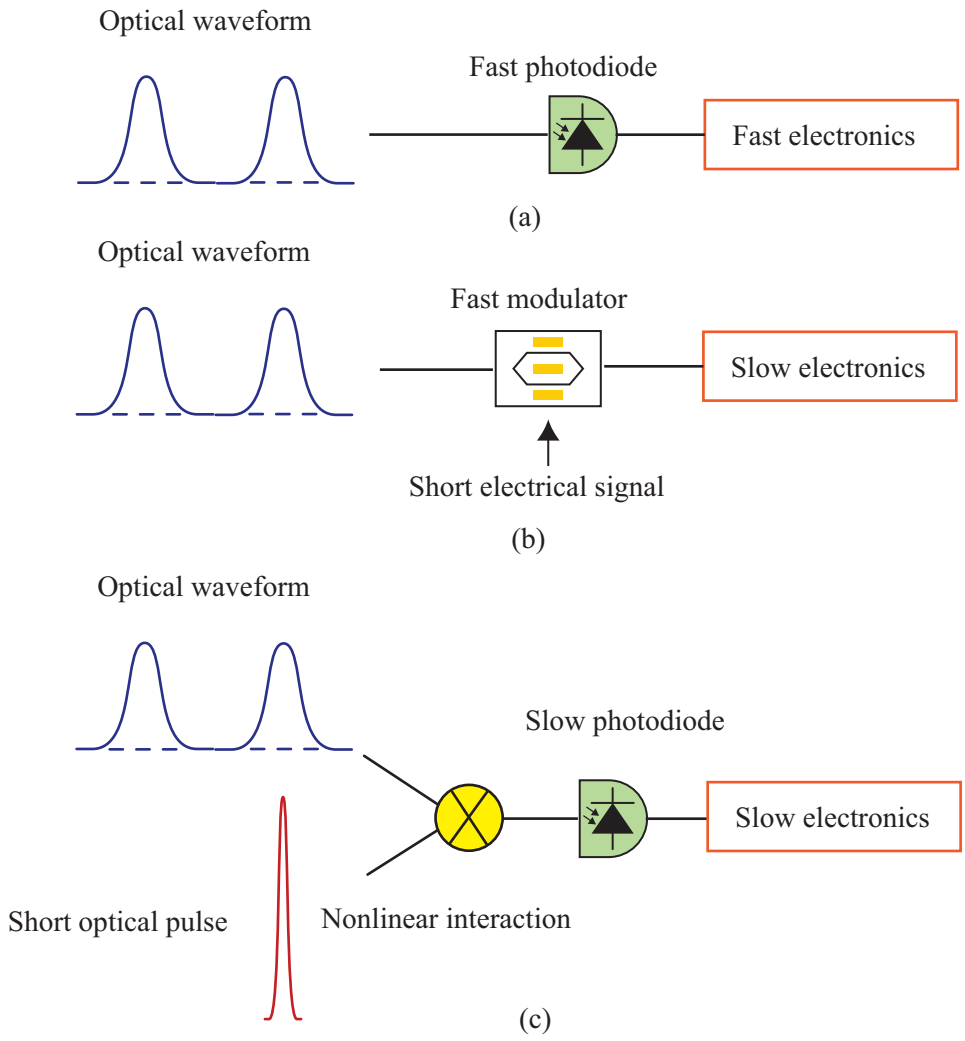

Figure 5.1: Schematic of three sampling techniques: (a) electronic sampling (b) sampling with a fast modulator and (c) nonlinear optical sampling.

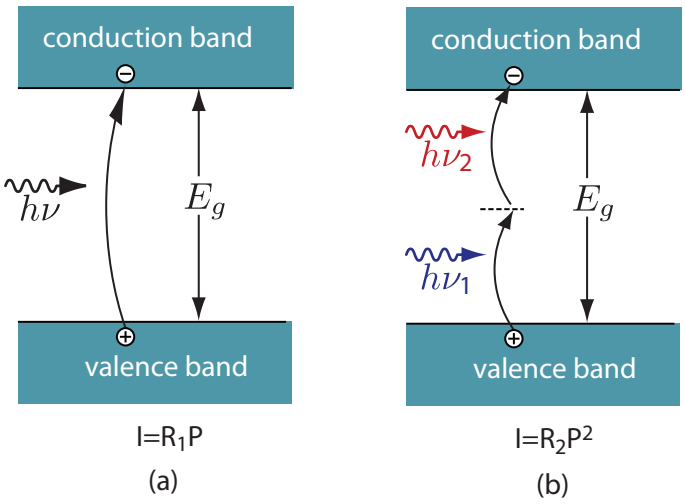

Figure 5.2: (a) Linear detector (b) 2PA detector.

5.2 Two-Photon Absorption

2PA is a nonlinear process in which two photons are simultaneously absorbed and generate a single electron-hole pair in a photodetector. It occurs when a photon, with energy less than the bandgap energy of photodetector but more than half of the bandgap energy, is launched into the photodetector. In this condition, single photon absorption (1PA) is prohibited since a single photon does not have enough energy to overcome the bandgap. However, if the optical intensity is high enough, two photons can be absorbed at the same time to produce a single electron-hole pair. Unlike the conventional photodetectors in which photocurrent is proportional to the input intensity due to 1PA, the photocurrent from 2PA process is proportional to the square of input intensity. Fig. 5.2 shows a schematic representation of single and two-photon absorption processes.

Despite its detrimental effect of hindering many other nonlinear processes, 2PA can be exploited in a variety of optical signal processing applications [99–102]. 2PA has a very fast response time and very wide optical bandwidth. Compared to other nonlinear

processes such as SFG and FWM, 2PA does not require phase matching. 2PA directly generates a measurable nonlinear photocurrent, thereby eliminating the need for an external optical filter and detector. In this work, we demonstrate optical sampling system using 2PA in a photodetector. 2PA-based optical sampling is also compact and inexpensive.

5.3 Conventional Optical Sampling Using Two-Photon Absorption

Figure 5.3(a) depicts the typical measurement setup for optical sampling based on 2PA. The signal and sampling pulse wavelengths are chosen to satisfy the following inequalities,

$$h\nu_1 \approx h\nu_2 < E_g < h(\nu_1 + \nu_2) \ , \tag{5.1}$$

where E_g denotes the bandgap energy of the photodetector and ν_1 and ν_2 are the signal and sampling frequencies, respectively. Under this condition, the intensity cross-correlation photocurrent $i_{\mathrm{ph}}(\tau)$ from the signal and sampling pulses as a function of delay τ can be described by [103]

$$i_{\mathrm{ph}}(\tau) = k\left[\frac{2\beta_{12}}{h\nu_1}\langle P_1(t)P_2(t-\tau)\rangle + \frac{\beta_{11}}{2h\nu_1}\left\langle P_1^2(t)\right\rangle + \frac{\beta_{22}}{2h\nu_2}\left\langle P_2^2(t-\tau)\right\rangle\right] \ , \tag{5.2}$$

where $\langle . \rangle$ indicates a time average, k is a proportionality constant that depends on the focus spot size, reflection, coupling efficiency and probability of carrier generation after two-photon absorption process, β_{12} is the non-degenerate 2PA coefficient between the signal and sampling pulses, β_{11} and β_{22} are the degenerate 2PA coefficients at the wavelength of signal and sampling pulses, respectively, and P_1 and P_2 are the signal power

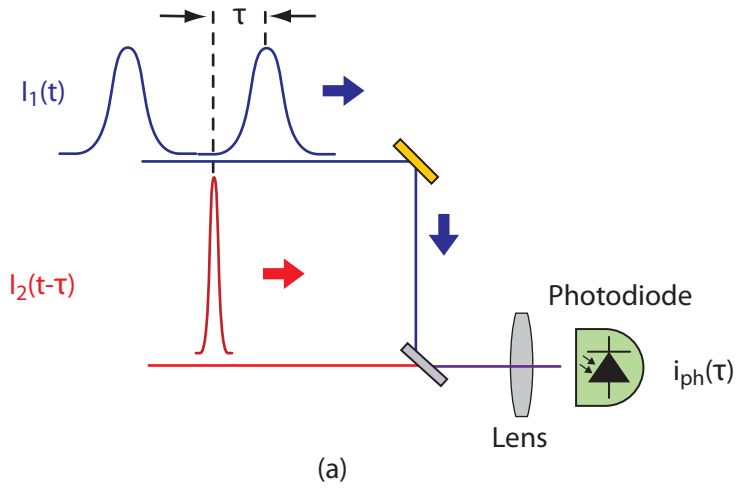

Figure 5.3: (a) The measurement setup for optical sampling based on 2PA. (b) Three dominant nonlinear processes that contribute to photocurrent when $h\nu_1 \approx h\nu_2 < E_g < h(\nu_1 + \nu_2)$: (i) nondegenerate 2PA from sampling and signal pulses, (ii) 2PA from signal pulses and (iii) 2PA from sampling pulses.

and sampling power, respectively. Based on Eq 5.2, there are three dominant multiphoton absorption processes the can contribute to the measured photocurrent, as depicted in Fig. 5.3(b). Among these processes, non-degenerate 2PA between the signal and sampling pulses (i) only occurs if the signal and sampling pulses temporally coincide in the detector. Degenerate 2PA of the signal (ii), and the sampling pulses (iii) together constitute a background photocurrent that does not depend on the temporal alignment τ.

While 2PA is widely used in time-averaged autocorrelation and cross-correlation measurements [104–106], it presents a challenge when there is a disparity between the signal and sampling powers. In sampling applications, the sampling pulse is typically chosen to have a much higher peak intensity than the signal, which in turn generates a large background photocurrent through degenerate 2PA of the sampling pulses. This background photocurrent, and the shot-noise associated with it, can easily overwhelm the small non-degenerate 2PA signal one seeks to measure. When the signal wavelength is comparable to the sampling wavelength ($h\nu_1 \approx h\nu_2$), the difference among 2PA coefficients in Eq 5.2 (β_{12}, β_{11} and β_{22}) is negligible. The signal-to-background ratio can never exceed 3:1 with the highest contrast ratio of 2:1 occurring when the signal and sampling pulses have equal power. Fig. 5.4(a) shows the simulated cross-correlation between the signal and sampling pulses when both pulses have equal power. When the sampling power is ten times larger than the signal power, the signal-to-background ratio reduced to 0.4:1, as depicted in Fig. 5.4(b), due to a strong background current from the sampling pulses. In the next section, we show that this background photocurrent can be suppressed by using long-wavelength sampling pulses below the half-bandgap of the photodetector such that two photons from the sampling pulses do not have enough energy to be absorbed through

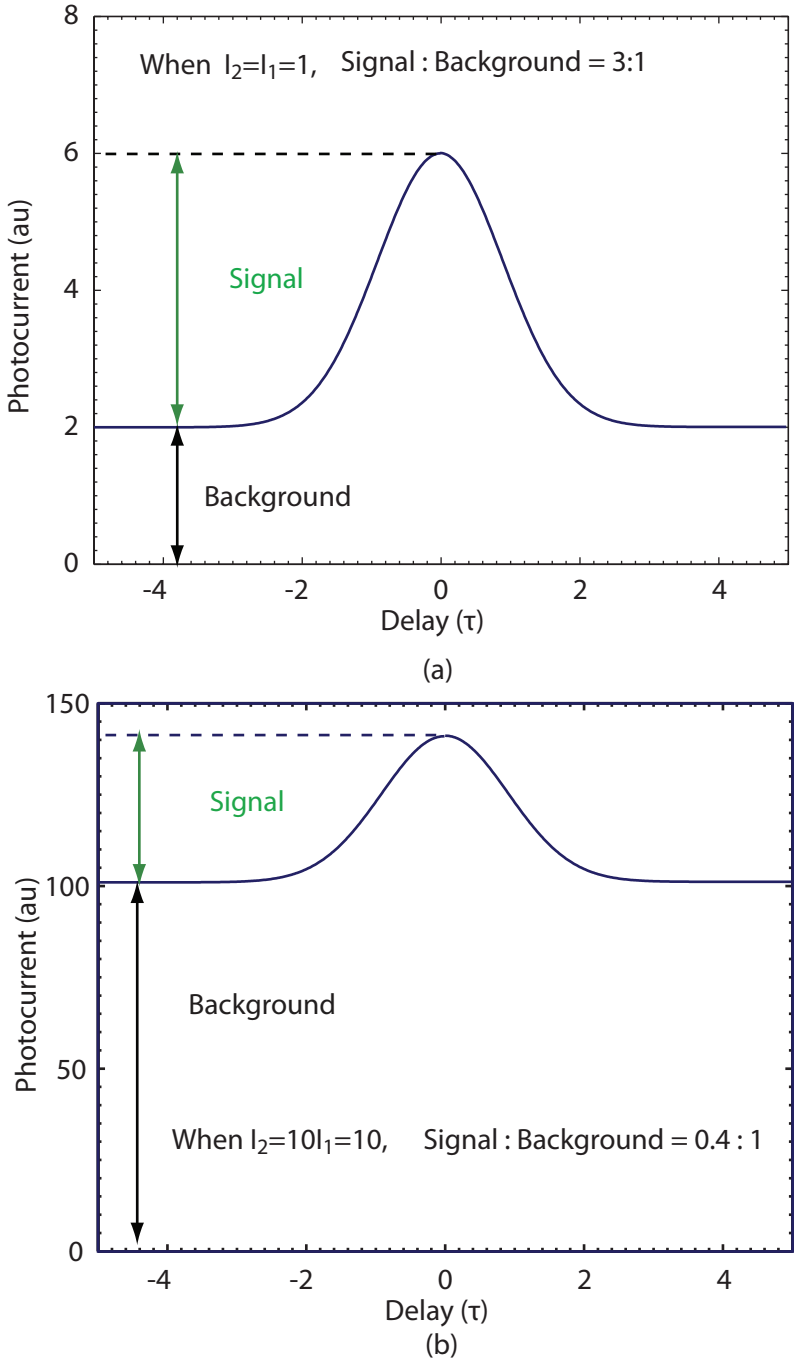

Figure 5.4: Simulated cross-correlation between sampling and signal pulses when (a) both pulses have equal power. (b) the sampling power is ten times larger than the signal power.

2PA. However, with the spatial and temporal coincidence of signal pulses, one photon from a sampling pulse and one from a signal pulse can be simultaneously absorbed to generate a photocurrent through non-degenerate 2PA.

5.4 Background Suppression Technique

The background photocurrent can be suppressed by choosing signal and sampling wavelengths to satisfy the following inequalities,

$$2h\nu_2 < E_g < h(\nu_1 + \nu_2) < 2h\nu_1 < 3h\nu_2 \ . \tag{5.3}$$

The left-most inequality ($2h\nu_2 < E_g$) expresses the important constraint that two-photon absorption of the sampling pulses is prohibited because the sampling photon energy falls below the half-bandgap of the photodetector. Although the sampling pulses could generate photocurrent via degenerate three-photon absorption (3PA) since $E_g < 3h\nu_2$, at the input power used in the experiment, the 3PA photocurrent is very small compared with the 2PA photocurrent. Under the constraints in inequalities (5.3), the three dominant nonlinear processes that contribute to photocurrent are depicted in Fig. 5.5. The signal photocurrent is still produced by non-degenerate 2PA between the signal and sampling pulses (i) ($E_g < h(\nu_1 + \nu_2)$), while the background photocurrent is generated by degenerate 2PA from the signal pulses (ii) ($E_g < 2h\nu_1$) and three-photon absorption from the sampling pulses (iii) ($E_g < 3h\nu_2$). The cross-correlation photocurrent can now be described by

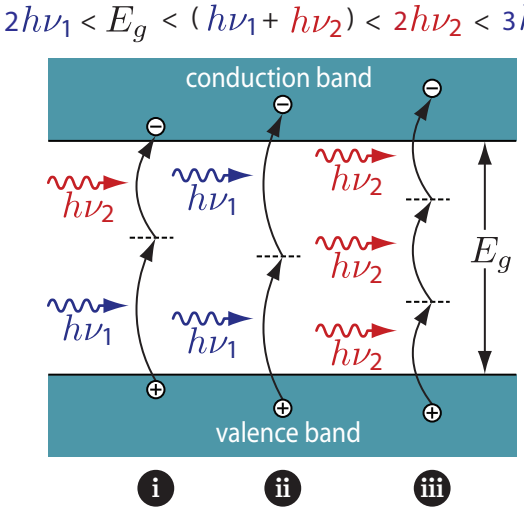

Figure 5.5: Three dominant nonlinear processes that contribute to photocurrent when $2h\nu_2 < E_g < h(\nu_1+\nu_2) < 2h\nu_1 < 3h\nu_2$: (i) nondegenerate 2PA from sampling and signal pulses, (ii) 2PA from signal pulses and (iii) 3PA from sampling pulses.

$$i_{\mathrm{ph}}(\tau) = k\left[\frac{2\beta_{12}}{h\nu_1}\langle P_1(t)P_2(t-\tau)\rangle + \frac{\beta_{11}}{2h\nu_1}\langle P_1^2(t)\rangle + \frac{\gamma_{222}}{3h\nu_2}\langle P_2^3(t-\tau)\rangle\right] \quad , \tag{5.4}$$

where γ_{222} is the degenerate 3PA coefficient. Unlike conventional 2PA cross-correlation, the signal-to-background ratio can exceed 3:1, depending on the 2PA and 3PA coefficients of the material and the signal and sampling powers used in the measurement. Recently, a similar background suppression technique has been applied for infrared photon counting [107].

5.5 Measurements of Two-Photon Absorption Photocurrent in a GaAs Photodiode

5.5.1 Background Photocurrent Measurement

For the measurements reported here, we used a commercially available GaAs PIN photodiode (Hamamatsu G8522-01), whose bandgap energy allows linear absorption at wavelengths shorter than 870 nm and degenerate 2PA at wavelengths shorter than 1740 nm. The signal and sampling wavelengths were chosen to be $\lambda_1 = 1490$ nm and $\lambda_2 = 1775$ nm, respectively. These wavelengths were chosen to satisfy the constraints in inequalities (5.3).

For the proof-of-concept measurements reported here, the signal and sampling pulse were co-generated as the signal and idler in a femtosecond optical parametric oscillator. The long wavelength sampling pulses could alternatively be produced using the soliton self-frequency shift in a highly nonlinear polarization-maintaining (PM) fiber [93, 108].

Both the signal and sampling pulses were 150 fs in duration, with a repetition rate of 82 MHz, and were focused to a 3.2 μm spot-size on the surface of the GaAs photodiode using an aspheric singlet lens. The photocurrent from the photodiode was measured using a lock-in detector. The background photocurrents (the latter two processes described in expression (5.4)), are quantified in Fig. 5.6, which shows the time-averaged photocurrent as a function of the average power at wavelengths of 1490 and 1775 nm.

The signal pulses at 1490 nm generate a photocurrent through degenerate two-photon absorption, as evidenced by the slope of 2 when plotted on logarithmic axes. The

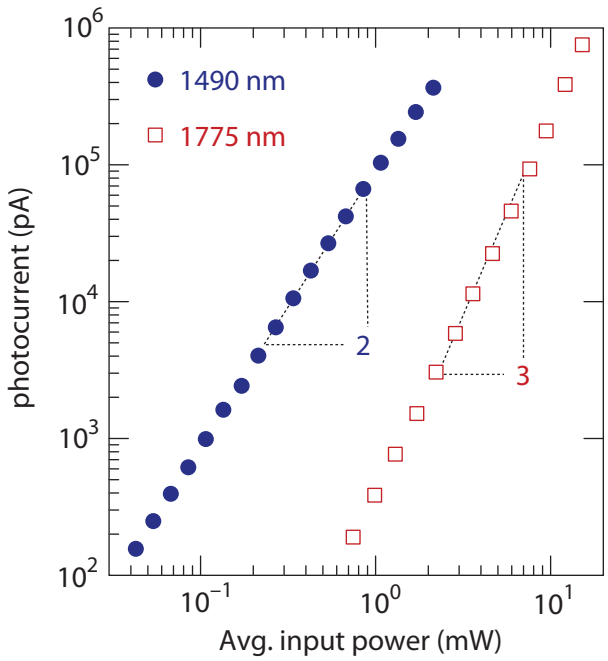

Figure 5.6: The background photocurrent as a function of incident power for $\lambda = 1490$ and 1775 nm.

sampling pulses at 1775 nm generate a photocurrent through three-photon absorption, which exhibits a cubic dependence in Fig. 5.6. The background photocurrent generated by 3PA from the sampling pulses is much smaller than the photocurrent generated by 2PA from the signal pulses at the same average input power used in the measurement. Notably, degenerate two-photon absorption of the sampling pulses does not occur because the sampling photon energy falls below the half-bandgap of GaAs.

5.5.2 Dynamic Range

Figure 5.7 plots the measured average photocurrent as a function of the signal power, with the sampling power held constant. The sampling pulses had an average power of 100 μW, which, in the absence of signal pulses, generated a background pho-

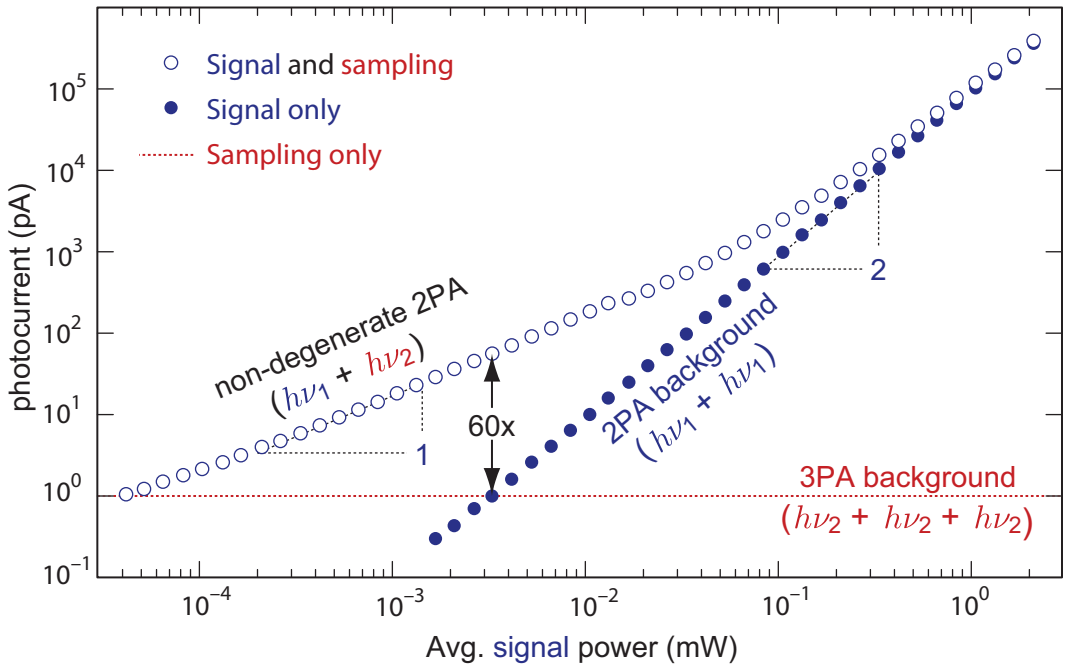

Figure 5.7: Measured average photocurrent in a GaAs photodiode vs. average signal power, for fixed sampling power of 100 μW.

tocurrent of 1 pA due to 3PA (indicated by the dashed line). When the sampling pulses were blocked, the degenerate 2PA photocurrent increased quadratically with the signal power, as expected. When both the sampling and signal pulses were spatially and temporally coincident on the detector, the photocurrent was linearly proportional to the signal power, as indicated by the open circles in Fig. 5.7. For a sampling power of 100 μW, the system achieved a maximum signal-to-background ratio of 30:1 at a signal power of 3 μW. Despite the large discrepancy between the signal and sampling powers, the system achieved a reasonable dynamic range by suppressing the background 2PA photocurrent of the sampling pulses.

5.5.3 Cross-Correlation Measurement

To demonstrate the improved dynamic range, we measured a cross-correlation between the signal and sample pulses by recording the time-averaged photocurrent as a function of the relative delay between the two. The solid curve in Fig. 5.8 plots the measured cross-correlation with a signal power of 3 μW and a sampling power of 100 μW. The cross-correlation full-width at half-maximum is measured to be 210 fs, as expected given the signal and sampling pulsewidths of 150 fs. The signal to background ratio is measured to be 30:1. The background photocurrent of 2 pA is composed of degenerate two-photon absorption of the signal pulses and three photon absorption of the sampling pulses, each of which generates 1 pA of average photocurrent. We emphasize that apart from choosing a sampling photon energy below the half bandgap, we did not employ any other techniques such as balanced detection or differential chopping to suppress the background.

For comparison, we note that if this measurement were performed using a sampling wavelength comparable to the signal wavelength (i.e., both above the half bandgap), then the attainable contrast ratio could never exceed 3:1. The dashed curve plotted in Fig. 5.8 shows the calculated cross-correlation signal that would result if the sampling frequency were tuned above the half-bandgap. When calculating the dashed curve, we reduced the sampling power to 45 μW, to account for the fact that the 2PA coefficient at 1490 nm was measured to be 2.2$\times$ higher than the coefficient describing non-degenerate 2PA of 1490 nm and 1775 nm, which is in agreement with the calculation of the non-degenerate and degenerate two-photon absorption coefficients by using second-order perturbation theory

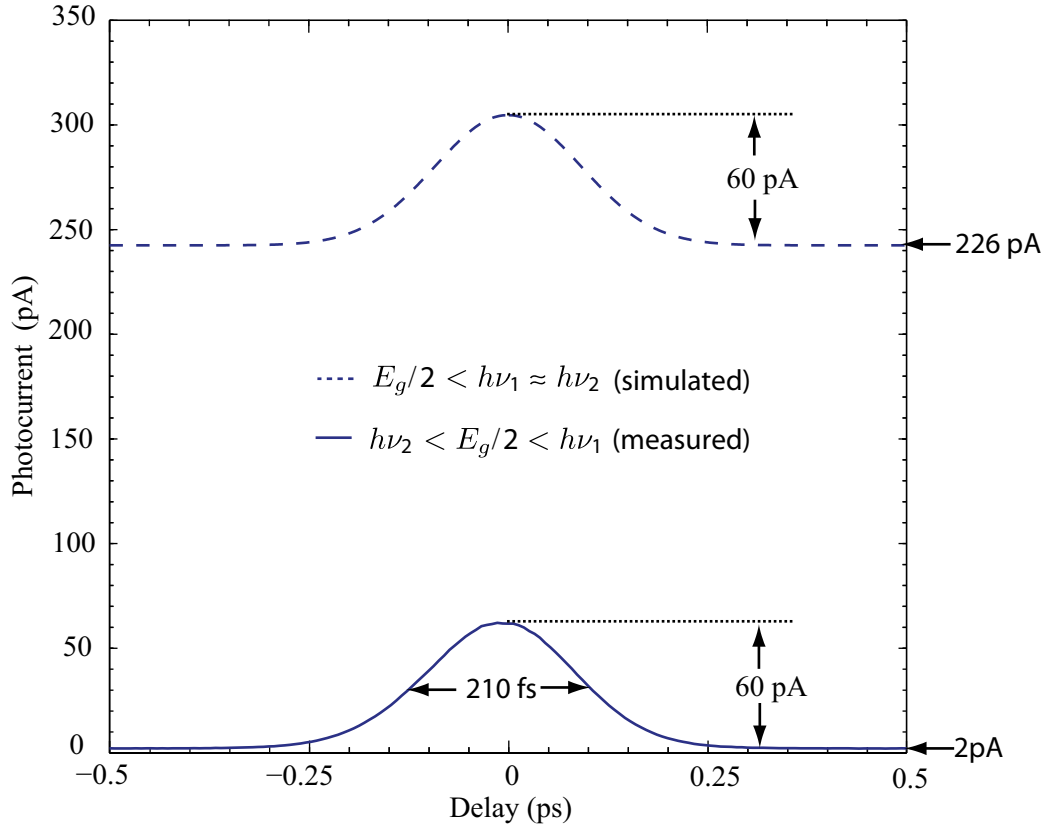

Figure 5.8: The cross-correlation between sampling and signal pulses. The solid line represents the measured cross-correlation when $h\nu_2 < E_g/2 < h\nu_1$. The dashed line is the simulated cross-correlation for the case when $E_g/2 < h\nu_2 \simeq h\nu_1$.

and a Kane band-structure model described in [109].

According to eq. (5.4), the signal-to background-ratio η can be described by

$$\eta = \frac{\frac{4\beta_{12}}{h(\nu_1+\nu_2)} P_1 P_2}{\frac{\beta_{11}}{2h\nu_1} P_1^2 + \frac{\gamma_{222}}{3h\nu_2} P_2^3} \quad . \tag{5.5}$$

While the non-degenerate 2PA signal scales in proportion to $P_1 P_2$, the background photocurrent from 3PA increases as P_2^3 and the degenerate 2PA of the signal grows as P_1^2. The largest value of η occurs when the signal and sampling pulses generate equal photocurrent. Under this condition,

$$P_1 = \sqrt{\frac{2\gamma_{222}\nu_1}{3\beta_{11}\nu_2} P_2^3} \quad . \tag{5.6}$$

Substituting P_1 from Eq. 5.6 into Eq. 5.5, the maximum signal-to-background ratio (or dynamic range) is found to be

$$\eta_{\max} = \frac{4\beta_{12}}{\nu_1+\nu_2} \sqrt{\frac{3\nu_1\nu_2}{2\beta_{11}\gamma_{222}P_2}} \quad . \tag{5.7}$$

Using these scaling relationships, the dynamic range is found to decrease with the sampling power in proportion to $P_2^{-1/2}$. To obtain the highest dynamic range, one should therefore choose the smallest possible sampling intensity for which the background photocurrents exceed the noise floor of the receiver.

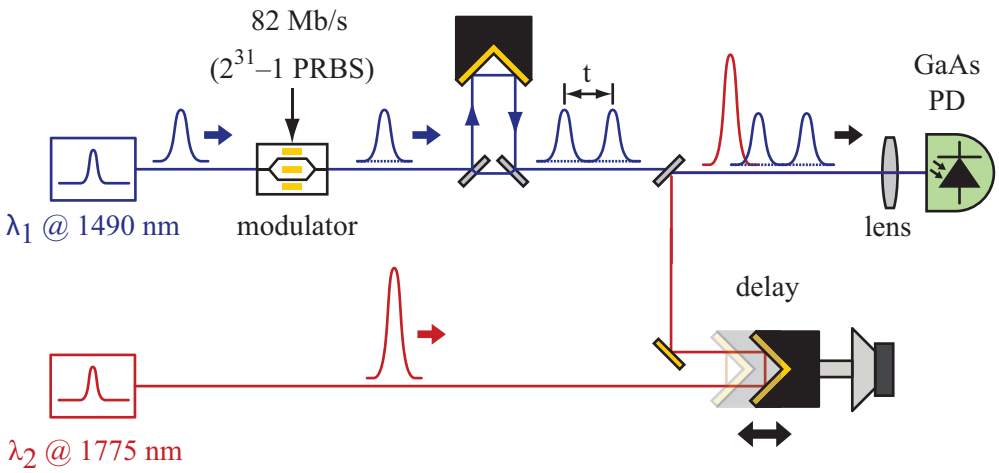

Figure 5.9: Experimental setup for an optical sampling using nondegenerate 2PA.

5.6 Ultrafast Optical Sampling in a GaAs Photodiode

Fig. 5.9 depicts the experimental setup used to demonstrate high-speed optical sampling based on nondegenerate 2PA [110]. The setup is similar to that used to measure the cross-correlation, except that the signal pulses were digitally modulated and passively multiplexed to simulate a high-speed time-division multiplexed channel. The signal pulses were on-off modulated with a $(2^{31} - 1)$, pseudorandom data pattern in a conventional lithium niobate waveguide electrooptic modulator. The signal pulsewidth broadened to 160 fs as a result of chromatic dispersion in the modulator and fiber pigtails. The resulting 82 Mb/s optical signal was split into two channels, one of which was delayed by $1/82$ μs (i.e., one bit period) in order to produce two uncorrelated tributaries. The two tributaries were recombined after adding an additional relative delay τ to simulate part of a high-speed optical-time-division-multiplexing (OTDM) data stream.

As before, the signal and sampling pulses were combined and focused onto the GaAs PIN photodiode. A retroreflector mounted on an audio speaker was used to vary the

relative timing between the signal and sampling pulses, while the resulting photocurrent was measured by directly connecting the photodiode to the 50 Ω input channel of a 4 GHz real-time digital oscilloscope. The photodiode has an electrical bandwidth of 3 GHz, which is sufficiently fast to resolve isolated sampling events. The oscilloscope waveform was collected at a (free-running) sample rate of 10 GS/s, over a time interval of 1 ms, but the resulting record was down-sampled to 82 MS/s (i.e., one measurement per sampling pulse) via offline post-processing.

Figure 5.10 shows measured eye diagrams for three inter-symbol spacings of $\tau =$ 250, 500, and 750 fs, which would be needed to support aggregate OTDM data rates of 4, 2, and 1.3 Tb/s. These measurements were performed using an average signal power of –2 dBm and a sampling power of +12 dBm. The black trace overlaid on Fig. 5.10(c) is the time-averaged cross-correlation signal, measured using a lock-in detector and slower variable delay. The cross-correlation shape closely matches the eye diagram, indicating that the temporal resolution of the sampling system is limited by the finite optical pulsewidths rather than by the electronics or nonlinearity. Notably, unlike in prior demonstrations, the eye diagrams do not exhibit a large background associated with degenerate 2PA of the pump signal.

5.7 Preliminary Experimental Results in a GaAs Waveguide-Based Detector

As mentioned previously, a smallest possible sampling intensity should be used in order to obtain the highest dynamic range. We expect the improvement in the dynamic

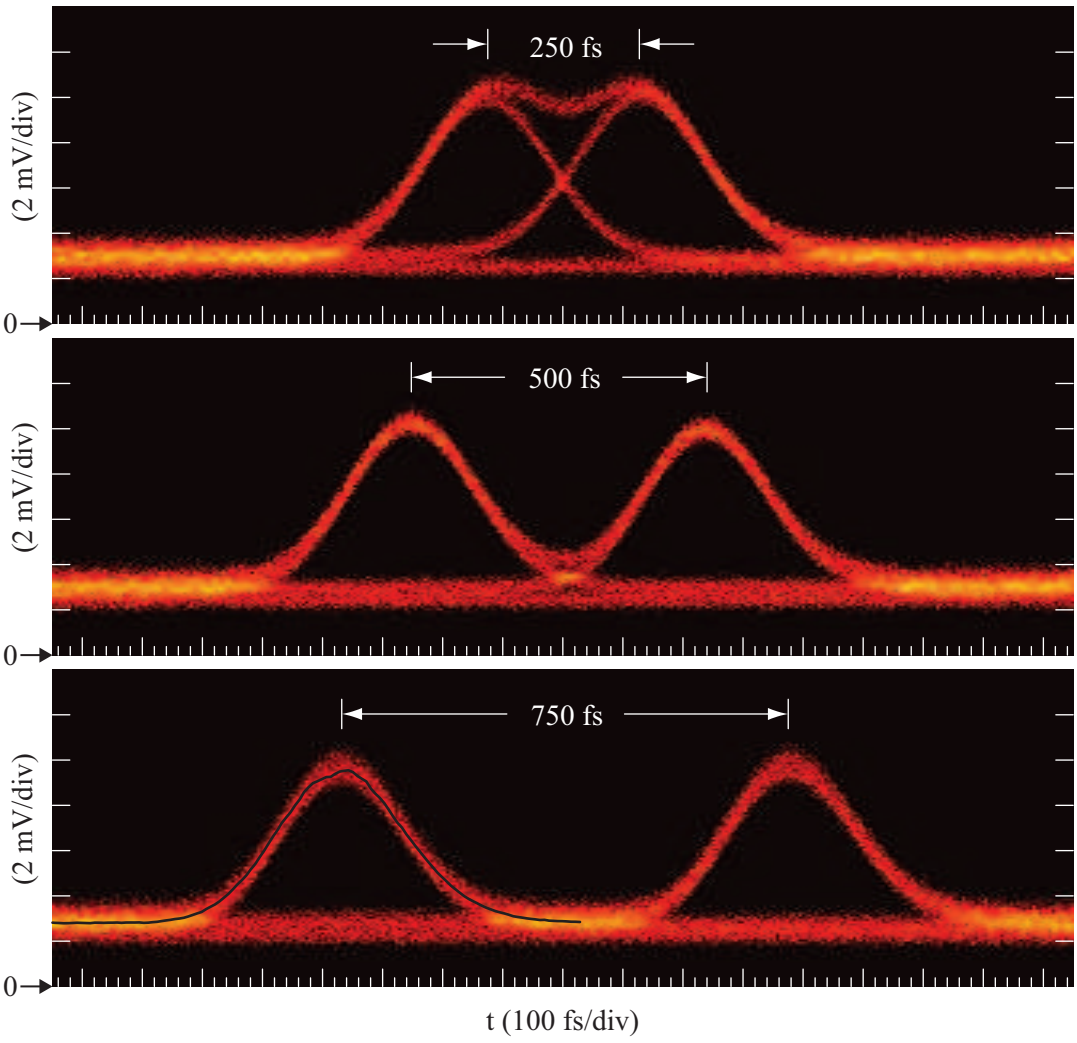

Figure 5.10: Measured eye diagram of an on-off keyed signal with inter-symbol spacings of 250, 500, and 750 fs.

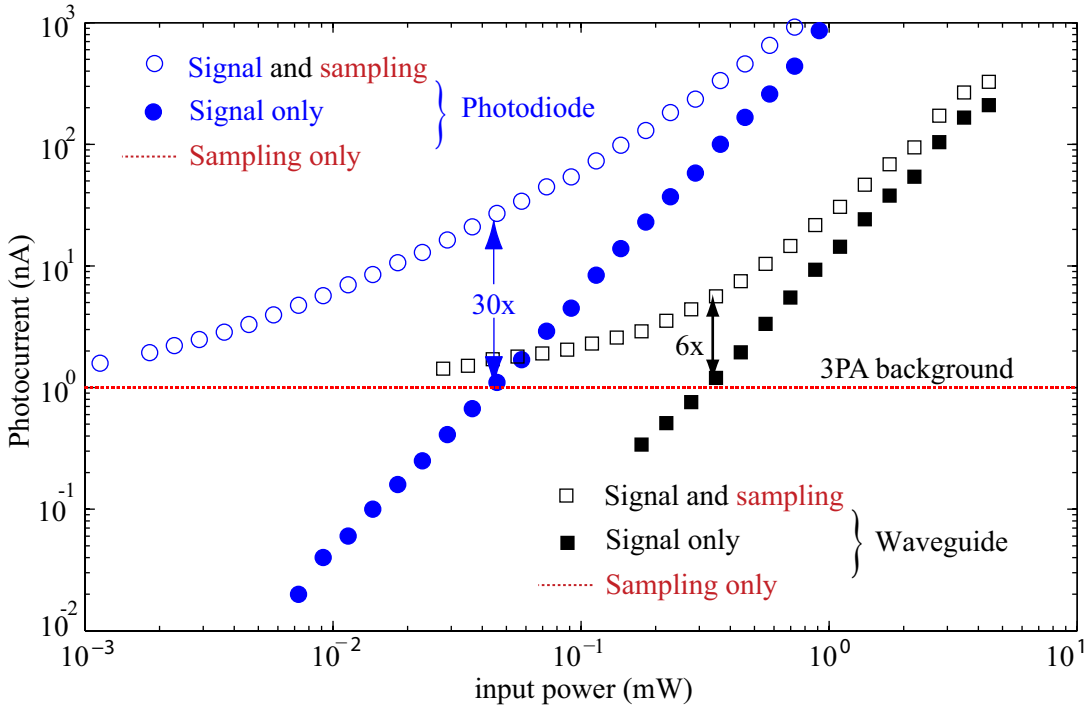

Figure 5.11: Measured average photocurrent in GaAs waveguide detector (square) and in GaAs photodiode (circle) vs. average signal power, for fixed sampling power

range and detection efficiency by using a waveguide-based detector, which benefits from a longer interaction length and a smaller mode size. To compare the performance of the optical sampling system using a GaAs waveguide detector to the system using a GaAs bulk photodiode, we repeated the measurement of average photocurrent as a function of the signal power for fixed sampling power. In this measurement, we use a 2.5-mm long GaAs waveguide-based detector which was described in chapter 3. The signal pulses at 1490 nm and the sampling pulses at 1775 nm were combined and coupled to the waveguide using a lensed fiber.

The open and closed squares in Fig. 5.11 represent the photocurrent generated in the waveguide as a function of signal power with and without the sampling pulses, respec-

tively. The sampling power was held constant and generated a background photocurrent of 1 nA due to 3PA, indicated by the dashed line. The system achieved a maximum signal-to-background ratio of 3:1, which is much lower than the ratio of 15:1 achieved in the photodiode conducted in similar measurement (circles in Fig. 5.11). One of the effects that limit the dynamic range in the waveguide detector is the walk-off between the pump pulse and the probe pulse due to waveguide dispersion. The walk-off length L_w represents the distance over which the pump and probe pulses pass through each other's envelope, and can be described by [111]

$$L_w = \frac{T_o}{\left| \frac{1}{v_{g_2}} - \frac{1}{vg_1} \right|} \quad , \tag{5.8}$$

where T_o is the pulse width of the pulse, and v_{g1} and v_{g2} are the group velocities at the signal and sampling wavelengths, respectively. v_{g1} and v_{g2} can be determined by numerically calculating the effective refractive index of the waveguide using a mode solver [112] taking into account the GaAs material dispersion described in [113]. For the signal pulses at 1490 nm and the sampling pulses at 1775 nm, v_{g1} and v_{g2} are estimated to be 8.91×10^7 m/s and 8.94×10^7 m/s, respectively. For a signal with a pulsewidth of 160 fs, the walk-off length L_w is estimated to be 1.8 mm, which is shorter than the waveguide length. Therefore, the group-delay walk-off in the waveguide has a role in limiting the dynamic range of the sampling system. The dynamic range and detection efficiency can also be limited by coupling and propagation loss, material quality and the size mismatch between the

optical modes of the waveguide at the pump and probe wavelengths.

5.8 Summary

We demonstrated a high-speed optical sampling system based on non-degenerate two-photon absorption in a GaAs photodetector. By using long-wavelength sampling pulses below the half-bandgap of the detector, we effectively suppressed the otherwise large background current that has historically plagued 2PA-based sampling systems. We measured eye diagrams for pseudorandom optical data signals, and showed a temporal resolution sufficient for speeds as high as 4 TB/s, limited primarily by the optical pulsewidth. The dynamic range of the sampling system that used a waveguide-based detector is lower than that of the sampling system that used a GaAs bulk photodiode, and it could be explained by the group-delay walk-off, coupling and propagation loss, material quality and the size mismatch between the optical modes of the waveguide at the pump and probe wavelengths.

Chapter 6

Conclusions

6.1 Summary

This thesis has sought to investigate nonlinear effects in semiconductor waveguides for optical signal processing. This work includes the characterization, design, fabrication and measurement of nonlinear waveguides.

In this work, I developed a technique to characterize nonlinear properties including two-photon absorption, self-phase modulation, free-carrier absorption, free-carrier dispersion and free-carrier lifetime in semiconductor waveguides. First, I developed the simulation tools using the split-step Fourier method to simulate nonlinear pulse propagation in the optical waveguide. Then, nonlinear properties were determined by launching femtosecond pulses into the waveguides and measuring the output power and output spectrum as a function of the input power along with measuring pump-probe transient absorption. By matching these measurements against numerical simulations, I estimated the nonlinear coefficients describing these nonlinear effects in the waveguide.

I reported the first experimental measurement of the instantaneous and carrier-based nonlinear effects in porous silicon waveguides at 1550 nm. Although the waveguide was approximately 70% porous, it exhibited instantaneous nonlinear effects including self-phase modulation and two-photon absorption comparable to those of crystalline silicon waveguides. The carrier-based nonlinearities are stronger and faster in porous silicon,

compared to what has been reported for crystalline silicon.

The fabrication of semiconductor waveguides can be a challenging task. There is always a trade-off between propagation loss and optical confinement. To this end, I designed and fabricated bulk GaAs waveguides with and without electrical contacts. 10-Gb/s wavelength conversion was demonstrated using nonlinear effects including cross-amplitude modulation (XAM), cross-phase modulation (XPM) and four-wave mixing (FWM) in these GaAs waveguides. The bit-error rate (BER) receiver sensitivity was measured, for the first time, in GaAa/AlGaAs waveguides. Both XPM and FWM based wavelength conversions exhibited BER receiver sensitivity penalties of less than 1 dB relative to the baseline signal.

Finally, I demonstrated an ultrafast optical sampling system based on non-degenerate two-photon absorption in a GaAs photodiode. By choosing the sampling pulses to have a photon energy below the half-bandgap of GaAs, the photocurrent background associated with nonlinear absorption of the strong sampling pulses was suppressed. The system is capable of resolving a quasi- 4 Tb/s signal with low background photocurrent.

6.2 Future Work

Our study on the nonlinear optical properties of porous silicon waveguides suggests that porous silicon could be an interesting alternative for all-optical switching or fast electrooptic modulators. However, before making a modulator, more work is needed to investigate the electrical conductivity in the directions parallel and perpendicular to the surface of a porous silicon waveguide. Laser-induced oxidation in porous silicon deserves

further investigation. A better understanding of how to define the refractive index profile of the porous silicon waveguide could further improve the process for making a porous silicon waveguide with a small effective area and low propagation loss.

Having demonstrated, for the first time, 10-Gb/s wavelength conversion using nonlinear effects in GaAs waveguides, the next step is to improve the nonlinear efficiency in the waveguides. As previously mentioned, nonlinear effects such as XPM and FWM are hindered by 2PA in GaAs waveguides. This problem can be solved by using AlGaAs, the bandgap energy of which can be designed to suppress the effects of 2PA in 1550 nm spectral regime. Figure 6.1 depicts the simulated bandgap wavelength and the refractive index of $Al_xGa_{1-x}As$ as a function of the Al fraction x [113]. According to the simulation in Fig. 6.1, AlGaAs with an Al fraction of 0.13 or more has a bandgap wavelength lower than 775 nm, which is enough to suppress 2PA from the optical signal operated at 1550 nm since the signal photon energy falls below half the bandgap.

Several groups have reported the fabrication of AlGaAs nanowires [21, 70], but the performance of these nanowires is impeded by propagation loss, which can be as high as 80 dB/cm. The majority of the propagation loss in the high-index contrast waveguide is attributed to the sidewall roughness. There are two potential solutions to minimize the overlap of the optical mode with the waveguide sidewalls in order to reduce the scattering loss from sidewall roughness. The first solution is to fabricate a waveguide without any etching process. Figure 6.2 depicts the fabrication process based on the submicron thick GaAs/AlGaAs waveguide demonstrated in [22]. Here, we replace the GaAs quantum wells in [22] with an $Al_{0.2}Ga_{0.8}As$ core layer. The core layer is grown on an etch stop layer made of AlAs on the GaAs substrate. There is a thin GaAs buffer layer be-

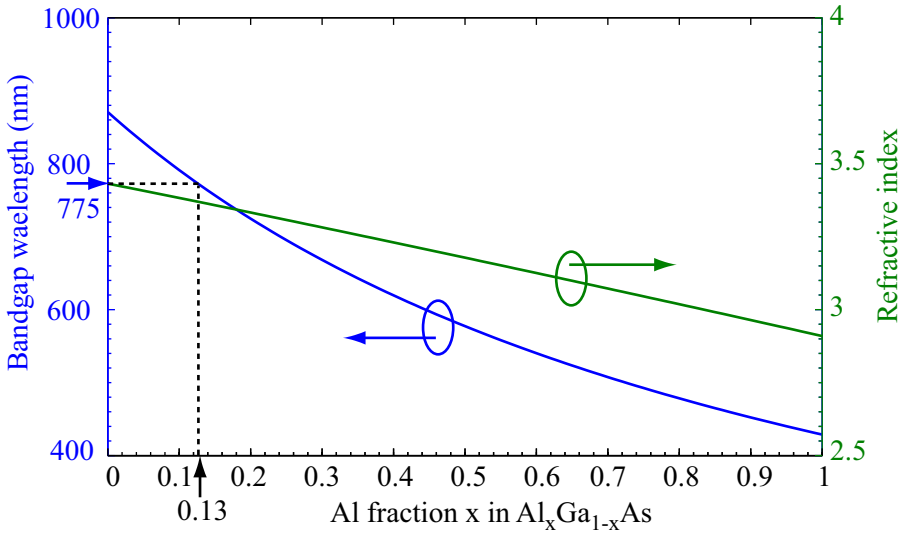

Figure 6.1: The bandgap wavelength and the refractive index of $Al_xGa_{1-x}As$ as a function of Al fraction x

tween the $Al_{0.2}Ga_{0.8}As$ core layer and the AlAs etch stop layer to protect the core layer from selective etching when the AlAs etch stop is removed. First, 60-nm thick Si is deposited on the photoresist patterned by e-beam lithography. The patterns are then lifted off. The lifted off Si layer provides the index loading for the AlGaAs waveguide. Then, BCB is spun on the sample for planarization. The sample is then bonded upside down to another semi-insulating GaAs transfer substrate using BCB as a bonding layer. Finally, the substrate is removed along with the AlAs etch stop layer and the GaAs buffer layer as described in [114]. The fundamental TE mode contours that were superposed on the schematic waveguide structure in Fig. 6.2(d) is numerically calculated with the effective area estimated to be 0.37 μm^2.

Recently, low-loss etchless silicon waveguides defined by thermal oxidation (which produces smooth sidewalls) have been demonstrated [115]. This technique could poten-

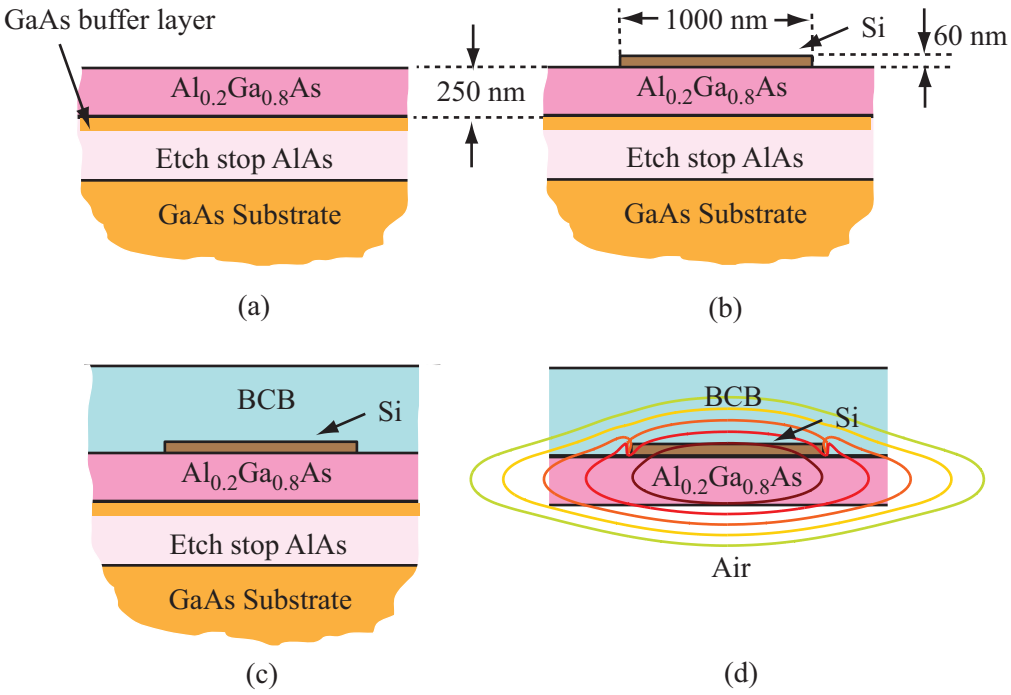

Figure 6.2: Fabrication process for AlGaAs substrate removed waveguides with Si index loading layer.

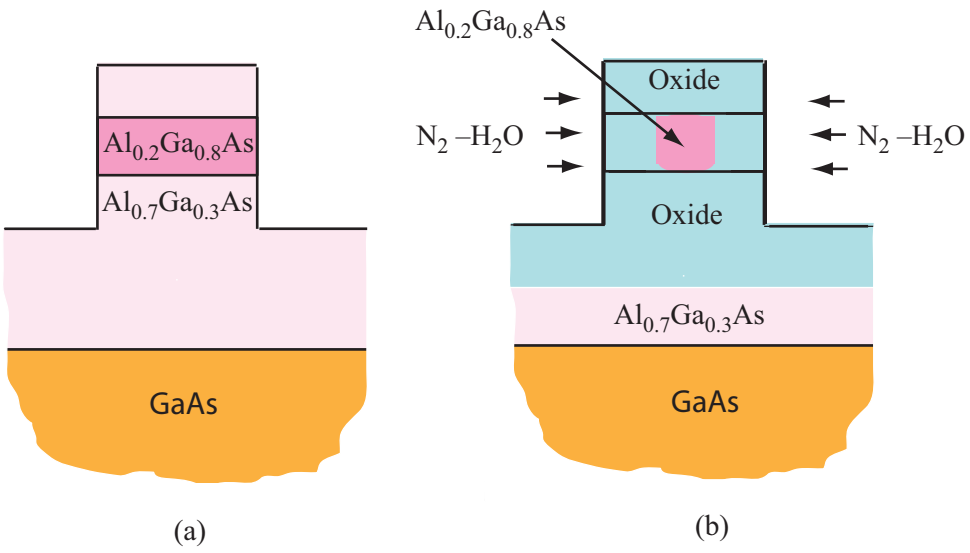

Figure 6.3: Fabrication process for AlGaAs waveguides defined by lateral oxidation

tially be applied to AlGaAs waveguides. The oxidation rate of AlGaAs increases with the increase in the fraction of Al in AlGaAs layer. This selective oxidation has been used to form a current aperture in GaAs/AlGaAs vertical-cavity surface-emitting lasers (VCSELs) [116]. Figure 6.3 depicts the fabrication process for AlGaAs waveguides defined by lateral oxidation. The structure consists of an $Al_{0.2}Ga_{0.8}As$ core layer surrounded by $Al_{0.7}Ga_{0.3}As$ cladding layers on a GaAs substrate. First, the ridge waveguide is formed by ICP etching, as described in Chapter 3. Then, the AlGaAs waveguide is laterally oxidized. Since the cladding layers are oxidized at the faster rate than the core layer due to the much larger Al fraction in the cladding layers, the $Al_{0.2}Ga_{0.8}As$ core layer is surrounded by oxide layers as illustrated in Fig. 6.3(b). Low-loss and compact AlGaAs waveguides fabricated by these two techniques could potentially be used for nonlinear optical signal processing.

Finally, we reported a proof-of-concept measurements of optical sampling system

in which both the signal and sampling pulse were co-generated as the signal and idler in an optical parametric oscillator. Due to equipment availability limitations, we were not be able to do the same measurement in a high-speed OTDM system. The polarization dependence of this optical sampling system deserves further investigation. Our group has demonstrated polarization-insensitive optical clock recovery using 2PA in a silicon photodiode [117]. By choosing the polarization state of the clock to be circular, the cross-correlation component becomes independent of the polarization state of the data. This technique could be applied in an optical sampling system using a GaAs photodiode by fixing the polarization state of the sampling pulses to be circular. The system sensitivity could also be improved by using a waveguide-based detector instead of a p-i-n photodetector. A better waveguide design is needed to optimize or control the dispersion properties in the waveguide. Nonetheless, ultrafast two-photon absorption in a GaAs photodiode with the background suppression technique can potentially be used for all other optical signal processing applications including optical demultiplexing.

Appendix A

Correction Factor for Two-Photon Absorption Measurements in Semiconductor Waveguides Using the Inverse Transmission Technique

The inverse transmission technique has been commonly employed for measuring the two-photon absorption coefficient in semiconductor waveguides. The 2PA coefficient can be obtained directly by launching optical pulses into a waveguide and measuring the slope of the ratio of the input intensity to the transmitted intensity (the reciprocal of intensity transmission) as a function of the input intensity. For a waveguide with linear propagation loss α and two-photon absorption coefficient β_{2PA}, the intensity of the optical pulses propagating along the waveguide at distance z and at time t can be described as

$$\frac{\partial I(z,t)}{\partial z} = -\alpha I(z,t) - \beta_{2PA} I(z,t)^2. \tag{A.1}$$

This equation can be directly integrated to obtain a solution for the intensity transmitted through a waveguide of length L as

$$I(L,t) = \frac{I(0,t)e^{-\alpha L}}{1+\beta_{2PA} L_{eff} I(0,t)}, \tag{A.2}$$

where L_{eff} is defined as $(1-e^{-\alpha L})/\alpha$. For optical pulses with a peak input intensity of I_o, the ratio of the peak intensity of input to transmitted pulses can be described as

$$\frac{1}{T_I} = e^{\alpha L}[1+\beta_{2PA} L_{eff} I_o]. \tag{A.3}$$

β_{2PA} can be found from the slope of the reciprocal of the peak intensity transmission

$1/T_{\mathrm{I}}$ as a function of peak input intensity. Usually, the peak intensities of the input and transmitted pulses are estimated by measuring the average optical powers before and after the waveguide [50, 73, 74]. However, the estimate of peak intensity of the transmitted pulses is accurate only if the temporal profile of the transmitted pulses remains the same after propagation through the waveguide. We demonstrated in chapter 2 that the output spectrum could broaden and shift as a result of self-phase modulation and free-carrier dispersion. Even without these effects, the temporal profile of optical pulses can change as a result of 2PA-induced pulsewidth spreading. To better understand this effect, let's assume that a hyperbolic secant pulse with a peak input intensity I_{o} and a pulsewidth t_{o} is launched into the waveguide. The temporal intensity profile of the input pulse can be written as

$$I(0,t) = I_{\mathrm{o}}\mathrm{sech}^2(\frac{t}{t_{\mathrm{o}}}). \tag{A.4}$$

The average power of the input pulse can be written as

$$P_{1_{\mathrm{ave}}} = A_{\mathrm{eff}}\int_{-\infty}^{\infty} I(0,t)dt = 2t_{\mathrm{o}}I_{\mathrm{o}}A_{\mathrm{eff}}, \tag{A.5}$$

where A_{eff} is the effective area of the waveguide. By substituting the input intensity from Eq.(A.4) into Eq.(A.2), the output intensity can be written as

$$I(L,t) = \frac{I_{\mathrm{o}}\mathrm{sech}^2(\frac{t}{t_{\mathrm{o}}})e^{-\alpha L}}{1+\beta_{2\mathrm{PA}}L_{\mathrm{eff}}I_{\mathrm{o}}\mathrm{sech}^2(\frac{t}{t_{\mathrm{o}}})}. \tag{A.6}$$

As a result, the average output power $P_{2_{\mathrm{ave}}} = A_{\mathrm{eff}}\int_{-\infty}^{\infty} I(L,t)dt$ can be derived as

$$P_{2_{\mathrm{ave}}} = 2t_{\mathrm{o}}I_{2\mathrm{o}}A_{\mathrm{eff}}\frac{(\beta_{2\mathrm{PA}}L_{\mathrm{eff}}I_{\mathrm{o}}+1)^{1/2}}{(\beta_{2\mathrm{PA}}L_{\mathrm{eff}}I_{\mathrm{o}})^{1/2}}\ln[(\beta_{2\mathrm{PA}}L_{\mathrm{eff}}I_{\mathrm{o}}+1)^{1/2}+(\beta_{2\mathrm{PA}}L_{\mathrm{eff}}I_{\mathrm{o}})^{1/2}], \tag{A.7}$$

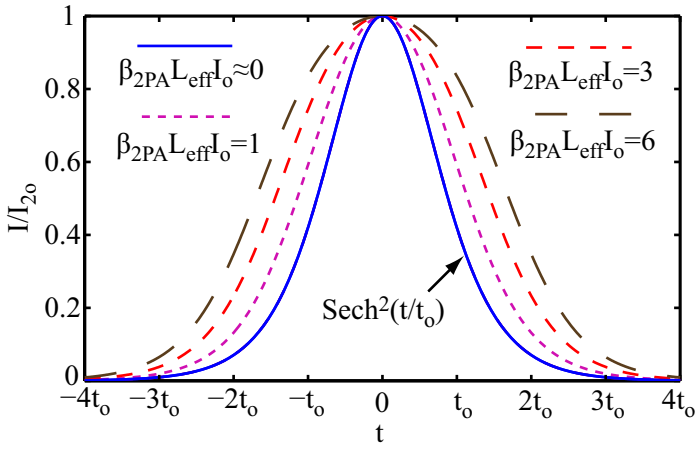

Figure A.1: Simulated temporal profile of the transmitted pulse at different input intensities.

where $I_{2o} = I_o \exp(-\alpha L)/(1+\beta_{2PA} L_{eff} I_o)$ is the peak intensity of the transmitted pulses at the output of the waveguide. Figure A.1 shows the simulation of the normalized temporal intensity profile of hyperbolic secant pulses transmitted through the waveguide at different peak input intensities. The temporal profile of the transmitted pulses changes as the input intensity increases as a result of 2PA-induced pulsewidth spreading.

From Eq.(A.5) and Eq.(A.7), the reciprocal of the power transmission $1/T_P$ (which is the ratio of input to transmitted power) can be derived as

$$\frac{1}{T_P} = \frac{P_{1_{ave}}}{P_{2_{ave}}} = \frac{e^{\alpha L}(\beta_{2PA} L_{eff} I_0 + 1)^{1/2}(\beta_{2PA} L_{eff} I_0)^{1/2}}{\ln[(\beta_{2PA} L_{eff} I_0 + 1)^{1/2} + (\beta_{2PA} L_{eff} I_0)^{1/2}]}. \tag{A.8}$$

Equation (A.8) shows that the 2PA coefficient cannot be determined directly from the slope of the ratio of the input to transmitted power as a function of input intensity. To verify the result of this equation, we measured the ratio of input to transmitted power as a function of input intensity in a silicon-on-insulator (SOI) waveguide. 200-fs optical pulses with a 82 MHz repetition rate at the center wavelength of 1550 nm were launched

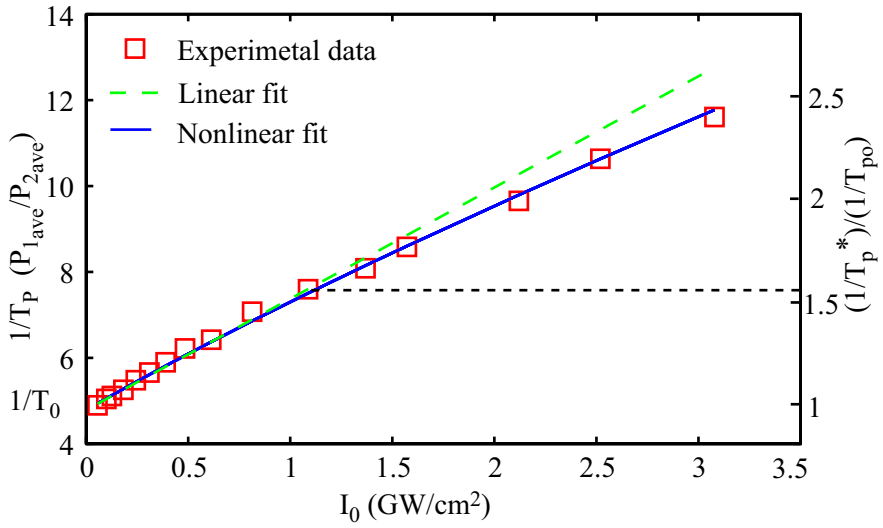

Figure A.2: The ratio of input to transmitted power as a function of input intensity (squares: experimental data; dashed line: linear fitting; solid line: simulation derived in Eq.(A.8)).

into the SOI waveguide. The waveguide was 1.7 cm long and had an effective area of 10 μm^2. Fig. A.2 presents the experimental and simulated ratio of input to transmitted power as a function of peak input intensity. As expected, the measured data deviate from the linear fit, while the simulation obtained by numerically solving Eq.(A.8) gives excellent agreement with the observations. From the simulation, β_{2PA} is estimated to be $1\pm.25$ cm/GW, in agreement with what we measured in chapter 2. This estimated value is higher than the value of $0.63\pm.15$ cm/GW estimated by the slope of linear fit line by a factor of 1.6.

The disparity in estimating 2PA coefficient by the inverse transmission technique has been considered in [76]. Here, we propose a simple technique to correct the value of β_{2PA} estimated from the slope of the linear fit by introducing the 2PA correction factor Γ. The 2PA correction factor is defined as the ratio of β_{2PA} estimated by solving Eq.(A.8) to

β_{2PA} estimated from the slope of the linear fit. Based on the definition of Γ, Eq.(A.8) can be rearranged as

$$\frac{1}{T_P} \simeq e^{\alpha L}[1 + \frac{\beta_{2PA}}{\Gamma} L_{eff} I_0]. \tag{A.9}$$

Γ depends on the temporal profile and peak intensity of the input pulses. For low input intensity, Γ can be written as

$$\lim_{I_0 \to 0} \Gamma = \frac{g(0) \int_{-\infty}^{\infty} g(t) dt}{\int_{-\infty}^{\infty} g^2(t) dt}, \tag{A.10}$$

where g(t) is the temporal profile of the input pulses. For low input intensity, Γ is 1 for CW or square pulses, while Γ is $\sqrt{2}$, 1.5 and 1.33 for Gaussian, hyperbolic secant and raised cosine pulses, respectively. This means that even at low input intensity, the value of β_{2PA} measured from the slope of the reciprocal of the transmission is underestimated at least by the factor of $\sqrt{2}$ for Gaussian pulses.

For the inverse transmission measurement in GaAs waveguide depicted in Fig. 3.8 in chapter 3, β_{2PA} was measured to be 10.6 cm/GW from the slope of the reciprocal of the transmission. In this measurement, the measured data do not deviate from the linear fit. In this case, we can use the minimum correction factor of $\sqrt{2}$ for Gaussian pulses. After taking into account the correction factor, β_{2PA} is calculated to be 15 cm/GW.

For higher input intensity, the reciprocal of the transmission (the ratio of input to transmitted power) deviates from the linear fit as a result of 2PA-induced pulsewidth spreading. The slope of the reciprocal of the transmission varies at each point along the curve. We define the inverse transmission evaluation point $1/T_P^*$ as the inverse trans-

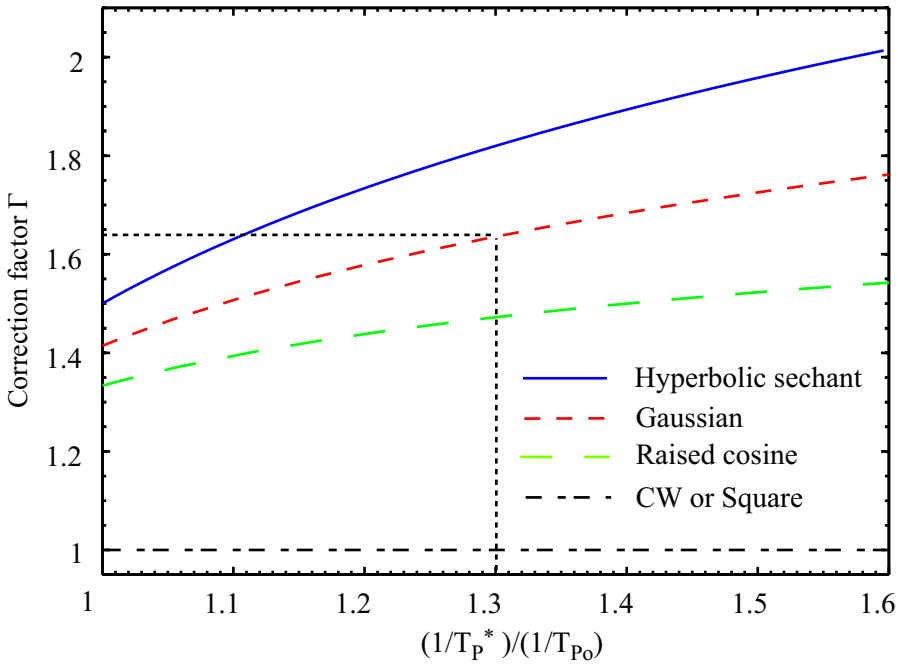

Figure A.3: Correction factor as a function of the normalized inverse transmission evaluation point for more common pulse profiles.

mission, at which the linear fit is the tangent line of the measured data curve. Γ can be calculated numerically as a function of normalized inverse transmission evaluation point $(1/T_P^*)/(1/T_{Po})$, where $1/T_{Po}$ is the Y-intercept of the linear fit. Figure A.3 shows Γ as a function of normalized inverse transmission evaluation point for the more common pulse profiles. For the inverse transmission measurement in Fig. A.2, the normalized inverse transmission evaluation point is found to be 1.3. Assuming that the input pulses have a Gaussian temporal profile, Γ can be determined from the plot in Fig. A.3 and is found to be 1.64, in agreement with the ratio of 1.6 calculated from the measurement.

Table A.1 lists published values of 2PA coefficient of silicon measured in the 1550 nm wavelength regime. The values of β_{2PA} measured by inverse transmission technique are lower than those measured by other techniques. By taking into account the correction

β_{2PA}published (cm/GW)	β_{2PA}correction (cm/GW)	λ (nm)	Ref.	Method
0.44±.1	0.78±.18	1560	[73]	1/T
0.45±.1	0.81±.18	1536	[50]	1/T
0.67±.07	0.94±.1	1550	[74]	1/T
0.79±.12	-	1540	[17]	z-scan
0.9±.18	-	1540	[32]	fit to T
0.63±.15	1±.25	1550	this work	1/T

Table A.1: Published values of 2PA coefficient of silicon with and without employing correction factor.

factor Γ to determine the 2PA coefficient measured by the inverse transmission technique, the values of 2PA coefficient become more consistent with those measured by other methods.

Bibliography

[1] T. Suhara and M. Fujimura. *Waveguide Nonlinear-Optic Devices*. Springer, first edition, 2003.

[2] C. Langrock, S. Kumar, J. E. McGeehan, A. E. Willner, and M. M. Fejer. All-optical signal processing using $\chi^{(2)}$ nonlinearities in guided-wave devices. *J. Lightwave Technol.*, 24(7):2579–2592, 2006.

[3] K. E. Stubkjaer. Semiconductor optical amplifier-based all-optical gates for high-speed optical processing. *J. Select. Topics in Quantum. Electron.*, 6(6):1428–1435, 2000.

[4] R. Salem, A. S. Lenihan, G. M. Carter, and T. E. Murphy. 160 Gb/s polarization-independent optical demultiplexing in 2-m Bismuth-Oxide fiber. *IEEE Photon. Technol. Lett.*, 18(21):2245–2247, 2006.

[5] J. Hansryd, P. A. Andrekson, M. Westlund, J. Li, and P.-O. Hedekvist. Fiber-based optical parametric amplifiers and their applications. *J. Select. Topics in Quantum. Electron.*, 8(3):506–520, 2002.

[6] C. Koos, P. Vorreau, P. Dumon, R. Baets, B. Esembeson, I. Biaggio, T. Michinobu, F. Diederich, W. Freude, and J. Leuthold. Highly-nonlinear silicon photonics slot waveguide. *Proc. Opt. Fiber Commun. Conf.*, (PDP25) 2008.

[7] C. Koos, P. Vorreau, T. Vallaitis, P. Dumon, W. Bogaerts, R. Baets, B. Esembeson, I. Biaggio, T. Michinobu, F. Diederich, W. Freude, and J. Leuthold. All-optical high-speed signal processing with silicon-organic hybrid slot waveguides. *Nature Photonics*, 3:216–219, 2009.

[8] V. G. Táeed, M. R. E. Lamont, D. J. Moss, B. J. Eggleton, D.-Y. Choi, S. Madden, and B. Luther-Davies. All optical wavelength conversion via cross phase modulation in chalcogenide glass rib waveguides. *Opt. Express*, 14(23):11242–11247, 2006.

[9] M. Galili, J. Xu, H. C. H. Mulvad, L. K. Oxenlowe, A. T. Clausen, P. Jeppesen, B. Luther-Davies, S. Madden, A. Rode, D.-Y. Choi, M. Pelusi, F. Luan, and B. J. Eggleton. Breakthrough switching speed with an all-optical chalcogenide glass chip: 640 Gbit/s demultiplexing. *Opt. Express*, 17(4):2182–2187, 2009.

[10] R. Dekker, N. Usechak, M. Först, and A. Driessen. Ultrafast nonlinear all-optical processes in silicon-on-insulator waveguides. *J. Phys. D: Appl. Phys.*, 40:R249–R271, 2007.

[11] R. Salem, M. A. Foster, A. C. Turner, D. F. Geraghty, M. Lipson, and A. L. Gaeta. Signal regeneration using low-power four-wave mixing on silicon chip. *Nature Photonics*, 2:35–38, 2008.

[12] V. Van, T. A. Ibrahim, P. P. Absil, F. G. Johnson, R. Grover, and P.-T. Ho. Optical signal processing using nonlinear semiconductor microring resonators. *J. Select. Topics in Quantum. Electron.*, 8(3):705–713, 2002.

[13] A. Villeneuve, K. AI-Hemyari, J. U. Kang, C. N. Ironside, J. S. Aitchison, and G. I. Stegeman. Demonstration of all-optical demultiplexing at 1555 nm with an AlGaAs directional coupler. *Electron. Lett.*, 19(8):721–722, 1993.

[14] F. Z. Henari, K. Morgenstern, W. J. Blau, V. A. Karavanskii, and V. S. Dneprovskii. Third-order optical nonlinearity and all-optical switching in porous silicon. *Appl. Phys. Lett.*, 67:323–325, 1995.

[15] F. Z. Henari. Two photon absorption of porous silicon. *Laser Physics*, 15:1634–1636, 2005.

[16] S. Lettieri, O. Fiore, P. Maddalena, D. Ninno, G. D. Francia, and V. L. Ferrara. Nonlinear optical refraction of free-standing porous silicon layers. *Opt. Commun.*, 168:383–391, 1999.

[17] M. Dinu, F. Quochi, and H. Garcia. Third-order nonlinearities in silicon at telecom wavelengths. *Appl. Phys. Lett.*, 82:2954–2956, 2003.

[18] A. Villeneuve, C. C. Yang, G. I. Stegeman, C. N. Ironside, G. Scelsi, and R. M. Osgood. Nonlinear absorption in a GaAs waveguide just above half the band gap. *J. Quantum Electron*, 30(5):1172–1175, 1994.

[19] P. P. Absil, J. V. Hryniewicz, B. E. Little, P. S. Cho, R. A. Wilson, L. G. Joneckis, and P.-T. Ho. Wavelength conversion in GaAs micro-ring resonators. *Optics Lett.*, 25(8):554–556, 2000.

[20] C. Husko, A. D. Rossi, S. Combrié, Q. V. Tran, F. Raineri, and C. W. Wong. Ultrafast all-optical modulation in GaAs photonic crystal cavities. *Appl. Phys. Lett.*, 94:021111, 2009.

[21] G. A. Siviloglou, S. Suntsov, R. El-Ganainy, R. Iwanow, G. I. Stegeman, and D. N. Christodoulides. Enhanced third-order nonlinear effects in optical AlGaAs nanowires. *Opt. Express*, 14(20):9377–9384, 2006.

[22] J. Shin, Y.-C. Chang, and N. Dagli. Propagation loss study of very compact GaAs/AlGaAs substrate removed waveguides. *Opt. Express*, 17(5):3390–3395, 2009.

[23] H. F. Arrand, T. M. Benson, P. Sewell, A. Loni, R. J. Bozeat, R. Arens-Fischer, M. Krüger, M. Thönissen, and H. Lüth. The applications of porous silicon to optical waveguiding technology. *IEEE J. Sel. Top. Quantum Electron.*, 4:975–982, 1998.

[24] H. F. Arrand, T. M. Benson, A. Loni, M. G. Krüger, M. Thönissen, and H. Lüth. Self-aligned porous silicon optical waveguides. *Electron. Lett.*, 33:1724–1725, 1997.

[25] A. Loni, L. T. Canham, M. G. Berger, R. Arens-Fischer, H. Munder, H. Lüth, H. F. Arrand, and T. M. Benson. Porous silicon multilayer optical waveguides. *Thin Solid Films*, 276:143–146, 1996.

[26] B. Gelloz and N. Koshida. Electroluminescence with high and stable quantum efficiency and low threshold voltage from anodically oxidized thin porous silicon diode. *J. Appl. Phys.*, 88:4319–4324, 2000.

[27] J. P. Zheng, K. L. Jiao, W. P. Shen, W. A. Anderson, and H. S. Kwok. Electroluminescence with high and stable quantum efficiency and low threshold voltage from anodically oxidized thin porous silicon diode. *J. Appl. Phys.*, 61:459–461, 1992.

[28] G. Vincent. Optical properties of porous silicon superlattices. *Appl. Phys. Lett.*, 64:2367–2369, 1994.

[29] L. Pavesi. Porous silicon dielectric multilayers and microcavities. *Riv. Nuovo Cimento*, 20:1–76, 1997.

[30] H. F. Arrand, T. M. Benson, A. Loni, R. Arens-Fischer, M. Krüger, M. Thönissen, H. Lüth, and S. Kershaw. Novel liquid sensor based on porous silicon optical waveguides. *IEEE Photon. Technol. Lett.*, 10:1467–1469, 1998.

[31] T. Matsumoto, M. Daimon, H. Mimura, Y. Kanemitsu, and N. Koshida. Optically induced absorption in porous silicon and its application to logic gates. *J. Electrochem. Soc.*, 142:3528–3533, 1995.

[32] G. W. Rieger, K. S. Virk, and J. F. Young. Nonlinear propagation of ultrafast 1.5 μm pulses in high-index-contrast silicon-on-insulator waveguides. *Appl. Phys. Lett.*, 84(5):900–902, 2004.

[33] L. Yin and G. P. Agrawal. Impact of two-photon absorption on self-phase modulation in silicon waveguides. *Optics Lett.*, 32(5):2031–2033, 2007.

[34] R. A. Soref and B. R. Bennett. Electrooptical effects in silicon. *IEEE J. Quantum Electron.*, QE-23:123–129, 1987.

[35] A. Cutolo, M. Iodice, P. Spirito, and L. Zeni. Silicon electro-optic modulator based on a three terminal device integrated in a low-loss single-mode SOI waveguide. *J. Lightwave Technol.*, 15(5):505–518, 1997.

[36] I. D. Rukhlenko, M. Premaratne, C. Dissanayake, and G. P. Agrawal. Nonlinear pulse evolution in silicon waveguides: An approximate analytic approach. *J. Lightwave Technol.*, 27(15):3241–3248, 2009.

[37] R. A. Fisher and W. K. Bischel. Numerical studies of the interplay between self-phase modulation and dispersion for intense plane-wave laser pulses. *J. Appl. Phys.*, 46(11), 1975.

[38] H. Ghafouri-Shiraz, P. Shum, and M. Nagata. A novel method for analysis of soliton propagation in optical fibers. *J. Quantum Electron.*, 31(1), 1995.

[39] G. P. Agrawal. *Nonlinear Fiber Optics*. Academic Press, forth edition, 2007.

[40] G. Polisski, D. Kovalev, G. Dollinger, T. Sulima, and F. Koch. Boron in mesoporous Si – where have all the carriers gone? *Physica B: Physics of Condensed Matter*, 273:951–954, 1999.

[41] Y. Tao and M. Esashi. Local formation of macroporous silicon through a mask. *J. Micromech. Microeng.*, 14:1411–1415, 2004.

[42] M. Takahashi, M. Araki, and N. Koshida. Burried optical waveguides of porous silicon. *Jpn. J. Appl. Phys.*, 37:L1017–L1019, 1998.

[43] A. M. Rossi, G. Amato, V. Camarchia, L. Boarino, and S. Borini. High-quality porous-silicon buried waveguides. *Appl. Phys. Lett.*, 78(20):3003–3005, 2001.

[44] R. J. Deri and E. Kapon. Low loss III-V semiconductor optical waveguides. *J. Quantum Electron.*, 27(3):626–640, 1991.

[45] T. E. Murphy, J. T. Hastings, and H. I. Smith. Fabrication and characterization of narrow-band bragg-reflection filters in silicon-on-insulator ridge waveguides. *J. Lightwave Technol.*, 19(12):1938–1942, 2001.

[46] C. K. Sheng, W. M. M. Yunus, W. M. Z. W. Yunus, Z. A. Talib, and A. Kassim. Characterization of thermal, optical and carrier transport properties of porous silicon using the photoacoustic technique. *Physica B*, 403:2634–2638, 2008.

[47] O. Boyraz, P. Koonath, V. Raghunathan, and B. Jalali. All optical switching and continuum generation in silicon waveguides. *Opt. Express*, 12:4094–4102, 2004.

[48] P. Apiratikul, A. M. Rossi, and T. E. Murphy. Nonlinearities in porous silicon optical waveguides at 1550 nm. *Opt. Express*, 17(5):3396–3406, 2009.

[49] H. K. Tsang and Y. Liu. Nonlinear optical properties of silicon waveguides. *Semicond. Sci. Technol.*, 23:064007, 2008.

[50] H. K. Tsang, C. S. Wong, T. K. Liang, I. E. Day, S. W. Roberts, A. Harpin, J. Drake, and M. Asghari. Optical dispersion, two-photon absorption and self-phase modulation in silicon waveguides at 1.5 μm wavelength. *Appl. Phys. Lett.*, 80(3):416–418, 2002.

[51] H. Fukuda, K. Yamada, T. Shoji, M. Takahashi, T. Tsuchizawa, T. Watanabe, J.-I. Takahashi, and S.-I. Itabashi. Four-wave mixing in silicon wire waveguides. *Opt. Express*, 13(12):4629–4637, 2005.

[52] R. Espinola, J. Dadap, R. Osgood Jr., S. McNab, and Y. Vlasov. C-band wavelength conversion in silicon photonic wire waveguides. *Opt. Express*, 13(11):4341–4349, 2005.

[53] H. Yamada, M. Shirane, T. Chu, H. Yokoyama, S. Ishida, and Y. Arakawa. Nonlinear-optic silicon-nanowire waveguides. *Jpn. J. Appl. Phys.*, 44:6541–6545, 2005.

[54] E. Dulkeith, Y. A. Vlasov, X. Chen, N. C. Panoiu, and R. M. Osgood Jr. Self-phase-modulation in submicron silicon-on-insulator photonic wires. *Opt. Express*, 14(11):5524–5534, 2006.

[55] A. D. Bristow, N. Rotenberg, and H. M. van Driel. Two-photon absorption and Kerr coefficients of silicon for 850-2200 nm. *Appl. Phys. Lett.*, 90:191104, 2007.

[56] Q. Lin, J. Zhang, G. Piredda, R. W. Boyd, P. M. Fauchet, and G. P. Agrawal. Dispersion of silicon nonlinearities in the near infrared region. *Appl. Phys. Lett.*, 91:021111, 2007.

[57] V. R. Almeida, Q. Xu, C. A. Barrios, and M. Lipson. Guiding and confining light in void nanostructure. *Optics Lett.*, 29:1209–1211, 2004.

[58] A. Boskovic, S. V. Chernikov, and J. R. Taylor. Direct continuous-wave measurement of n_2 in various types of telecommunication fiber at 1.55 μm. *Optics Lett.*, 21(24):1966–1968, 1996.

[59] J. H. Lee, T. Tanemura, K. Kikuchi, T. Nagashima, T. Hasegawa, S. Ohara, and N. Sugimoto. Use of 1-m Bi_2O_3 nonlinear fiber for 160-Gbit/s optical time-division demultiplexing based on polarization rotation and a wavelength shift induced by cross-phase modulation. *Optics Lett.*, 30(11):1267–1269, 2005.

[60] N. Sugimoto, T. Nagashima, T. Hasegawa, S. Ohara, K. Taira, and K. Kikuchi. Bismuth-based optical fiber with nonlinear coefficient of 1360 $W^{-1}km^{-1}$. *Proc. Opt. Fiber Commun. Conf.*, (PDP26) 2004.

[61] E. C. Mägi, L. B. Fu, H. C. Nguyen, M. R. E. Lamont, D. I. Yeom, and B. J. Eggleton. Enhanced Kerr nonlinearity in sub-wavelength diameter As_2Se_3 chalcogenide fiber tapers. *Opt. Express*, 15(16):10324–10329, 2007.

[62] Q. Xu, V. R. Almeida, and M. Lipson. Time-resolved study of Raman gain in highly confined silicon-on-insulator waveguides. *Opt. Express*, 12(19):4437–4442, 2004.

[63] X. G. Chen, N. C. Panoiu, and R. M. Osgood. Theory of Raman-mediated pulsed amplification in siliconwire waveguides. *J. Quantum Electron.*, 42:160–170, 2006.

[64] C. Koos, L. Jacome, C. Poulton, J. Leuthold, and W. Freude. Nonlinear silicon-on-insulator waveguides for all-optical signal processing. *Opt. Express*, 15(10):5976–5990, 2007.

[65] M. A. Foster, A. C. Turner, M. Lipson, and A. L. Gaeta. Nonlinear optics in photonic nanowires. *Opt. Express*, 16(2):1300–1320, 2008.

[66] J. U. Kang, G. I. Stegeman, and J. S. Aitchison. All-optical multiplexing of femtosecond signals using an AlGaAs nonlinear directional coupler. *Electron. Lett.*, 31(2):118–119, 1995.

[67] J. E. Heebner, N. N. Lepeshkin, A. Schweinsberg, G. W. Wicks, R. W. Boyd, R. Grover, and P.-T. Ho. Enhanced linear and nonlinear optical phase response of AlGaAs microring resonators. *Optics Lett.*, 24(7):769–771, 2004.

[68] D. Lauvernier, S. Garidel, M. Zegaoui, J. P. Vilcot, and D. Decoster. GaAs/polymer optical nanowires: fabrication and characterisation. *Electron. Lett.*, 42(4):217–219, 2006.

[69] R. Katouf, N. Yamamoto, A. Kanno, N. Sekine, K. Akahane, H. Sotobayashi, T. Isu, and M. Tsuchiya. Ultrahigh relative refractive index contrast GaAs nanowire waveguides. *Appl. Phys. Express*, 1:122101, 2008.

[70] J. Meier, W. S. Mohammed, A. Jugessur, L. Qian, M. Mojahedi, and J. S. Aitchison. Group velocity inversion in AlGaAs nanowires. *Opt. Express*, 15(20):12755–12762, 2007.

[71] D. Lauvernier, S. Garidel, M. Zegaoui, J. P. Vilcot, J. Harari, V. Magnin, and D. Decoster. Optical devices for ultra-compact photonic integrated circuits based on III-V/polymer nanowires. *Opt. Express*, 15(9):5333–5341, 2007.

[72] J. Lu, X. Meng, A. J. Springthorpe, F. R. Shepherd, and M. Poirier. Inductively coupled plasma etching of GaAs low loss waveguides for a travelling waveguide polarization converter, using chlorine chemistry. *J. Vac. Sci. Technol. A*, 22(3):1058–1061, 2004.

[73] R. Claps, D. Dimitropoulos, V. Raghunathan, Y. Han, and B. Jalali. Observation of stimulated Raman amplification in silicon waveguides. *Opt. Express*, 11(15):1731–1739, 2003.

[74] T. K. Liang and H. K. Tsang. Nonlinear absorption and Raman scattering in silicon-on-insulator optical waveguides. *J. Sel. Top. Quantum Electon.*, 10(5):1149–1153, 2004.

[75] D. Vignaud, J. F. Lampin, and F. Mollot. Two-photon absorption in. InP substrates in the 1.55 μm range. *Appl. Phys. Lett.*, 85(2):239–241, 2004.

[76] M. J. Weber. *CRC Handbook of Laser Science and Technology*, volume 3. CRC Press, 1982.

[77] T. Durhuus, C. Joergensen, B. Mikkelsen, R. J. S. Pedersen, and K. E. Stubkjaer. All optical wavelength conversion by SOAs in a Mach-Zehnder configuration. *IEEE Photon. Technol. Lett.*, 6(1):53–55, 1994.

[78] T. K. Liang, L. R. Nunes, T. Sakamoto, K. Sasagawa, T. Kawanishi, M. Tsuchiya, G. R. A. Priem, D. Van Thourhout, P. Dumon, R. Baets, and H. K. Tsang. Ultrafast all-optical switching by cross-absorption modulation in silicon wire waveguides. *Opt. Express*, 13(19):7298–7303, 2005.

[79] D. J. Moss, L. Fu, I. Littler, and B. J. Eggleton. Ultrafast all-optical modulation via two-photon absorption in siliconon-insulator waveguides. *Electron. Lett.*, 41(6):320–321, 2005.

[80] X. Yang, A. K. Mishra, R. J. Manning, R. P. Webb, and A. D. Ellis. All-optical 42.6 Gbit/s NRZ to RZ format conversion by cross-phase modulation in single SOA. *Electron. Lett.*, 43(16):890–892, 2007.

[81] W. Astar, J. B. Driscoll, X. Liu, J. I. Dadap, W. M. J. Green, Y. A. Vlasov, G. M. Carter, and R. M. Osgood Jr. Conversion of 10 Gb/s NRZ-OOK to RZ-OOK utilizing XPM in a Si nanowire. *Opt. Express*, 17(15):12987–12999, 2009.

[82] T. Tanemura, J. Lee, D. Wang, K. Katoh, and K. Kikuchi. Polarization-insensitive 160-Gb/s wavelength converter with all-optical repolarizing function using circular-birefringence highly nonlinear fiber. *Opt. Express*, 14(4):1408–1412, 2006.

[83] J. S. Aitchison, D. C. Hutchings, J. U. Kang, G. I. Stegeman, and A. Villeneuve. The nonlinear optical properties of AlGaAs at the half band gap. *J. Quantum Electron.*, 33(3):341–348, 1997.

[84] S. T. Ho, C. E. Soccolich, M. N. Islam, W. S. Hobson, A. F. J. Levi, and R. E. Slusher. Large nonlinear phase shifts in low-loss $Al_xGa_{1-x}As$ waveguides near half-gap. *Appl. Phys. Lett.*, 59(20):2558–2560, 1991.

[85] W. Astar, P. Apiratikul, T. E. Murphy, and G. M. Carter. Wavelength conversion of 10 Gb/s RZ–OOK using filtered XPM in a passive GaAs/AlGaAs waveguide. *submitted to IEEE Photon. Technol. Lett.*, 2009.

[86] K. Inoue and T. Mukai. Signal wavelength dependence of gain saturation in a fiber optical parametric amplifier. *Optics Lett.*, 26(1):10–12, 2001.

[87] R. H. Stolen and J. E. Bjorkholm. Parametric amplification and frequency conversion in optical fibers. *J. Select. Topics in Quantum. Electron.*, 18(7):1062–1072, 1982.

[88] A. M. Darwish, E. P. Ippen, H. Q. Le, J. P. Donnelly, and S. H. Groves. Optimization of four-wave mixing conversion efficiency in the presence of nonlinear loss. *Appl. Phys. Lett.*, 69(6):737–739, 1996.

[89] P. Apiratikul, W. Astar, G. M. Carter, and T. E. Murphy. Demonstration of 10–Gb/s wavelength conversion using four–wave mixing in GaAs waveguide. *submitted to IEEE Photon. Technol. Lett.*, 2009.

[90] C. Dorrer. High-speed measurements for optical telcommunication systems. *J. Select. Topics in Quantum. Electron.*, 12(4):843–858, 2006.

[91] I. Kang and C. Dorrer. Optical sampling source-free simultaneous eye-diagram monitoring and clock recovery up to 160 Gb/s. *in Eur. Conf. Optical Communications (ECOC) 2003*, Paper 4.2.4 2003.

[92] S. Kodama, T. shimuzu, T. Yoshimatsu, K. Yoshino, T. Furata, and H. Ito. Ultrafast optical sampling gate monlithically integrating a PD and EAM. *Electron. Lett.*, 40(11):696–697, 2004.

[93] N. Yamada, S. Nogiwa, and H. Ohta. 640-Gb/s OTDM signal measurement with high-resolution optical sampling system using wavelength-tunable soliton pulses. *IEEE Photon. Technol. Lett.*, 16(4):1125–1127, 2004.

[94] J. Li, J. Hansryd, P. O. Hedekvist, P. A. Andrekson, and S. N. Knudsen. 300-Gb/s eye-diagram measurement by optical sampling using fiber-based parametric amplification. *IEEE Photon. Technol. Lett.*, 13(9):987–989, 2001.

[95] J. Li, M. Westlund, H. Sunnerud, B.-E. Olsson, M. Karlsson, and P. A. Andrekson. 0.5 Tb/s eye-diagram measurement by optical sampling using XPM-induced wavelength shifting in highly nonlinear fiber. *IEEE Photon. Technol. Lett.*, 16(2):566–568, 2004.

[96] C. Schmidt, C. Schubert, S. Watanabe, F. Futami, R. Ludwig, and H. G. Weber. 320 Gb/s all-optical eye diagram sampling using gain-transparent ultrafast-nonlinear interferometer (GT-UNI). *in Eur. Conf. Optical Communications (ECOC) 2002*, Paper 2.1.3.

[97] M. Westlund, P. A. Andrekson, H. Sunnerud, J. Hansryd, and J. Li. High-performance optical-fiber-nonlinearity-based optical waveform monitoring. *J. Lightwave Technol.*, 23(6):2012–2022, 2005.

[98] C. Dorrer, D. C. Kilper, H. R. Stuart, G. Raybon, and M. G. Raymer. Linear optical sampling. *IEEE Photon. Technol. Lett.*, 15(12):1746–1748, 2003.

[99] R. Salem, A. A. Ahmadi, G. E. Tudury, G. M. Carter, and T. E. Murphy. Two-photon absorption for optical clock recovery in OTDM networks. *J. Lightwave Technol.*, 24(9), 2006.

[100] P. J. Maguire, L. P. Barry, T. Krug, W. H. Guo, J. O. Dowd, M. Lynch, A. L. Bradley, J. F. Donegan, and H. Folliot. Optical signal processing via two-photon absorption in a semiconductor microcavity for the next generation of high-speed optical communications network. *J. Lightwave Technol.*, 24(7), 2006.

[101] Z. Zheng, A. M. Weiner, J. H. Marsh, and M. M. Karkhanehchi. Ultrafast optical thresholding based on two-photon-absorption GaAs waveguide photodetectors. *IEEE Photon. Technol. Lett.*, 9(4):493–495, 1997.

[102] T. K. Liang, L. R. Nunes, M. Tsuchiya, K. S. Abedin, T. Miyazaki, D. Van Thourhout, W. Bogaerts, P. Dumon, R. Baets, and H. K. Tsang. High speed logic gate using two-photon absorption in silicon waveguides. *Optics Comm.*, 265(1), 2006.

[103] J.-C. Diels and W. Rudolph. *Ultrashort Laser Pulse Phenomena: Fundamentals, Techniques, and Applications on a Femtosecond Time Scale*. Academic Press, second edition, 2006.

[104] K. Kikuchi. Optical sampling system at 1.5μm using two photon absorption in Si avalanche photodiode. *Electron. Lett.*, 34(13):1354–1355, 1998.

[105] P. J. Maguire, L. P. Barry, T. Krug, M. Lynch, A. L. Bradley, J. F. Donegan, and H. Folliot. All-optical sampling utilising two-photon absorption in semiconductor microcavity. *Electron. Lett.*, 41(8):489–490, 2005.

[106] M. Dinu, D. C. Kilper, and H. R. Stuart. Optical performance monitoring using data stream intensity autocorrelation. *J. Lightwave Technol.*, 24(3):1194–1202, 2006.

[107] F. Boitier, J.-B. Dherbecourt, A. Godard, and E. Rosencher. Infrared quantum counting by nondegenerate two photon conductivity in GaAs. *Appl. Phys. Lett.*, 94(8):081112, 2009.

[108] N. Nishizawa, R. Okamura, and T. Goto. Analysis of widely wavelength tunable femtosecond soliton pulse generation using optical fibers. *Jpn. J. Appl. Phys.*, 38(8):4768–4771, 1999.

[109] D. C. Hutchings and E. W. Van Stryland. Nondegenerate two-photon absorption in zinc blende semiconductors. *J. Opt. Soc. Am. B*, 9(11):2065–2074, 1992.

[110] P. Apiratikul and T. E. Murphy. Background-suppressed ultrafast optical sampling using nondegenerate two–photon absorption in a GaAs photodiode. *to appear in IEEE Photon. Technol. Lett.*, 2009.

[111] R. Dekker, A. Driessen, T. Wahlbrink, C. Moormann, J. Niehusmann, and M. Forst. Ultrafast Kerr-induced all-optical wavelength conversion in silicon waveguides using 1.55 μm femtosecond pulses. *Opt. Express*, 14(18):8336–8346, 2006.

[112] A. B. Fallahkhair, K. S. Li, and T. E. Murphy. Vector finite difference modesolver for anisotropic dielectric waveguides. *J. Lightwave Technol.*, 26(11):1423–1431, 2006.

[113] S. Adachi. GaAs, AlAs, and $Al_xGa_{1-x}As$ material parameters for use in research and device applications. *J. Appl. Phys.*, 58(3):1–29, 1985.

[114] J. Shin, S. Wu, and N. Dagli. Bulk undoped GaAs-AlGaAs substrate-removed electrooptic modulators with 3.7-V-cm drive voltage at 1.55 μm. *IEEE Photon. Technol. Lett.*, 18(21):2251–2253, 2006.

[115] J. Cardenas, C. B. Poitras, J. T. Robinson, K. Preston, L. Chen, and M. Lipson. Low loss etchless silicon photonic waveguides. *Opt. Express*, 17(6):4752–4757, 2009.

[116] G. M. Yang, D. H. Lim, J.-H. Kim, K. Y. Lim, and H. J. Lee. Selective oxidation of AlGaAs/GaAs structure and its application to vertical cavity lasers. *Jpn. J. Appl. Phys.*, 37:1391–1393, 1998.

[117] R. Salem, G. E. Tudury, T. U. Horton, G. M. Carter, and T. E. Murphy. Polarization-insensitive optical clock recovery at 80 Gb/s using a silicon photodiode. *IEEE Photon. Technol. Lett.*, 17(9):1968–1970, 2005.